12-2017

# Unsteady Aerodynamics and Blade-Row Interactions in the Embedded Stage of an Axial Compressor

Douglas Ryan Matthews
*Purdue University*

# UNSTEADY AERODYNAMICS AND BLADE-ROW INTERACTIONS IN THE EMBEDDED STAGE OF AN AXIAL COMPRESSOR

by

**Douglas Ryan Matthews**

**A Thesis**

*Submitted to the Faculty of Purdue University*

*In Partial Fulfillment of the Requirements for the degree of*

**Master of Science in Aeronautics and Astronautics**

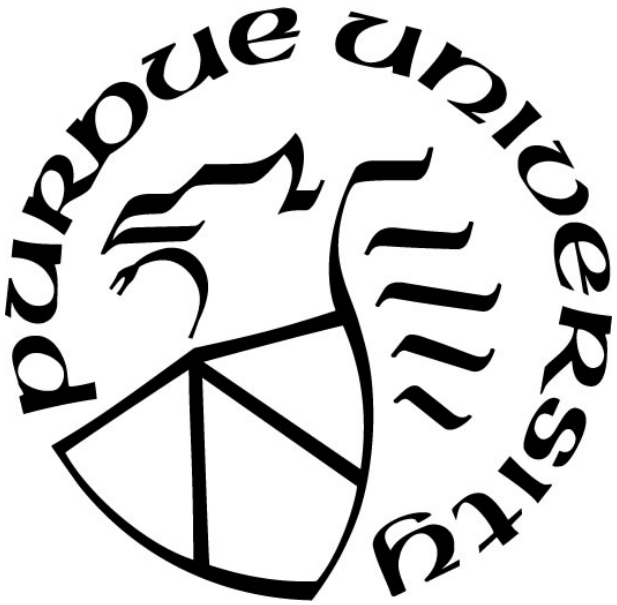


Department of Aeronautics and Astronautics

West Lafayette, Indiana

December 2017

# THE PURDUE UNIVERSITY GRADUATE SCHOOL
# STATEMENT OF THESIS APPROVAL

Dr. Nicole Key, Chair

Department of Mechanical Engineering

Dr. Carson Slabaugh

Department of Aeronautics and Astronautics

Dr. Guillermo Paniagua

Department of Mechanical Engineering

**Approved by:**

Dr. Wayne Chen

Head of the Departmental Graduate Program

*For my family.*

# ACKNOWLEDGMENTS

I would like to begin my thanks with my advisor, Professor Nicole Key, for whom I am grateful for her guidance and the opportunities granted to surround myself with the many exceptional individuals at the Maurice J. Zucrow Laboratories and Purdue University, both within and outside of our research group. I greatly appreciate my committee members, Dr. Carson Slabaugh and Dr. Guillermo Paniagua, for serving on my examination committee and for their valuable feedback of this work. Technical guidance from John Fabian as well as the technical expertise from Grant Malicoat and Rob McGuire have been essential for this research. Grant Malicoat requires special recognition for his role in keeping our projects running and taking the time to impart his experience with us as we work toward a common goal. Financial support from Rolls-Royce and the GUIde 5 consortium are also gratefully acknowledged.

I am deeply appreciative of the current and former postdoctoral researchers and research scientists with whom I have had the great pleasure of working with: Drs. Reid Berdanier, Natalie Smith, Fangyuan Lou, and Leng Yujun. Their patience, expertise, and friendship have been invaluable. A similar appreciation is in order for the rest of our tight-knit research group, whose lasting friendships I will always cherish. Special recognition is required for members of the Purdue 3-Stage team, including Nicholas Kormanik, Nyansafo Aye-Addo, and Razvan Rusu, for the countless hours spent solving challenging problems together and mutual support for the many simultaneous research projects. My teammate, Nicholas Kormanik, whose friendship, support, and parallel efforts have been beyond measure.

Lastly, and certainly not least, thank you to my family: my parents Alan and Martha, and my sister, Emily. Without your unwavering support, especially during times I have given you every reason to doubt extending it, my accomplishments will have never been achievable. I love you all very much.

# TABLE OF CONTENTS

# LIST OF TABLES

# LIST OF FIGURES

# LIST OF SYMBOLS

| Symbol | Description |
|---|---|
| $1CWB$ | First Chordwise Bending |
| $1T$ | First Torsion |
| $c$ | Chord |
| $C_P$ | Surface Pressure Coefficient |
| $f$ | Frequency |
| $F$ | Force |
| $k$ | Spring Stiffness Constant |
| $m$ | Mass |
| $\dot{m}$ | Mass Flow Rate |
| $N$ | Rotational Speed |
| $P$ | Pressure |
| $r$ | Radial Coordinate |
| $t$ | Time |
| $U_t$ | Blade Tip Speed |
| $V$ | Absolute Velocity |
| $W$ | Relative Velocity |
| $x$ | Axial Coordinate |

*Greek*

| | |
|---|---|
| $\eta$ | Isentropic Efficiency |
| $\omega$ | Angular Frequency |
| $\Omega$ | Blade Angular Velocity |
| $\rho$ | Density |
| $\theta$ | Tangential Coordinate |
| $\zeta$ | Damping Coefficient |

*Subscripts*

| | |
|---|---|
| AA | Radial and Circumferential Area Average |
| $c$ | Corrected Condition |
| mech | Mechanical |
| $o$ | Stagnation Condition |
| $s$ | Static Condition |
| $x$ | Axial Direction |
| $\theta$ | Tangential Direction |
| $in$ | Inlet Measurement Position |
| $ex$ | Exit Measurement Position |

*Accents*

| | |
|---|---|
| $\langle \quad \rangle$ | Ensemble Average |
| $\lvert \quad \rvert$ | Normalized |

# LIST OF ABBREVIATIONS

| Abbreviation | Description |
|---|---|
| BPP | Blade-Passing Period |
| BPF | Blade-Pass Frequency |
| DCA | Double Circular Arc |
| EA | Ensemble Average |
| EO | Engine Order |
| HL | High Loading |
| IBR | Integrally Bladed Rotor |
| IGV | Inlet Guide Vane |
| NB | Number of Blades |
| ND | Nodal Diameter |
| OPR | Overall Pressure Ratio |
| PE | Peak Efficiency |
| R1/R2/R3 | Rotor 1/Rotor 2/ Rotor 3 |
| RMS | Root-Mean-Square |
| S1/S2/S3 | Stator 1/Stator 2/ Stator 3 |
| TPR | Total Pressure Ratio |
| VP | Vane Passage |

# ABSTRACT

Author: Matthews, Douglas, R. MSAAE
Institution: Purdue University
Degree Received: December 2017
Title: Unsteady Aerodynamics and Blade-Row Interactions in the Embedded Stage of an Axial Compressor
Major Professor: Dr. Nicole L. Key

In a mature engineering field like compressor aerodynamics, the most accessible advances in machine technology, translating to performance and efficiency, have been discovered and have found industry design applications. As the community continues to make progress, increasingly challenging aspects of the involved physics must be exploited. Modern turbomachinery operates with larger bypass ratios, smaller cores, and lighter, thinner, and more flexible materials resulting in the maintenance of higher operating pressures and temperatures. As the performance and efficiency of these machines continues to climb, the same technological advances reinforce challenges like forced-response vibration, high-cycle fatigue of engine components, and large relative tip clearances in an engine core.

Accounting for these challenges increasingly depends on the investigation of the unsteady domain for solutions. Tools at the disposal of the designer include progressively improving computational simulations through both computational resources and attainable model fidelity. As essential as these tools are for modern turbomachinery design, the confidence in their results is only as good as the experimental data used to validate them. The objective of this research is the experimental investigation and characterization of the transient aerodynamics and blade-row interactions near forced-response resonant vibratory operating conditions in a multi-stage environment.

Experimental methods are focused on fast-response pressure transducers with the high frequency response capable of capturing the unsteady pressure fluctuations associated with the high-speed rotation and blade-pass frequency of a modern high-pressure core axial compressor. Investigation is centered on an engine-representative embedded rear stage, with adjacent stages establishing realistic flow conditions and resulting boundary

conditions for model comparison. Aerodynamic characterization of several flow conditions and the examination of the effect of a reduced vane-count stator configuration upstream of the embedded stage are performed with measurements of the embedded rotor at the casing endwall and rotor exit plane, as well as within a passage of the embedded stator. Circumferential vane traverse around stationary instrumentation provide a full vane passage of phase-locked, time-resolved pressure measurements of the rotor aerodynamics and the unsteady loading of the embedded stator is distinguished for a single vane position.

Results from this investigation identify and describe the inception and trajectory of tip clearance flows, including the tip leakage vortex and double-leakage tip clearance flow. Evidence of an upstream vane wake interaction with the rotor occurs for limited regions of vane passage positions. Spectral analyses and pressure unsteadiness provide further insight into the blade-row interactions.

# 1. INTRODUCTION

## 1.1 Motivation

High-speed turbomachinery assumes many forms and scales, from tiny handheld surgical drills, to jet engines, turbochargers, rocket turbopumps in vehicles, and even industrial power plants with entire buildings constructed to accommodate and support them. All of these machines and the industries built around them face the same challenges in their design and maintenance. Efficiency is one of the driving factors of modern turbomachinery design. In the aerospace industry, an important result of increased efficiency is lower fuel consumption. Two aspects of efficiency must be considered when designing an airbreathing engine: propulsive efficiency, how efficiently the power produced by the engine is utilized to propel the vehicle, and thermal efficiency, how efficiently energy added by heat is converted to net work output. Applying a simplified energy balance to the power supplied by an engine to the working fluid results in the following formulation of propulsive efficiency,

$$\eta_p = \frac{\text{power delivered to vehicle}}{\text{net (mechanical) power in the exhaust}} = \frac{\dot{m}_{\text{air}}(V_{\text{ex}} - V_{\text{in}})V_{\text{in}}}{\frac{1}{2}\dot{m}_{\text{air}}(V_{\text{ex}}^2 - V_{\text{in}}^2)} = \frac{2V_{\text{in}}}{V_{\text{ex}} + V_{\text{in}}}, \qquad (1.1)$$

describing the mass flow rate and flow velocities entering and exiting the machine, where $\dot{m}_{air}$ is the mass flow rate of air entering the machine, $V_{\text{in}}$ is the flow velocity at the inlet, and $V_{\text{ex}}$ is the flow velocity of the exhaust. A simple force balance of the same system,

$$F \approx \dot{m}_{\text{air}} \times (V_{\text{ex}} - V_{\text{in}}), \qquad (1.2)$$

describes the jet thrust force produced with the same variables used in the formulation of propulsive efficiency. Comparing these expressions, propulsive efficiency is maximized when the flow is leaving the engine at the same speed it enters ($V_{\text{ex}} = V_{\text{in}}$). However, this same condition would result in no jet thrust produced. Instead, to maximize propulsive efficiency, turbofan engine manufacturers decrease the difference in velocities across the engine and increase the mass flow rate to maintain the same force. An analogy for these different approaches is the application of a large impulse to a small amount of air—a turbojet engine—or a smaller impulse to a large amount of air, the turbofan engine.

To further increase the mass flow rate through the engine, bypass ratios, the ratio of the mass flow rate through the bypass stream to the mass flow rate entering the core, have increased to produce more thrust with increased efficiency. Early turbofan engines had bypass ratios of less than one and overall pressure ratios (OPR) of about 10:1. Modern high-speed aircraft, e.g. fighter jets, maintain low bypass ratios but operate with OPR of about 30:1. Modern high-bypass commercial turbofans, e.g. General Electric GEnx, Rolls-Royce Trent series, and Rolls-Royce Advance3, have bypass ratios of up to 12:1 and OPR of up to 60:1. Future high-bypass turbofans, like the Rolls-Royce UltraFan are projected to operate with 15:1 bypass ratio and 70:1 overall pressure ratio. Larger bypass ratios can be achieved in two ways: increasing the size (diameter) of an engine and the corresponding ducted flow of the fan stream, or decreasing the size of the core and corresponding core stream of the engine. Conventional limits on nacelle size have been reached; for a modern commercial turbofan, the bottom of the nacelle is an irregular shape—flattened to maintain necessary ground clearance with the larger fan diameter. Decreasing core size bears its own difficulties; as rotor blades decrease in size, the constant physical clearance gap between the tip and endwall is much larger relative to the size of the blade. Decreased core size also results in smaller axial gaps between blade rows, potentially facilitating negative interaction between blade rows.

Industry standards have driven modern turbomachinery designs to incorporate faster assembly, lighter materials, smaller cores, and maintain higher operating pressures and temperatures. Traditional manufacturing methods of rotors involve machining a slot (typically a dovetail, fir tree, or bulb style) in the rotor disk by broaching, milling, or grinding processes. Matching blade roots are machined into individual blades and are then fastened into the rotor drum. Newer manufacturing methods, including multi-axis CNC machining, investment casting, additive manufacturing, and wire electrical discharge machining (EDM), allow modern turbomachinery blade-rows to be manufactured as single-piece parts. These parts are known as bladed disks (blisks) or integrally bladed rotors (IBR). These manufacturing techniques have greatly decreased the number of components and assembly time of modern turbomachines, eliminated the source of crack initiation and propagation in the rotor disk associated with the machined root slot assembly, all while

simultaneously taking advantage of increasingly complex blade geometries associated with increasing capabilities of computer-aided design and manufacture. The result of these technological advances is increased machine efficiencies, measured through increased operating pressures and temperatures. The tradeoff with this valuable industry growth manifests as an environment rife with opportunity for blade vibration with lighter, thinner bladed disks and the elimination of the mechanical damping provided by the mechanical attachment of the blade root into the rotor disk slot.

## 1.2 Forced Response Vibration and Aeromechanics

Aeromechanics describes the interaction between fluid flow and structures in the flow path. Several subgroups of aeromechanics exist, including forced response vibration. If not accounted for in design and operation, the periodic motion of turbomachinery can produce a favorable environment for resonant vibration. For this to be avoided, methods and tools for designing and protecting these machines are required. Vibration can be described mathematically from a derivation of the governing equations of motion to give the general form of the second-order ordinary differential equation describing a single degree-of-freedom mass-spring-damper system:

$$m\ddot{x} + \zeta\dot{x} + kx = F\mathrm{e}^{i\omega t} \tag{1.3}$$

where $m$ is the mass of the system, $x$ is the position of the mass, $\zeta$ is the damping coefficient, and $k$ is the proportionality constant associated with the stiffness of the spring. The right-hand side of this equation is the externally applied forcing function, in this form periodic in time. Without this term, the system would experience free vibration. Forced response focuses on the system response when this forcing function is present and can occur with random excitation (non-synchronous vibration) or periodically (synchronous vibration). Synchronous vibration, the focus of this study, occurs at the fundamental frequency and its integer multiples, or harmonics, and is, therefore, coupled with the machine's shaft speed. This is also known as blade-passing excitation and must meet two conditions: the excitation frequency must be equal to a bladed disk assembly natural frequency and the excitation pattern must match the associated nodal diameter mode shape.

Forcing functions develop from distortions in the flow field caused by surrounding blade-rows, struts, and inlet distortion. The most prominent forcing functions acting on a rotor occur as transported wakes from upstream stationary vane-rows and non-uniform potential fields generated by the upstream and downstream stationary vane-rows.

Forced response vibration is the result of unsteady aerodynamic loading experienced by the blade due to these forcing functions with a frequency equal to the natural frequency of vibration for a blade. If operated at this resonant vibrating condition, the machine can experience high-cycle fatigue, thereby compromising machine longevity and ultimately resulting in fatigue failure of the blades. The ability to detect and predict these dangerous resonant conditions is essential to the durability of turbomachinery. An important tool used in the design and operation of these machines is the Campbell diagram. The diagram represents the system response spectrum as a function of its oscillation regime, the operating speed of the machine. Predictions of modal frequencies from finite-element models are compared with synchronous response lines, also known as engine order lines, and the interception of a modal frequency with an engine order line indicate speed regimes where synchronous vibration may occur. Engine order (EO) is described by the relation:

$$EO = \frac{f}{N_{\mathrm{mech}}/60} \tag{1.4}$$

where $f$ is the frequency of the excited mode, and $N_{\mathrm{mech}}/60$ is the shaft rotational speed, both having units of Hz. A simple example of a Campbell diagram, Figure 1.1, shows resonant crossings associated with two different modes and engine order lines.

Bladed disk vibration encompasses vibration of the blades and vibration of the disk. To describe a bladed disk vibration mode, the natural frequency and nodal diameter are required. Blade alone frequencies are independent of the number of nodal diameters whereas disk alone frequencies are dependent on the number of nodal diameters. When blades are attached to a disk, a system is formed and the individual disk and blade

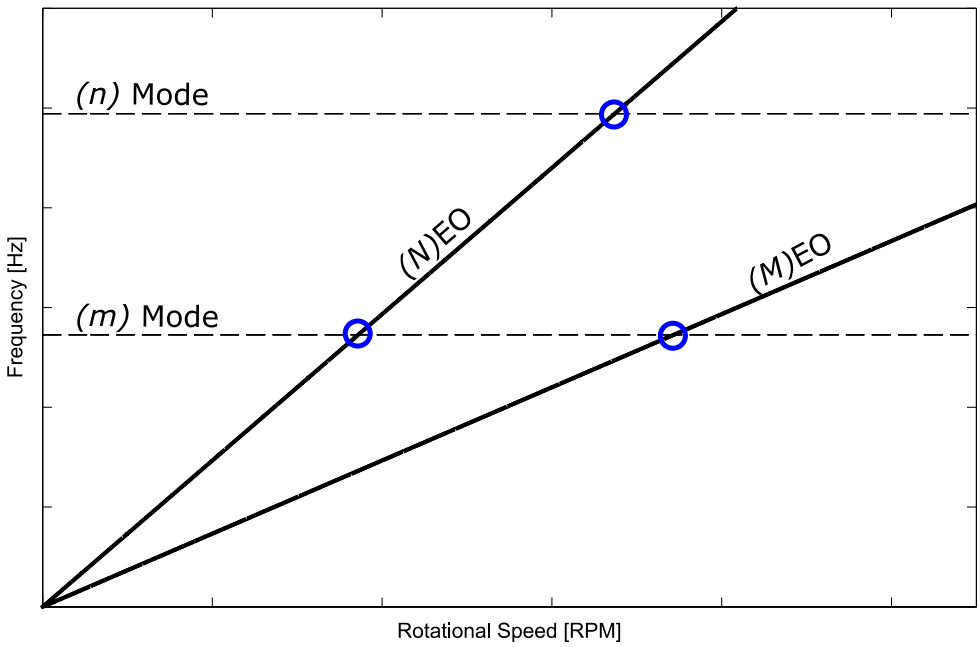


Figure 1.1: Example Campbell diagram showing resonant crossings with different engine order crossing lines.

frequencies and their mode shape characteristics become coupled components of the overall system. This combination of blade and disk modes of the coupled system produced two natural frequencies when a bladed disk vibrates. One of these natural frequencies is lower than the lowest individual blade or disk natural frequency and the other is higher than the highest individual component natural frequency. When the blades and disk become a coupled system, the blade alone mode becomes a family of modes, with each mode family having a different number of nodal diameters. As explained by Baumgartner et al. (1995), every classical vibration mode shape, e.g., 1st flap (1F), 1st torsion (1T), is an upper term comprising complete families of individual modes, described by the spatial frequency of a wave, the wavenumber. Engine orders and nodal diameters are closely related. For $N$ distortions in the flow field, the rotating blade will experience a number of disturbances equal to $N$ times the speed of rotation, the definition of the engine order. A periodic mode shape can only be excited by periodic excitation of the same wavenumber. An illustration of the relationship of blade alone and disk alone modes with the coupled bladed disk system modes is shown in Figure 1.2.

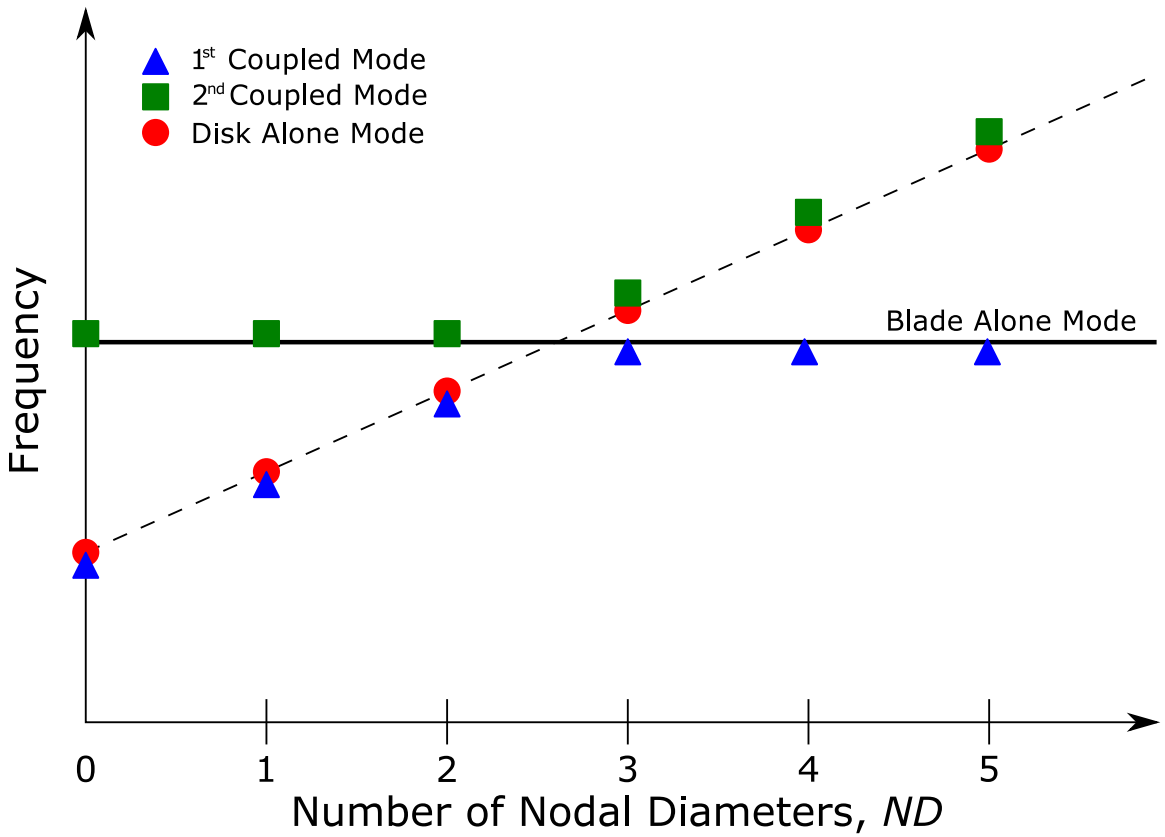


Figure 1.2: Relationship of blade alone and disk alone modes with bladed disk modes.

This means the *N*EO excitation will only excite modes with a corresponding wavenumber. When the *N* waves are imposed on a circular membrane, their lines make up the lines of zero deflection across the diameter of the disk, or nodal diameters. Similarly, nodal circles describe constant radii around the disk of zero deflection. Figure 1.3 depicts a vibrating circular membrane with these features. For high nodal diameters and rigid disks, blade modes dominate the vibration response. At low nodal diameters, disk vibrations are dominant, and flexible disks exhibit coexisting disk and blade vibratory characteristics.

Campbell diagrams are an important tool used in the design of turbomachinery, but they can only indicate the speeds where a forced response vibration crossing occurs and are unable to predict the amplitude of response. The amplitude will depend on the damping, both mechanical and aerodynamic. Damping is difficult to predict, and therefore, it is

important to acquire comprehensive datasets to develop and validate prediction tools.

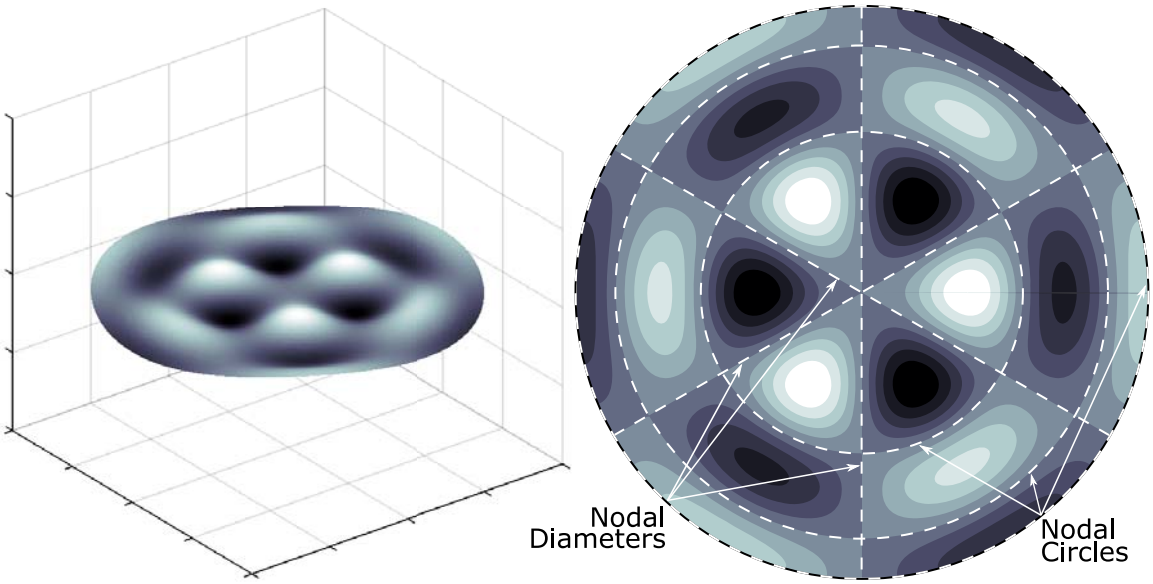


Figure 1.3: Vibrating circular membrane with a (3,3) mode - 3 nodal diameters and 3 nodal circles.

## 1.3 Forced Response Forcing Functions

A spatial non-uniformity in the rotating reference frame of a rotor is a periodic temporal non-uniformity in the stationary reference frame of a stator and vice-versa. These non-uniformities create the temporal aerodynamic forcing functions, or gusts, and associated pressure fluctuations and dynamic loading on neighboring blade-rows. The aerodynamic forcing function can be further separated into two components: vortical and potential. The vortical forcing function is associated with wakes shed from upstream boundary layers, and the potential forcing function arises from the pressure potential field, an inviscid effect caused by an airfoil's thickness and camber. Potential fields travel upstream and downstream of the locations of generation.

While the potential field effects decay very quickly with an increase in distance, wakes persist several blade-rows downstream of their source. Fundamental research of flow over circular cylinders in an open jet tunnel, studying the effects of the wake on the self-excited

and forced vibration, showed the vortex formation extended 2.2–2.3 diameters axially downstream of the cylinder (Griffin, 1972). A study performed by Gallus et al. (1982) revealed wake-flow interactions dominate for large axial distances of blade-rows and potential field interactions are is on the same order of magnitude for very small axial distances between blade-rows. Koch & Wolff (1998) examined the effects of axial blade-row spacing on forcing function strength, showing both vortical and potential forcing function magnitude decreases with axial distance. Figure 1.4 illustrates the forcing functions present for an embedded stage rotor from nearby stationary rows, the blue potential forcing functions exist from the static pressure potential fields and the red vortical forcing functions are caused by the wakes being shed from the airfoil boundary layers.

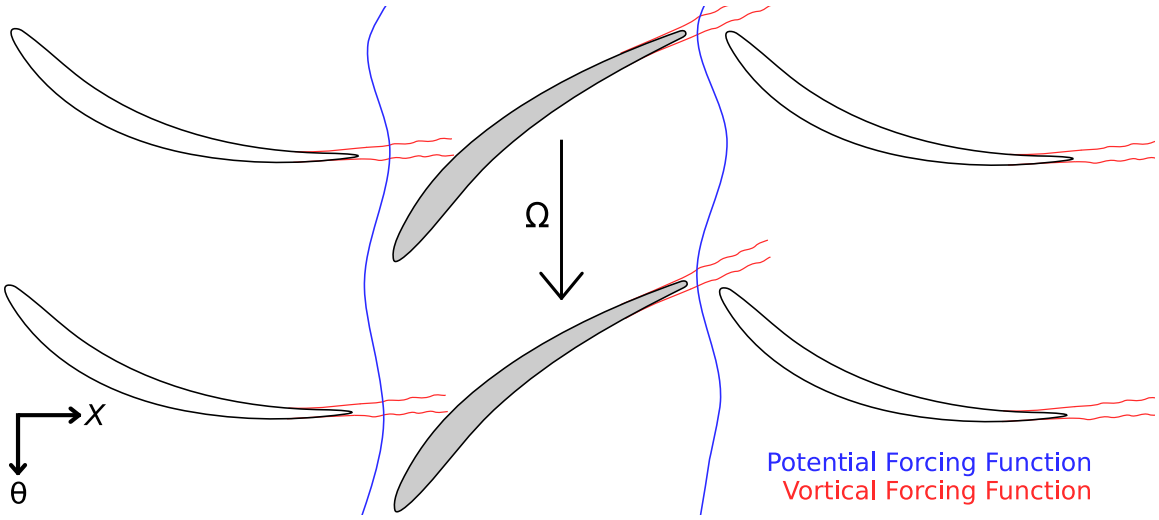


Figure 1.4: Illustration of the forcing functions present in turbomachinery systems.

Significant research has been performed on the identification of the components of the aerodynamic forcing functions and models to describe them. Models for predicting blade response to unsteady aerodynamics were initially limited to linearized two-dimensional inviscid flow analyses with small perturbations imposed on the mean flow (Whitehead, 1987; Hall & Verdon, 1989). The fundamental vortical gust modeling assumption was introduced and investigated by Henderson and Fleeter (1992a & 1992b) through comparison of the measured unsteady aerodynamic response of downstream blades with linear theory predictions. Two constraints were proposed on linear theory gusts: the

unsteady perturbation velocity vectors must be parallel so the gust is divergence free, and gust magnitude direction be parallel to the rotor downstream mean relative flow. Manwaring and Wisler (1992) added potential field forcing functions to the vortical gust wake models utilizing a technique proposed by Giles in an unpublished correspondence to split the measured unsteady flow fields into their potential and vortical components. The method used to split these components was based on unsteady velocity measurements, later termed the V-method. This method attributed violations to the constraints established by Henderson and Fleeter to the presence of an unsteady potential perturbation. A later study by Feiereisen et al. (1994) showed the fundamental vortical gust model could still be violated by effects not modeled by the V-method, in their example momentum diffusion in the wake. From this study, a method was developed to split the components using both unsteady velocity and unsteady static pressure measurements; this method was termed the P-method. Both methods were used in a study by Weaver and Fleeter (1994) to validate the techniques and investigate the effect of steady loading on the unsteady aerodynamic gust forcing functions generated by turbine rotor blade-rows. The P-method was further refined by Feiereisen and Fleeter (1994) utilizing unsteady velocity and pressure data, resulting in the removal of weighting factor ambiguity introduced in their previous work. Johnston, Feiereisen, and Fleeter (1998) acquired and analyzed data defining the forcing functions generated by a rotor, including upstream-generated wakes, to address the limitations of wake forcing-function models used for the prediction of forced response. Applying a splitting analysis technique, the forcing functions generated downstream of a rotor were primarily vortical while the gust generated upstream of a rotor had a primarily potential component.

## 1.4 Vibration Monitoring and Measurement Techniques

Convenient and cost-effective methods for detecting vibration in rotating machinery are under continual development. Several factors and tradeoffs must be considered when choosing vibration monitoring and measurement systems, including sensor technology, measurement reference frame, and system durability. Generally, the objective for any fluid dynamics measurement is to acquire accurate, detailed information without disturbing the flow field. The capability to monitor and measure blade vibration without affecting overall

power production and efficiency is, therefore, useful in both scientific research and industrial applications.

### 1.4.1 Strain Gage Transducers

Strain gage transducers have long been a preferred method of measuring vibration in turbomachines. Having been invented around the same time as the jet engine, these measurement devices have been studied and matured alongside modern turbomachinery. Strain gages are designed to convert mechanical motion to an electronic signal. As an object being measured by a strain gage deforms, the electrical resistance within the gage changes. The change in resistance can be measured through circuit analysis of a Wheatstone bridge and is related to strain through a quantity known as a gage factor. Strain gages are mounted to the rotors, simultaneously subjected to the benefits and drawbacks of measurements in the rotating reference frame. Measurements in the relative frame are useful as they observe all events encountered by the instrumented equipment throughout operation. However, it is not typically feasible to instrument each blade with strain gages, and careful strain gage installation selection is necessary. A rule-of-thumb is to install three gages for any one measurement of interest for redundancy. Blade-to-blade variability can be caused by mistuning—the asymmetry of the frequency response of a bladed disk. Transferring the data from the relative frame to the stationary frame can also be complicated, requiring a slip ring assembly or telemetry system mounted to the rotating system. Strain gages attached to rotating components suffer from limited life expectancy, as the measurement device must also experience the same stress experienced by the blades in very harsh operating environments. When mounted to the blade, the strain gage may also alter blade structural characteristics and interfere with the flow over the blade.

### 1.4.2 Non-Intrusive Stress Measurement System

Kadambi et al. (1989) suggested the most promising technologies for obtaining blade stress information would be “momentary” processes. A momentary process measures all blade vibrations through the transit time of each blade-passing beneath stationary sensors. A Non-intrusive Stress Measurement System (NSMS), also referred to as Blade Tip-Timing

(BTT) and Arrival Time Analysis (ATA), is an example of such a process. A light source, typically a laser transmitted through fiber optics, is commonly used as a sensor for a tip-timing system. As each measured blade-passes beneath the sensors, the system compares its arrival time with a baseline time. Any deviation from this baseline arrival time indicates deflection of the blade. By measuring these deflections across a series of sensors or revolutions, characteristics of the blade vibrations can be determined. An example optical blade tip-timing system is shown in Figure 1.5. Although laser probes are typically used for NSMS, any sensor with the ability to precisely indicate a blade-passing event can be used. Blade tip-timing technology was patented as early as 1949 when George W. Hardigg filed as an engineer working with Westinghouse Electrical Corporation. His invention consisted of an electromagnetic pickup coil used to detect the passing of a magnet attached to a blade tip.

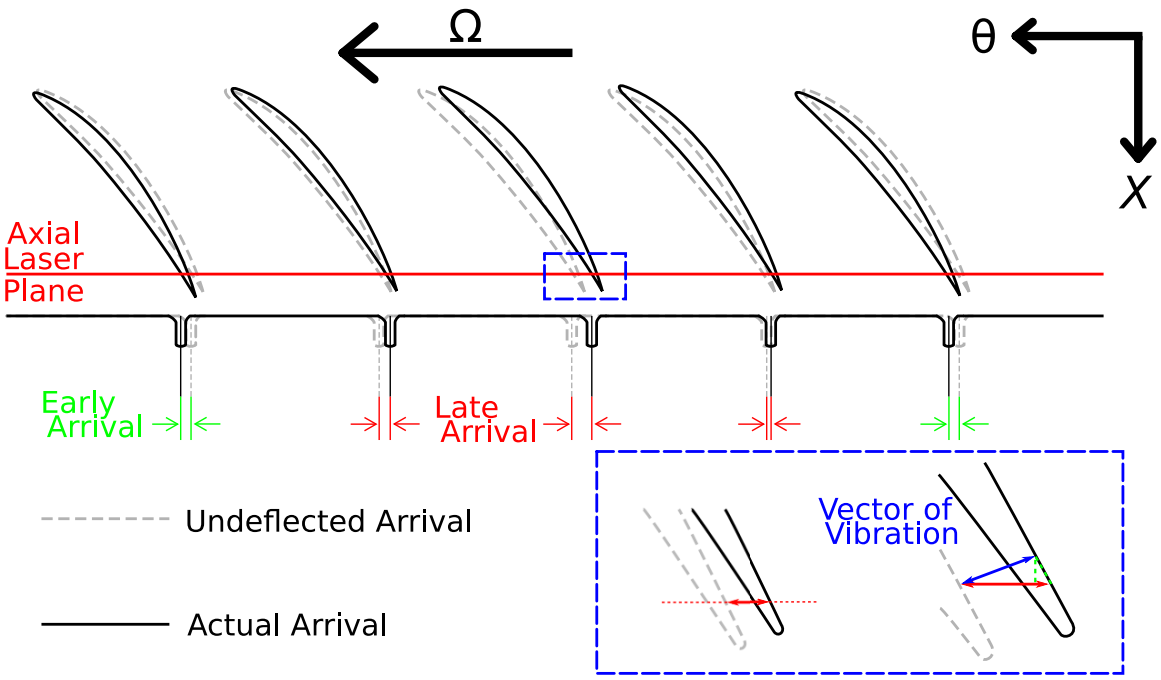


Figure 1.5: Illustration of the principles of an optical blade tip-timing system.

Optical tip timing has several benefits as a vibration monitoring system and is becoming a standard method for blade vibration analysis. Sensors are installed in the casing or shroud endwall of a turbomachine and directed radially inward. This placement of the sensors

allows for some flexibility in sensor mounting and can detect and measure all rotating blades in the row it is installed. Blade tip-timing systems with laser probes experience the same difficulties inherent with other optical measurement methods. The light probes must be oriented such that the transmission and reflection of the light can be received by the fiber optics and transmitted to the photo detector for conversion into an electrical signal. Light probes must be kept clean to receive the reflected light, and any buildup of dust and dirt can greatly degrade the perceived reflection. To accomplish this, some systems use an air delivery system to continuously clean the probes. While achieving this function, the delivered air is purged into the working fluid flowpath, thereby influencing the local flow field. Optimal probe placement is required for appropriate resolution of blade vibration characteristics. This is achieved with algorithms requiring knowledge of the predicted vibratory blade mode shape and engine order. If the light probe is not positioned over the area of deflection of the blade, the blade will appear to have arrived near its expected arrival time and resulting measurements would indicate little or no vibration occurring.

### 1.4.3 Vibration Measurement with High-Frequency Response Pressure Transducers

As blades pass through resonant conditions, a corresponding increase in vibration occurs. Excitation of the molecules of the working fluid sharing the flowpath with the vibrating blades will occur and propagate as acoustic waves. These acoustic waves, or pressure fluctuations, can be measured with a pressure transducer. Pressure transducers work using the same principle as strain gages, and in fact, pressure transducers are also known as strain gage pressure transducers. The distinction between the two transducers is their installation and cause of deformation in the sensing element. In contrast to strain gages mounted directly to a test article to experience and measure the deformation, a pressure transducer has an internal sensing element that deforms in response to an applied external pressure.

Early adopters of fast-response pressure transducers to measure vibrations (Kurkov & Dicus, 1978; Kurkov, 1981) used stationary pressure transducers mounted in the casing to measure flutter induced vibrations of rotor blades. To resolve the spectral difference in pressure on the pressure and suction sides of the blade, a procedure based on engine order sampling was used to remove the steady-state component of the pressure signal and

eliminate the engine harmonics from the overall spectra. The researchers proposed a few sampling techniques to remove the steady-state pressures from the signal. Engine order sampling, the technique used to collect data for the study, samples pressure from all blades as they pass the measurement port in the casing, effectively treating the whole rotor as a system rather than focusing on individual blades. Pressure data from a transducer located over the leading edge was captured along with a once-per-revolution (1/rev) reference signal. The steady-state portion of the pressure signal was removed by computing the average pressure over several revolutions and subtracting the average from the instantaneous pressures. Another sampling technique, blade-passage sampling, separates data into discrete revolutions and orders each revolution relative to the start of the revolution—ensemble averaging. The corresponding points in each revolution were then averaged to get a passage average of the ensemble average data and obtain a representative average of all revolutions of data taken. In addition to the spectral results, after separating the steady and unsteady components of the signal, the result was transformed to the rotating reference frame to obtain the nodal diameters of the vibrations. These experiments were compared with results from the emergent methods of optical blade-tip position measurements, and flutter was detected using high response aerodynamic data records. Therefore, precise determination of flutter frequency can be made using two stationary transducers for a blade-row of interest.

Research conducted by Mengle (1990) developed a scheme to find the dominant vibrating modes and frequencies with two stationary pressure transducers for the case of an isolated rotor and rotor-stator stage. Mengle cites several advantages of using pressure transducers when compared to other stationary sensors: avoidance of complex signal transmission from the relative frame, the ability to sense the continuous unsteady pressure field—effectively sensing all blades simultaneously rather than only once per revolution—and sensors do not need to be positioned immediately near the rotor, as the pressure field can be measured slightly further away axially from the blade-row. An important result of his research is traveling wave mode frequencies observed in the rotating reference frame are Doppler-shifted to the stationary reference frame, and furthermore, these Doppler shifts are harmonics of the rotor speed.

Baumgartner et al. (1995) used pressure transducers mounted in the casing wall just upstream of the first rotor of a 10-stage high-pressure compressor to investigate unsteady pressure fluctuations in the tip region of the rotor and its relation to blade vibration. The compressor was also instrumented with a hot-film probe at the trailing edge to measure unsteady velocity fluctuations and strain gages on the blades to measure blade response. The authors define many sources of vibration, among them forced response and rotating flow instabilities. One rotating flow instability mentioned is the generation of vortex shedding in the tip region of the rotor blades caused by enlarged tip clearance. This tip leakage vortex is the source of high fluctuations of pressure, potentially causing high-level blade vibration. This study was able to directly compare blade vibrations measured with strain gages with the fluctuating wall pressures measured by the pressure transducers. This comparison showed a direct correlation between high blade vibration amplitudes and high wall pressure fluctuations in the same speed range.

A study by Manwaring et al. (1997) marked the first time extensive detailed measurements of forced response on an airfoil were performed; specifically, inlet distortion generated forced response measurements of the first stage blade of a transonic two-stage fan. Unsteady pressure differences across the blade were measured with seven pressure transducers installed at 85 percent span on each of two adjacent rotor blades, however many of the pressure transducers failed due to the operating environment. The pressure transducers were embedded flush to one surface of the blade and pneumatically connected to the other surface with a vent hole. Vibratory stresses were measured with dynamic strain gages of the pressure transducer instrumented blades. Measurements of unsteady pressure and vibratory strain were characterized at four Campbell diagram crossings and compared against computational models.

Gill and Capece (2004) used eleven equally spaced pressure transducers around the circumference of a single stage fan casing at the same axial location upstream of the leading edge of the rotor blades to measure the flutter characteristics of the fan blade. Using a two-probe analysis, blade vibratory frequencies and nodal diameters were determined. The

authors used a cross-power spectral analysis between the two sensors with sets of data having the same time index to find the nodal diameters. A multi-probe configuration was used to analyze simultaneously the two-dimensional unsteady pressure field around the circumference of the entire rotor as a function of angular position and time. After removing the pressure component due to blade-passing, data acquired from the pressure transducers and strain gages were compared and exhibited similar responses. The authors show the multi-probe technique provides detailed spectral analysis to detect flutter response in both rotating and stationary reference frames, with the ideal transducer configuration having equally spaced sensors around the rotor circumference.

Most recently, a comprehensive study of the first torsion vibratory response for different loading conditions of the embedded stage (Rotor 2) of the Purdue 3-Stage axial research compressor was completed (Murray & Key, 2014 & 2015; Smith, Murray, & Key, 2016). This study performed highly detailed measurements including blade tip-timing, characterization of vortical and potential forcing functions with radial total pressure probe traverse and radial hotwire cross-film traverse, and unsteady pressure fluctuation in the tip clearance region over the rotor and through a downstream stator vane passage with fast-response pressure transducers. The culmination of these detailed measurements provides researchers an extensive dataset of aerodynamic and tip-timing data associated with the first torsion vibratory response of a rotor. Pressure transducers with sufficiently high frequency response in a downstream stator vane passage were used to detect vibration of the upstream rotor. The unsteady pressure data were acquired and processed in a similar fashion as previous studies by subtracting the steady portion from the transient sweep through resonance and Doppler shifting the reference frame. The frequency content of the signal was computed, and the unsteady pressure data were compared with tip-timing data with results indicating forced response vibration.

## 1.5 Tip Clearance Flows and Over-Rotor Measurements

Rotor tip clearance flows in axial compressors occur in the spacing between the rotor blade tip and the casing endwall. As temperatures and loading change based on operation requirements, the size of these gaps will vary. Endwall region flows have a strong influence

on overall performance and stability. Wisler (1985) suggests more than half of the loss in an axial compressor is associated with the flow in the endwall region. Storer and Cumpsty (1994) report that while as much as 30 percent of the total loss in compressors is sometimes attributed to flow through the tip clearance, 10 percent may be a more realistic contribution of total loss.

Initial investigations of turbomachinery tip clearance flows led to the development of models to describe them. Flow models developed by Lakshminarayana (1965 & 1970) predicted tip clearance flows and have been compared extensively to later developed tip clearance models as a baseline. These early studies were performed with cascade models, and while unable to demonstrate important relative frame effects, they proved very useful in the investigation of flow dynamics of rotating machinery. Their relative simplicity, both logistically and economically, allows cascade studies to be widely performed and continue to provide insight into turbomachinery flow physics.

### 1.5.1 Defining Rotor Tip Clearance Flows

The rotor tip leakage flow is driven by a pressure gradient between the higher-pressure side of a blade, the blade pressure side, and the lower pressure side of the blade, the blade suction side. To alleviate this pressure gradient, a jet of fluid is driven from the area of highest pressure to the area of lowest pressure, or from the pressure side to the suction side over the rotor tip (Lakshminarayana and Horlock, 1965; Zhong et al., 2013). Figure 1.6 shows an illustration of the primary and secondary flow structures in a rotor blade-row passage, including tip clearance flows.

The rotor tip leakage vortex is formed by a shear layer interaction between the passage primary flow and the tip leakage secondary flow. As the tip leakage jet is transported across the rotor tip and encounters the bulk through-flow, the shear layer between the two flows results in the roll-up of a vortex sheet (Lakshminarayana and Horlock, 1965; Storer and Cumpsty, 1991; Chen et al., 1991). Figure 1.7 shows an illustration of the formation of the tip leakage vortex roll-up as the tip leakage jet interacts with the shear layer.

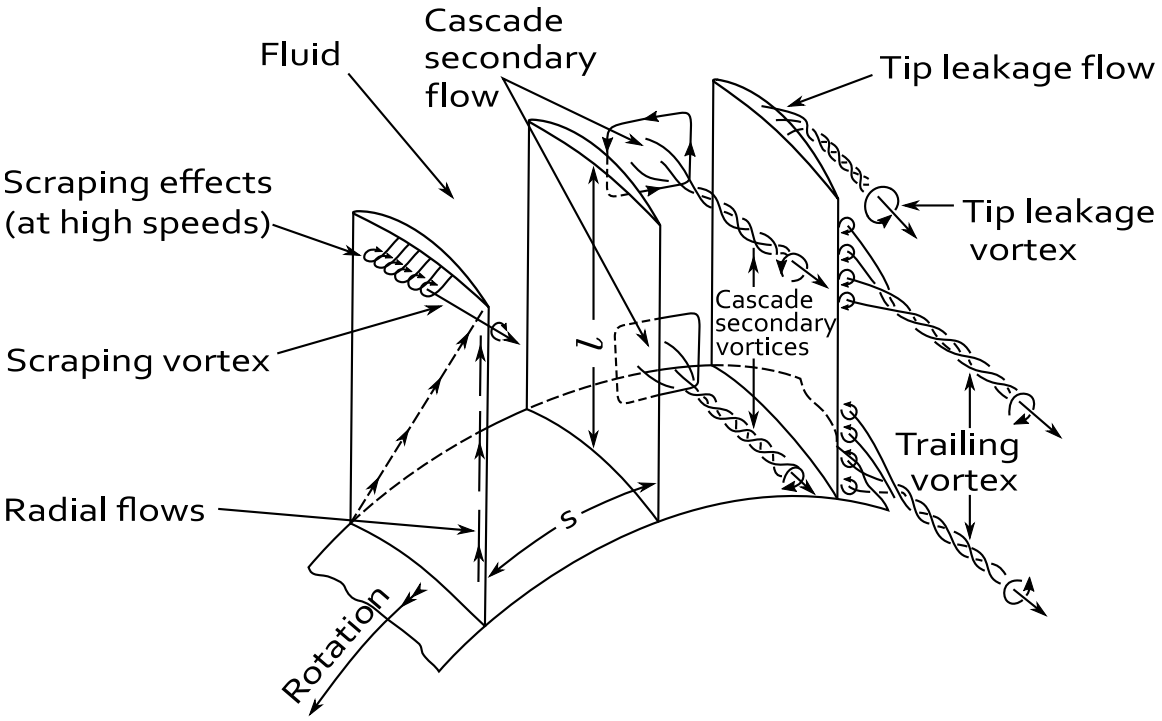


Figure 1.6: Illustration of primary and secondary flow structures in a rotor blade-row, from Lakshminarayana and Horlock (1965).

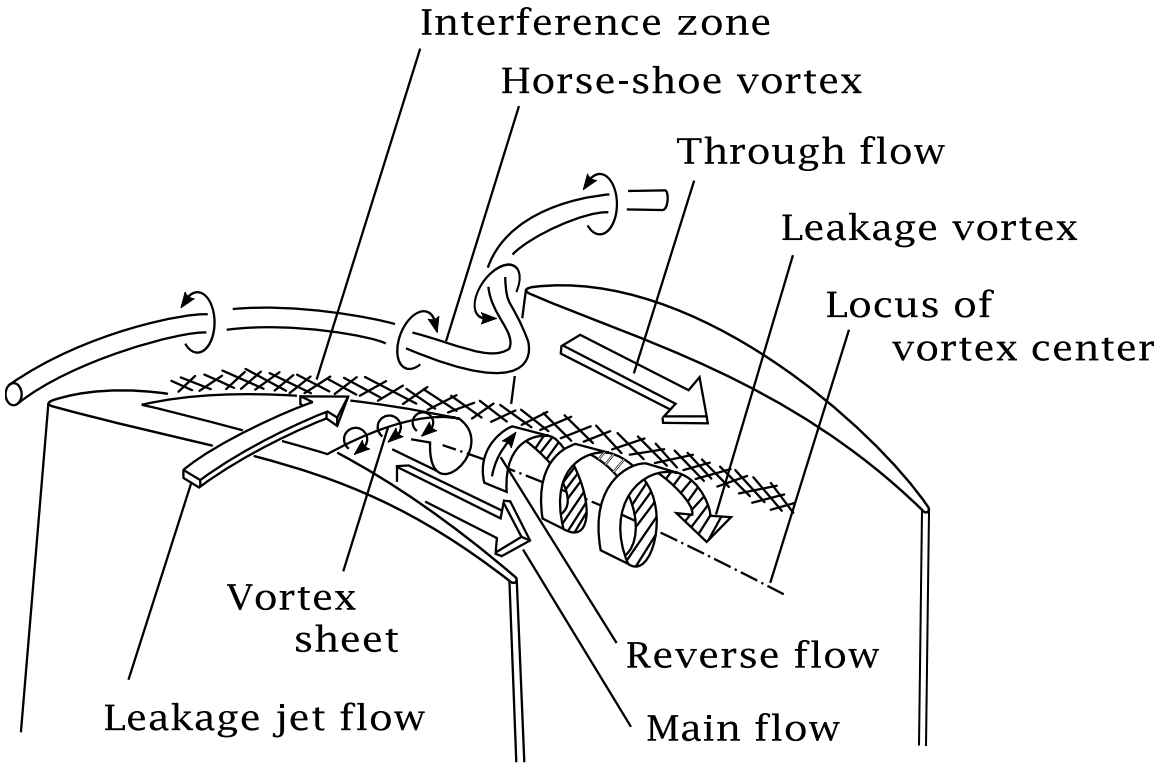


Figure 1.7: Illustration of the tip leakage vortex formation, from Inoue et al. (1989).

### 1.5.2 Quantifying Tip Leakage Flow Effects on Machine Performance

There are two aspects of tip leakage flow: one is blockage, a fluid dynamic effect, and the other is loss, a thermodynamic effect. Blockage is the reduction in freestream or core flow area due to local velocity defects and is analogous to displacement thickness in boundary layer theory. Several methods have been used to quantify blockage. Khalid et al. (1999) conducted computational and experimental studies and developed a simplified analysis estimating the endwall blockage with trends captured to better than 10 percent. Suder's (1998) investigation of blockage effects concluded blockage in the endwall region was 2–3 times greater than the core flow region, and furthermore, this increased blockage can be primarily attributed in part to tip clearance flow and shock/tip leakage vortex interaction. Most recently, Berdanier (2015) characterized and quantified the velocity defect region associated with leakage flow based on the procedure introduced by Suder and calculated blockage downstream of embedded stage blade-rows with thermal anemometry. Koch and Smith (1976) developed a method for calculating design point efficiency potential, proposed design parameter correlations, and quantified sources of loss in axial flow compressors. A conclusion of this study was that an efficiency decrease is caused by mass flow rate deficits in the endwall boundary layers. This study, however, did not differentiate between hub and casing endwall boundary layers, and the effects, instead, were summed together.

### 1.5.3 Effects of Clearance on Tip Clearance Flows

Research performed by Inoue et al. (1986, 1989) measured the stage performance and tip flow structure changes with changes in tip clearance. Experiments were conducted on two isolated axial compressor rotors with similar blade profiles but different solidities using a phase-locked multi-sampling technique with a slanted hotwire probe in the tip clearance gap and high-frequency response pressure transducers set in the casing wall. For the smallest clearance (about 0.56% relative to blade span), the leakage jet flow was stronger near the leading edge and reacted with the through-flow. As clearance increased, the position of maximum pressure difference between the pressure and suction surface of the blade moved downstream, resulting in a stronger leakage jet flow downstream. At the largest tip clearance (about 5.6% clearance relative to blade span), a reversed flow develops

due to the leakage flow vortex roll-up. The location of leakage flow roll-up coincides with the location of minimum wall pressure. As tip clearance is increased, the position of the roll-up onset moves downstream, and the vortex center moves toward the casing endwall. In the case of the higher solidity rotor (about 1.33 times the solidity of the lower solidity rotor) with a large tip clearance, the tip leakage flow region extends across the passage to the adjacent blade. The tip leakage vortex moves radially inward, towards the hub and interacts with the adjacent wake behind the rotor. The authors conclude increased tip clearance has a negative effect on stage performance by reducing both power and efficiency.

A study by Gbadebo et al. (2006) compared three-dimensional numerical computations carried out with ten levels of tip clearance (0 to 2.18% of blade chord) with experimental results at zero and 1.7% chord tip clearances. Three-dimensional separations on the suction surface of the blade observed at smaller tip clearances were largely removed for larger tip clearances (above 0.58% chord) by the clearance flow. This was attributed to the suppression of the leading edge horseshoe vortex and the interaction of the tip clearance flow with the endwall boundary layer. This interaction leads to a newly formed three-dimensional separation line on the suction side near the endwall, consequently rolling up into the clearance vortex. Dong et al. (1987) similarly reported that tip clearance controls three-dimensional separation on the near endwall suction surface. In addition to the previously mentioned studies, McDougall et al. (1990) reported that removal of corner separation at the stator hub is attributed to the tip leakage flow energizing the low momentum fluid in the suction side corner endwall.

### 1.5.4 Over-Rotor Measurements of Tip Clearance Flows with High-Frequency Response Pressure Transducers

Many studies have utilized fast-response pressure transducers for over-rotor measurements of the endwall pressure fluctuations in the tip clearance region. If properly designed, these experiments can provide high-fidelity representation of the flow physics near the casing. Work performed on a modern transonic fan (Shin et al., 2008; Hah and Shin, 2012) with a staggered array of fast-response pressure transducers installed on the casing wall over the fan measured the unsteady static pressures on the fan casing and were compared with

numerical predictions. These studies used the ensemble average method in addition to an ensemble root-mean-square (RMS) method to highlight the random disturbance level, or random unsteadiness, of the pressure signal. The authors cite the sensitivity of the ensemble average method to all forms of random unsteadiness as particularly effective in determining the location of features such as shocks and vortices. Measurements were compared with steady and unsteady computational fluid dynamics methods, each chosen for capabilities of resolving different flow features and characteristics, and were proven useful in the identification of flow features. As expected, results show that high levels of ensemble average static pressure are associated with the leading edge oblique shock, the tip leakage vortex, and the passage shock.

Recent notable comprehensive tip clearance flow investigations have used extensive complementary instrumentation techniques to understand and explain clearance flow physics. Ernst et al. (2010) conducted research on a two-stage axial compressor with an inlet guide vane conducive for special measurement objectives including rotor-stator axial spacing and stator indexing. Unsteady pressure measurements, acquired with fast-response pressure transducers mounted in probes, the axial gap, and tip leakage flow region, were locked to the shaft revolution via a 1/rev encoder allowing the signal to be ensemble averaged and the root-mean-square (RMS) to be computed. Unsteady total pressure measurements acquired downstream of all blade-rows characterize the RMS total pressure distribution at blade-row exit planes. These exit plane measurements identified important flow structures: the tip clearance vortex, blade-row wakes, clearance vortex-stator wake interaction, and hub boundary layer behavior. Over-rotor static measurements typify the endwall time-resolved ensemble average pressure distribution, distinguishing the tip clearance vortices and their trajectories, upstream wakes from stationary rows, blade-wake interactions with the rotating blades, shock formation on the suction side, and circulation and separation near the leading edge. In addition to the detailed evaluation of flow physics, frequency analysis of pressure transducers and strain gages is used to establish a method for the detection of flow phenomena induced by rotor-stator interaction and indexing effects as well as their propagation through a multi-stage environment. Of note, the author shows the stator reference position (zero clocking) shows most pronounced amplitude from

frequency analyses of collected strain gage signals. This is explained by the propagation of stator wakes downstream impinging on the leading edge of consecutive vane-rows. Downstream wake impingement from the upstream blade-rows cause increased loading and higher amplitude response at the downstream vane-row leading edge, and is discussed in detail by Key et al. (2009 & 2010) and Müller et al. (2007). The potential flow field influence, and therefore blade loading, on the upstream rotor by the downstream stator is maximized in this impinging configuration. When the stator is traversed about one-half pitch from the reference position, the wake passes through the consecutive vane passage without interaction. The alternating behavior in blade loading causes a resulting sinusoidal distribution of blade force of rotors and stators.

An exhaustive tip clearance study (Berdanier and Key, 2015) in the same facility as the present investigation (explained in detail in Chapter 2) was performed to characterize the fundamental flow physics and overall performance effects of increased rotor tip clearance heights in axial compressors. Data acquired in a multi-stage environment, including the important embedded stage, at three different tip clearances, four different speedlines, and two different operating conditions culminated in an extensive openly available database on multi-stage compressor flow of the rear stages of a high-pressure compressor with large relative tip clearances. The facility is unique from those reported in many studies because it is a multi-stage, non-repeating stage machine operating at engine-representative Reynolds numbers and Mach numbers. Three different tip clearance casings—1.5%, 3%, and 4% of the blade height—are the vehicles for a study of this magnitude. Steady and unsteady measurement techniques supporting this study include fast-response pressure transducers—mounted in the casing upstream of and over the rotor, installed in a Kiel probe for flow field traverse, and flush-mounted in the pressure and suction sides of a stator vane passage—seven-element total pressure and total temperature rakes upstream and downstream of each row, casing static pressure taps, thermal anemometry, capacitance probes for dynamic tip clearance measurement, flow-visualization, and particle image velocimetry. The methods used in the present investigation closely follow techniques developed and used in this study. Broad results show trends of decreasing efficiency with

increasing tip clearance, and the reduction of stall margin and stage matching ability caused by increased tip clearance flows.

## 1.6 Unsteady Aerodynamic Loading: Blade-Row Interaction and Blade-to-Blade Variability

Trailing each blade of a turbomachine is a viscous wake, a region of velocity deficit fluid shed from the boundary layer of the blade. These wakes impose forcing functions on downstream blade-rows resulting in oscillatory blade loading. Wakes and leakage flows are the primary unsteady flow structures generating unsteady pressure distributions and resulting unsteady blade forces in turbomachines. These vortical flow disturbances can persist for several rows through the machine, interacting with the downstream blade-rows and flow features.

Earlier analytical and experimental studies (Kemp and Sears; 1954, Meyer, 1958; Lefcort, 1965; Kerrebrock and Mikolajczak, 1970) developed models for wake transport through blade-rows. Kemp and Sears approximated viscous wakes from single airfoil experiments and then calculated the unsteady force and moment on a downstream blade passing through such wakes based on the theory of isolated thin airfoils in non-uniform motion. Meyer analytically determined the time-dependent pressure gradient and velocity of the case of two-dimensional incompressible flow through lightly loaded cascades.

Lefcort produced fundamental work of wake interactions in a water table experiment where an airfoil immersed in two-dimensional water flow experienced wakes generated by a cylindrical wake generator traversed upstream of the airfoil. Using piezoelectric transducers, one of the earliest characterizations of the unsteady pressure distribution over an airfoil during the passage of a wake was experimentally determined. Lefcort proposed forces in turbomachines can be considered as owing to four main effects: the circulation effect, caused by circulation about blades of the moving adjacent blade rows; the blade-thickness effect, caused by the presence of the potential flow fields about blades of adjacent blade rows due to the finite thickness of the blades; the wake effect, unsteady velocity fields induced at the blade by wakes shed upstream and assumed to be swept downstream

with the freestream velocity; and the wake-distortion effect, distortion of the wake though wake chopping. In the relative frame, the wake can be considered a jet approaching the blade. When the jet reaches the leading edge, it is cut in two, commonly referred to as wake chopping, and the two halves are distorted; one half of the jet contracts and the other half spreads out on the blade surface.

Capece et al. (1986) utilized a three-stage research compressor to investigate multi-stage blade-row interaction gust aerodynamics for the first time. Phase-locked average revolutions of time-variant datasets, consisting of two-wire thermal anemometry (cross configuration) and high-frequency response pressure transducers embedded in the pressure and suction surfaces of two different vanes, were calculated from the raw time series and subsequently Fourier decomposed. The spectra of the pressure signal contained a dominant fundamental blade-pass frequency with much smaller higher harmonic components and minimal non-harmonic content. This investigation determined that complex unsteady aerodynamic loading on downstream blade-rows is directly related to the forcing function on the blade row, and the forcing function itself is affected by multi-stage blade-row interactions.

Sanders and Fleeter (1997, 2001) performed experiments in a transonic one and a half stage research axial fan investigating multi-stage interaction effects on rotor blade-to-blade wake variability and the resulting aerodynamic response of the downstream vane-row. This was done at different speeds and clocking configurations using a cross-film probe, unsteady static pressure probe, and fast-response pressure transducers reverse mounted within the suction and pressure surfaces of adjacent vanes. Resulting ensemble-averaged measurements quantified multi-staging effects at several inlet guide vane clocking positions relative to the downstream stationary probes where the rotor wakes changed markedly with vane traverse, with both the wake shape and blade-to-blade variability affected.

Boyd and Fleeter (2003) experimentally investigated axial compressor unsteady aerodynamic response generated by the interactions of rotor blades with the upstream inlet

guide vane of a two-stage research compressor with the purpose of investigating statistical viability of using an average wake to represent flows around the machine annulus. Rotor-based instrumentation was accomplished with a rotating cross hot-wire probe and fast-response static pressure transducers installed along the midspan of four of the first stage rotor blade pressure and suction sides. The ensemble average and RMS were computed along with an overall average and RMS, termed the grand average and grand standard deviation. The transverse and streamwise gust components of the wake ensembles were then compared against their respective grand averages using the Smith-Satterthwaite test—comparing two independent random samples assumed to come from normal distributions with unequal variances. The results of this test determine whether the grand average is a good representation of the wakes and whether wake-to-wake variability is due to chance or is attributed to physical cause. Additional statistics were computed using streamwise and transverse velocities for the forcing function and the unsteady lift and moment coefficients for the rotor blade response. To determine the joint variability of the blade-to-blade variability and the unsteady aerodynamic response variability, the probability distribution, covariance, and correlation coefficient were computed. Results of these tests showed variation of the wakes and aerodynamic response vary by as much as 100%, and the blade-to-blade variability of the forcing function and aerodynamic response were significant. Additionally, the blade-to-blade streamwise and transverse components of the wakes varied significantly from their computed averages.

Recent studies in the same facility as the present investigation (Key et al. 2010; Smith and Key, 2017) quantified blade-to-blade and blade-row interactions of a three-stage machine using different measurement techniques. Key et al. quantified rotor wake variability driven by blade-row interaction using time-resolved flow angle data acquired with a cross-film sensor at midspan behind each rotor, spanning 50 circumferential positions across the vane passage. The study includes wake variations caused by blade-to-blade variability, upstream rotor wakes, and interactions with the potential field of the downstream vane-row. The lowest levels of variability are associated with the first stage rotor, and increased blade-to-blade wake variability in the downstream rotors. Interaction between rotor wakes and upstream blade-rows cause an amplitude modulation in the ensemble average revolutions,

indicating higher variability. Smith and Key investigated how the pitchwise variations (vane clocking) at the embedded rotor exit affect surface pressures on the downstream vane in the embedded stage. A similar cross-film sensor acquired time-resolved flow angles and a fast-response total pressure probe captured the RMS total pressure exiting the second stage rotor as they entered a specially instrumented vane passage within the second stage stator. This vane passage has flush-mount high-frequency response pressure transducers in the neighboring pressure and suction sides. Results show significant contribution to the unsteady stator surface pressure occurring over a rotor revolution from interactions between the first and second stage rotors. Additionally, the rotor 1-rotor 2 interactions change in the pitchwise direction downstream of the rotor, and therefore, vane clocking affects change in downstream surface pressure. The tip leakage flow, measured at the exit of the embedded stage, also contributes to the downstream stator surface pressures measured near the tip region and provides an additional pressure peak with each blade-passing, resulting in more high-frequency content at twice the blade-pass frequency. Vane-row interaction, between the first and second stage stators did not occur directly, but the interaction between the first stage stator wakes and the second stage rotor cause a circumferentially varying flow field in the absolute reference frame, subsequently experienced by the second stage stator.

## 1.7 Research Objectives

The purpose of this research is the experimental investigation of unsteady aerodynamics and blade-row interactions of an embedded compressor stage with different upstream vane counts. Unsteady aerodynamic measurements acquired at corrected operating conditions near resonant mechanical conditions characterize the aerodynamic response of the forced response excitation and support the aeromechanic characterization of forced response vibration. Measurements associated with the forced response excitation of a higher order chordwise bending mode for a baseline (88EO) and reduced vane count (76EO) configuration and the first torsion mode for the reduced vane count (38EO) have been acquired with fast-response pressure transducers. Unsteady pressure measurements over the rotor in the tip clearance endwall region and through the downstream stator vane passage have been examined for steady-state operating conditions of two different loading

conditions. Examination of the unsteady pressure signals from the flow field comprising the embedded stage of the compressor have characterized aspects of the aerodynamic vortical and potential forcing functions, including the generation of the tip leakage vortex, blade-row interaction, and blade-to-blade variability.

The data acquired for this study is part of a comprehensive, detailed dataset characterizing the forced response of an embedded stage compressor rotor. This data has been made available to aeromechanics research partners in academia, industry, and government as part of the GUIde 5 consortium (Government Agencies, Universities, and Industry working together on a common goal). Research partners will be able to use this dataset to design and validate tools for the detection and avoidance of forced response vibration.

# 2. EXPERIMENTAL METHODOLOGY

## 2.1 Purdue 3-Stage Axial Compressor Research Facility

The Purdue 3-Stage axial research compressor is a scaled model of the rear stages of a modern high pressure compressor and comprises an inlet guide vane (IGV) followed by three axial stages. The compressor is capable of matching engine-representative Reynolds numbers and Mach numbers with a corrected design speed of 5000 rpm. The IGV and stators are shrouded on both inner and outer diameters, utilizing labyrinth knife-edge seals on the rotor drum to mitigate hub clearance flows between the inner shroud and rotor drum. Each of the rotors is machined as an integrally bladed rotor (IBR), or bladed disk (blisk). The blade profiles of the IGV and rotors are double circular arc (DCA) configurations while the stators take their profiles from a NACA 65-series airfoil design.

The compressor is driven by a 1400 horsepower three-phase alternating current motor. An encoder on the motor shaft and feedback control with the variable frequency drive maintain the shaft speed within 0.1% of the desired set speed. A gear coupling connects the low-speed shaft of a 5:1 speed-increasing gearbox and flexible disc couplings connect the high-speed shaft of the gearbox to the compressor through an inline torquemeter. Unconditioned ambient air is drawn from a screened settling chamber through a filtered 3.36:1 area ratio bell-mouth reducing the flow area to the 24-inch diameter inlet duct. Following the bell-mouth, airflow passes through a honeycomb flow straightener and an ASME standard long-form Venturi flowmeter. After the Venturi, the airflow travels through the remainder of an insulated 14-foot length of the inlet duct to an elliptical bullet-style nose cone reducing the annulus area 3.27:1 at the inlet to the 2-inch constant area annulus flowpath of the compressor. Aft of the compressor test section the flow passes a sliding throttle ring used to set the operating loading condition of the compressor to a collector and is finally exhausted out of the test cell.

## 2.2 Facility Configurations Supporting Rotor 2 Resonant Measurements

Two uniformly spaced stator vane configurations have been used to characterize their influence on resonant response of Rotor 2. The baseline configuration of the compressor has rotor blade counts of 36, 33, and 30 for Rotor 1 (R1), Rotor 2 (R2), and Rotor 3 (R3), respectively, and stator vane counts of 44 for IGV, Stator 1 (S1), and Stator 2 (S2), respectively, and a vane count of 50 for Stator 3 (S3). The flowpath cross-section and measurement stations is shown in Figure 2.1. Each stator vane-row is individually indexable allowing full vane passage characterization of probes and instrumentation through circumferential traverse. A reduced vane count configuration of S1 was manufactured with 38 vanes. The configurations are summarized in Table 2.1.

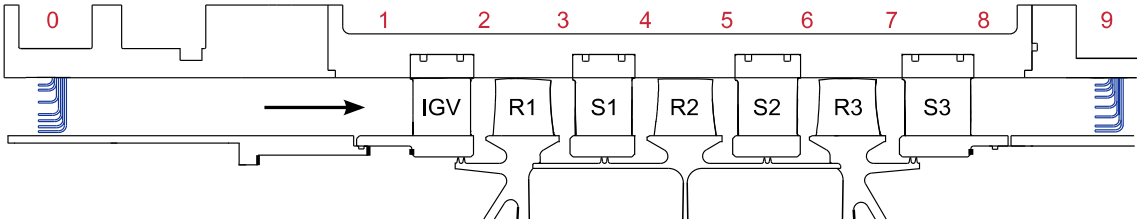


Figure 2.1: Cross section of the flowpath and measurement stations of the Purdue 3-Stage Axial Compressor Research Facility.

Table 2.1: Summary of facility configurations and vane counts.

| Configuration | IGV | R1 | S1 | R2 | S2 | R3 | S3 |
|---|---|---|---|---|---|---|---|
| Baseline | 44 | 36 | 44 | 33 | 44 | 30 | 50 |
| Reduced vane count | 44 | 36 | 38 | 33 | 44 | 30 | 50 |

## 2.3 Compressor Performance and Operating Loading Conditions

Experiments performed in this research have been designed to take advantage of the difference between mechanical and corrected conditions of a compressor in operation to investigate the steady-state and transient aerodynamics at operating points with corrected compressor speeds equivalent to mechanical resonance speeds located in and near

excitation modes of R2. Specifically, excitation of the upstream 88 engine order first-chordwise (1CWB) bending mode of the baseline configuration and the 76 engine order first-chordwise bending and 38 engine order first-torsion (1T) modes of the reduced vane count configuration have been studied.

The Rotor 2 Campbell diagram for the different compressor configurations is shown in Figure 2.2. Blue circles mark the engine order crossings considered in this study. Another crossing occurs at the 44EO-1T engine order crossing with the baseline stator count; this condition has been studied extensively by Murray (2014). Resonant responses are shown in red and have been experimentally determined by Murray (2014) and Aye-Addo (2016) with NSMS measurements. Steady-state and transient data were acquired at two loading conditions: peak-efficiency (PE) and high loading (HL). Loading conditions, corrected to standard day conditions, were set using the methods outlined in Berdanier et al. (2015) to account for the effects of humidity on the real gas properties and are shown on the compressor map in Figure 2.3 and summarized in Table 2.2. Mass flow rates in Table 2.2 are normalized by the design point mass flow rate.

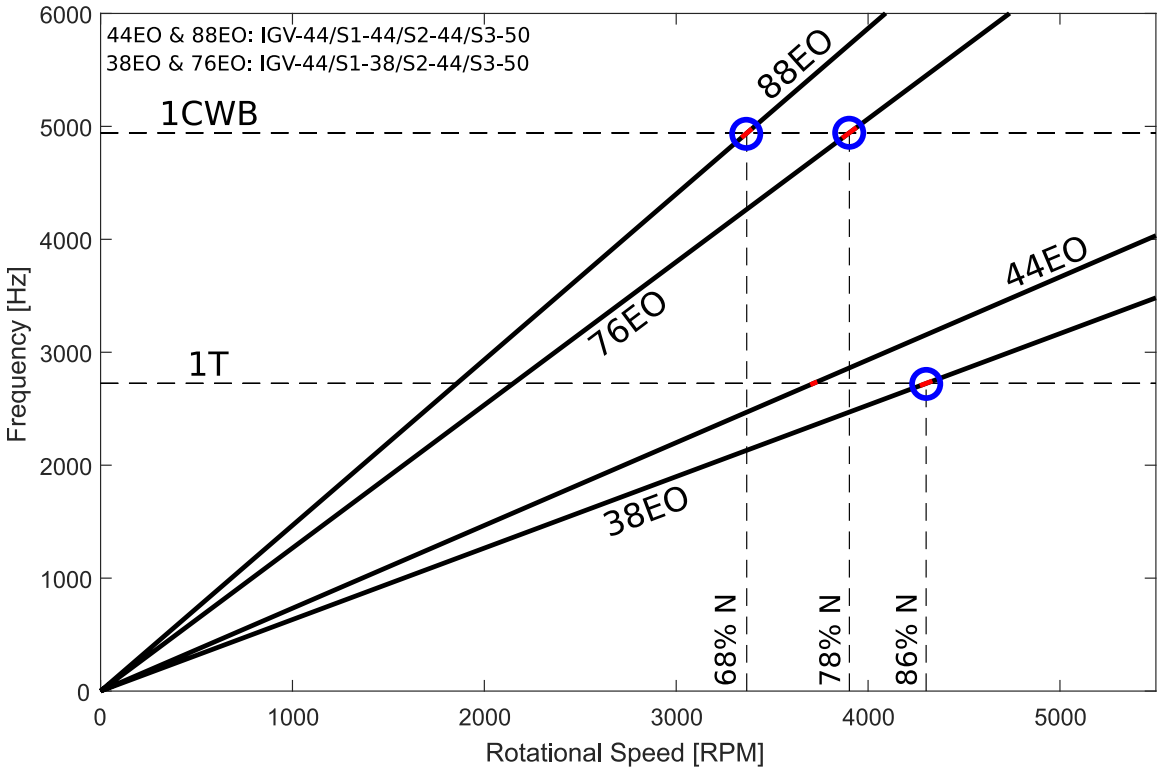


Figure 2.2: Rotor 2 Campbell diagram for different vane-count configurations.

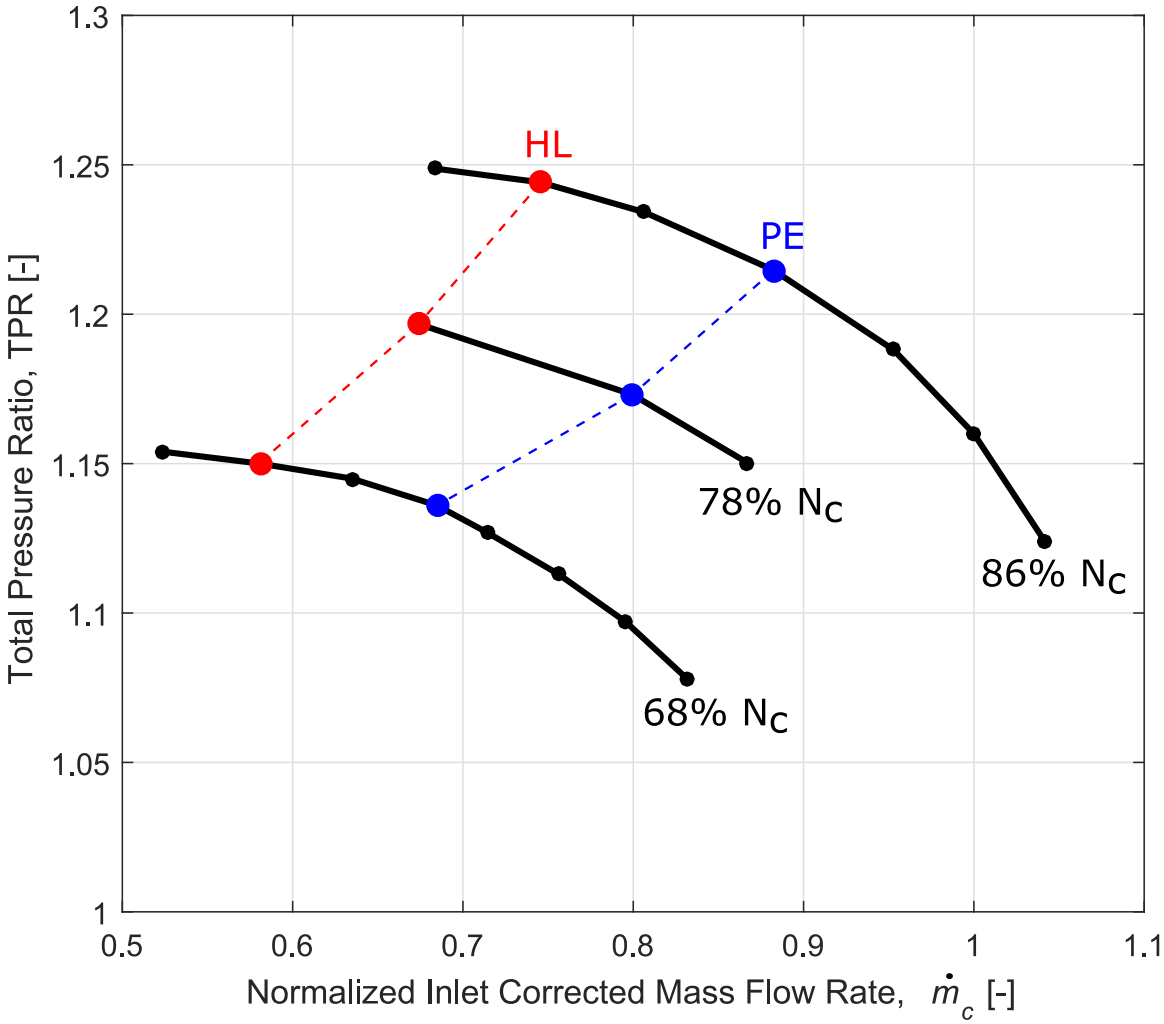


Figure 2.3: Compressor map with loading conditions and operating points associated with detailed steady-state and transient testing.

Table 2.2: Summary of compressor loading conditions and operating points associated with different modes of excitation.

| Corrected Speed | Mode of Excitation | Peak Efficiency (PE) | | High Loading (HL) | |
|---|---|---|---|---|---|
| | | Normalized $\dot{m}_c$ [-] | TPR [-] | Normalized $\dot{m}_c$ [-] | TPR [-] |
| 3400 rpm [68% $N_c$] | 88EO-1CWB | 0.68 | 1.14 | 0.58 | 1.15 |
| 3900 rpm [78% $N_c$] | 76EO-1CWB | 0.80 | 1.17 | 0.67 | 1.20 |
| 4300 rpm [86% $N_c$] | 38EO-1T | 0.88 | 1.21 | 0.75 | 1.24 |

## 2.4 Fast-Response Pressure Measurements

To capture the high-frequency fluctuations of pressure associated with rotor blade passing, fast-response pressure transducers were used to measure the endwall static pressure fluctuations over the rotor tip and the unsteady loading of a downstream vane passage.

### 2.4.1 Fast-Response Transducer Data Acquisition System

All of the sensors used in this study were Kulite ultraminiature and subminiature pressure transducers. A Precision Filters 28000 signal conditioning system installed with four Precision 28118 octal-channel full bridge amplification cards provides the voltage excitation and amplification necessary for the sensors. This system acquires data from 32 simultaneous channels and supports a variety of transducers. The signal conditioning system is controlled with an accompanying software used to adjust DC offset, gain, and analog anti-aliasing signal filter. The analog signals are then digitized with a National Instrument (NI) PXIe-1073 chassis installed with two NI PXIe-6358 capable of sampling 16 simultaneous analog inputs at 1.25 MHz, interfacing with the data acquisition computer through NI BNC-2110 connector blocks. This signal conditioning and data acquisition system is coupled with an optical laser tachometer aimed at the high-speed shaft of the speed-increasing gearbox creating a square wave used as a once-per-revolution (1/rev) trigger. The pulse train is relayed through a digital counter, providing an accurate rotational speed of the shaft. The 1/rev trigger also provides the ability to phase-lock each revolution of time-resolved data acquired on the compressor. Typical unsteady measurements at steady-state operating conditions were acquired with a sample rate of 300 kHz and analog anti-aliasing filter cut-off frequency of 100 kHz.

### 2.4.2 Over-Rotor Static Pressure Measurements of Embedded Stage Rotor

Windows on the compressor casing located over each rotor allow adaptable instrumentation to be installed into the casing. Flush-mounted fast-response pressure transducers instrumented into aluminum blocks can be installed in these windows to characterize the high-frequency fluctuations of static pressure in the endwall of the casing over the rotors. Two of these blocks, with 25 sensors installed in different arrays, were used

to collect data at steady operating conditions and during transient speed sweeps through resonant conditions.

The first block has a 5x5 array of Kulite XTL-140 subminiature pressure transducer sensors with standard protective B-type screens having an operational range of 0–5 psig (Figure 2.4a). This array covers 120% of the axial chord of R2 and 110% of one blade-passage. Figure 2.4 shows the sensor positions relative to a blade on R2. Technical specifications list the natural frequency of the transducer to be up to 150 kHz, but the installed screen reduces the dynamic frequency response to less than 20 kHz (Brossman, 2012). As an approximation, sensor frequency response should be five to ten times the highest frequency component contained in the signal. Dominating frequencies in the signal are associated with blade-pass frequency ($BPF$):

$$BPF = \frac{N_{\text{mech}} N_{\text{blades}}}{60} \tag{2.1}$$

where $N_{\text{mech}}$ is the rotational speed in rpm and $N_{\text{blades}}$ is the number of blades. Using this definition, the highest frequency of interest to this study expected in the signal is associated with 36-blade count of Rotor 1 (R1). Operating at 110% mechanical design speed, (5500 rpm) the blade-pass frequency of R1 is 3300 Hz or 3.3 kHz. The dynamic frequency response of the system is slightly more than six times the highest frequency component contained in the signal. Results from this instrumented block are not presented in this study, however the system description and calibration information are included for future work with the acquired data.

The second block has a linear array of 25 Kulite XCS-062 ultraminiature pressure transducers with standard protective B-type screens and an operational range of 0–5 psig (Figure 2.4b). This linear array spans 126.4% of the axial chord with the furthest upstream sensor located at -12.8% of the axial chord and the furthest downstream sensor 113.6% of the axial chord. The XCS-062 sensor has a smaller diameter than the XTL-140 sensor and allows for more spatial resolution of the axial span. Like the XTL-140, the installed screen reduces the dynamic frequency response. However, the cavity size behind the screen was

reduced to increase the greatest allowable frequency by filling it in with silicone material. This practice increases the frequency response to 30 kHz for these sensors (Berdanier, 2015). The dynamic frequency response of the system using these sensors is slightly more than 9 times the blade-pass frequency. Figure 2.5 shows each instrumented block used in this investigation.

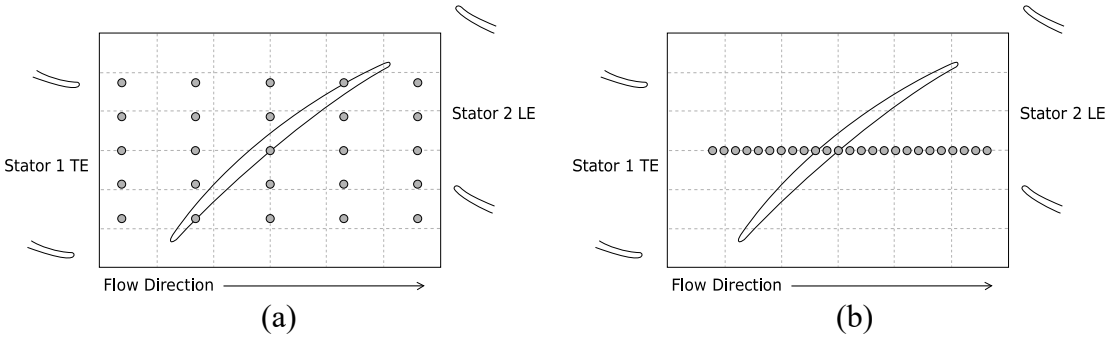


Figure 2.4: Sensor positions in 5x5 (2.4a) and linear (2.4b) arrays relative to R2 blades.

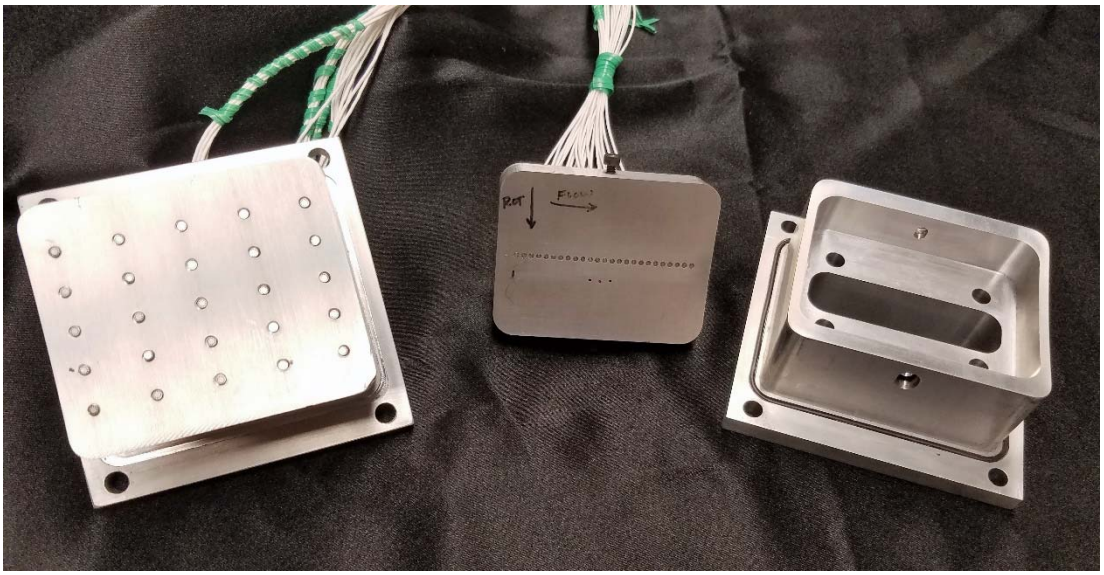

Figure 2.5: Instrumented blocks for over-rotor endwall static pressure measurements.

## 2.5 Static Surface Pressure Measurements of Embedded Stage Stator Loading

To measure the effects of the upstream rotor wakes on the unsteady loading of S2, a removable stator vane passage was previously designed and instrumented with Kulite LQ-062 ultraminiature pressure transducers with a 0–5 psig range. These sensors are different

from the over-rotor casing transducers as they operate in sealed-gage mode. The over-rotor casing transducers use the ambient conditions outside of the compressor as a reference pressure for measurements. Sealed-gage sensors do not operate this way, and instead, a reference pressure is taken at the time of balancing the sensors. These transducers do not have protective screens installed so the manufacturer specified frequency response of 100 kHz to 150 kHz can be expected. Upon delivery, only 15 of the 16 installed sensors were

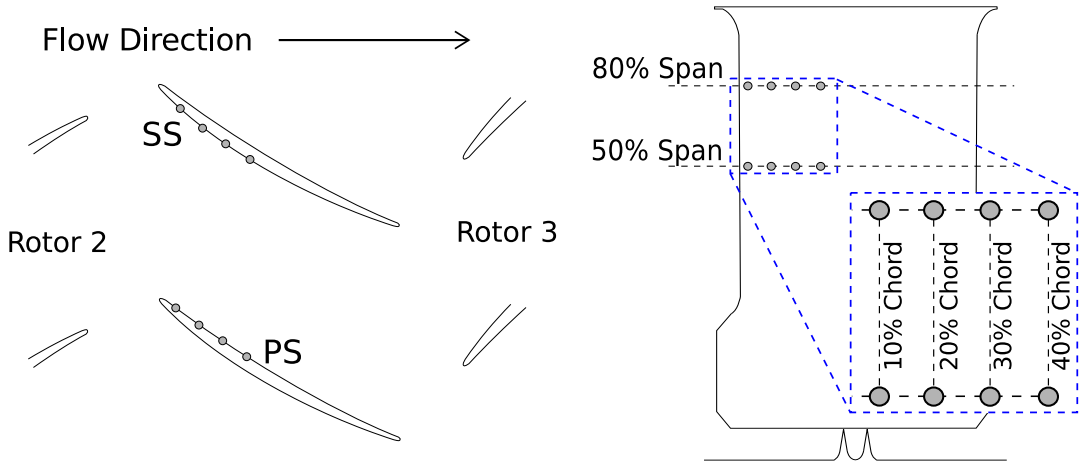


Figure 2.6: Kulite LQ-062 pressure transducer sensor locations in removable stator vane passage insert.

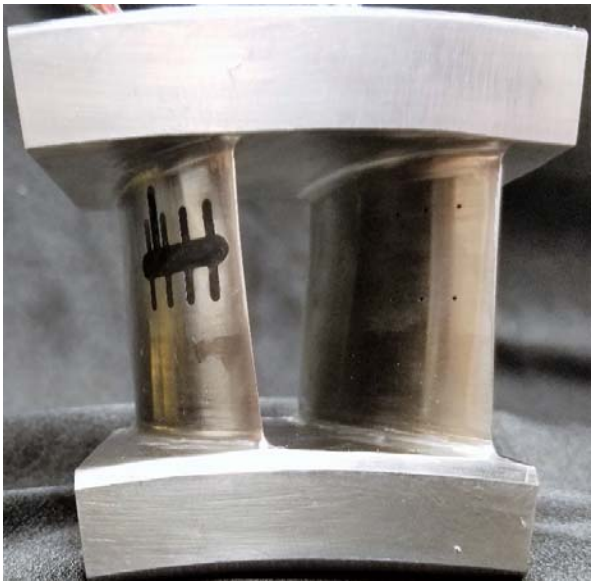

Figure 2.7: Removable stator vane passage insert instrumented with Kulite LQ-062 pressure transducers.

functional. Sensors are located at 10%, 20%, 30%, and 40% of the chord on the pressure side and suction side of the passage at 50% and 80% span of the stator vane from the hub. Figure 2.6 illustrates the positions of these sensors and the instrumented vane passage is shown in Figure 2.7.

## 2.6 Exit Plane Total Pressure Measurements of Embedded Stage Rotor

A single element Kulite LQ-062 ultraminiature pressure transducer with standard protective B-type screen installed in a Kiel head probe is used to acquire time-resolved total pressure measurements at the R2 exit plane (Figure 2.8). The sensor operates in sealed-gage mode and has a pressure range of 0–5 psig. The Kiel head surrounding the transducer element has a diameter of 0.083 in. and a flow acceptance cone of 30°. With the installed screen, this sensor has an expected frequency response of about 20 kHz.

Figure 2.8: Kulite LQ-062 pressure transducer installed in Kiel head probe.

## 2.7 Pressure Transducer Calibrations

The pressure transducers were subjected to known pressures from an Omega DPI 610 high accuracy pressure calibrator in a custom pressure calibration chamber with interchangeable bulkheads to accommodate the different instrumented blocks. The Omega DPI 610 has an internal pressure range of -15 to 30 psig and an accuracy of 0.025% full-scale. Voltages from the transducers and pressure measurements from the chamber were then acquired simultaneously to obtain the calibration slope of each sensor. Nominal sensitivities were

provided by the manufacturer, but it is standard practice to perform a static calibration of each sensor before using them to acquire any data. The XTL-140 sensor has a nominal sensitivity of 20 mV/psi, and with an applied gain of 50, the calibrated slope for this sensor is 1 psi/V. The XCS-062 sensor has nominal sensitivity of about 25 mV/psi and with a similar applied gain of 50 the linear calibrated slope for the sensor is 0.800 psi/V. The LQ-062 sensor has nominal sensitivity of 10 mV/psi, and with a gain of 100, the linear calibrated slope for this sensor is 1 psi/V. All sensors have accuracy of ±0.1% of full-scale output as stated by the manufacturer, this includes the combined non-linearity, hysteresis, and repeatability. With the stated accuracy and the nominal full-scale outputs of 100 mV for the XTL-140 and LQ-062 transducers and 125 mV for the XCS-062, uncertainties in the voltage measurements are 0.1 mV and 0.125 mV, corresponding to 0.005 psi. Additionally the compensated temperature range for all transducers is +80°F to +180°F. Figure 2.9 displays experimental data in black and the average of the sensitivity provided by the manufacturer for each sensor in red.

Difficulties in repeating previously calibrated values of the stator vane passage insert transducers led to the design and manufacture of a new bulkhead for the calibration chamber. Previously, the stator vane passage insert was calibrated with a separate calibration chamber than the over-rotor sensors, with the pressure transducer leads being bundled and routed out of two holes. Teflon thread-sealing tape and liberal use of silicone sealant were applied to help maintain constant pressure in the chamber; however, it was difficult to sustain pressure in this chamber. The new bulkhead design routes separate transducer leads through smaller individual openings to allow better individual sealing. The new chamber bulkhead and improved data acquisition has allowed better sealing greatly reduced hysteresis between measurement systems resulting in calibration slopes closely matching the nominal sensitivities of the transducers. Data acquired with the previous calibration chamber bulkhead suffered a large deviation from the nominal sensitivity. Data acquired with the new calibration chamber bulkhead, shown in Figure 2.10 shows experimental data in black and the average manufacturer provided sensitivity in red. Coefficients of determination ($R^2$ values) for each best-fit straight line are no less than 1.000 and have an average value of 1.0000 over all sensors calibrated.

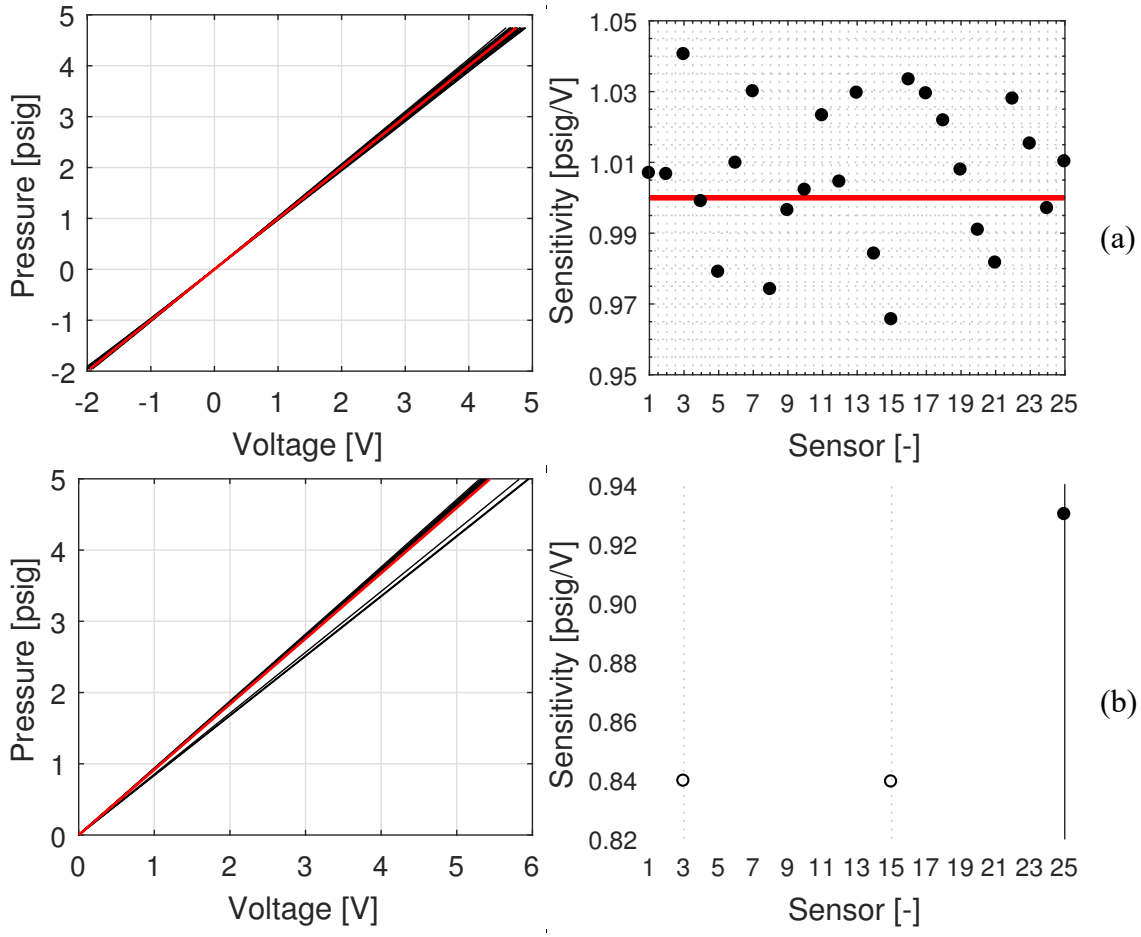


Figure 2.9: Best fit straight lines and sensitivities for the XTL-140 (2.9a) and XCS-062 (2.9b) pressure transducers.

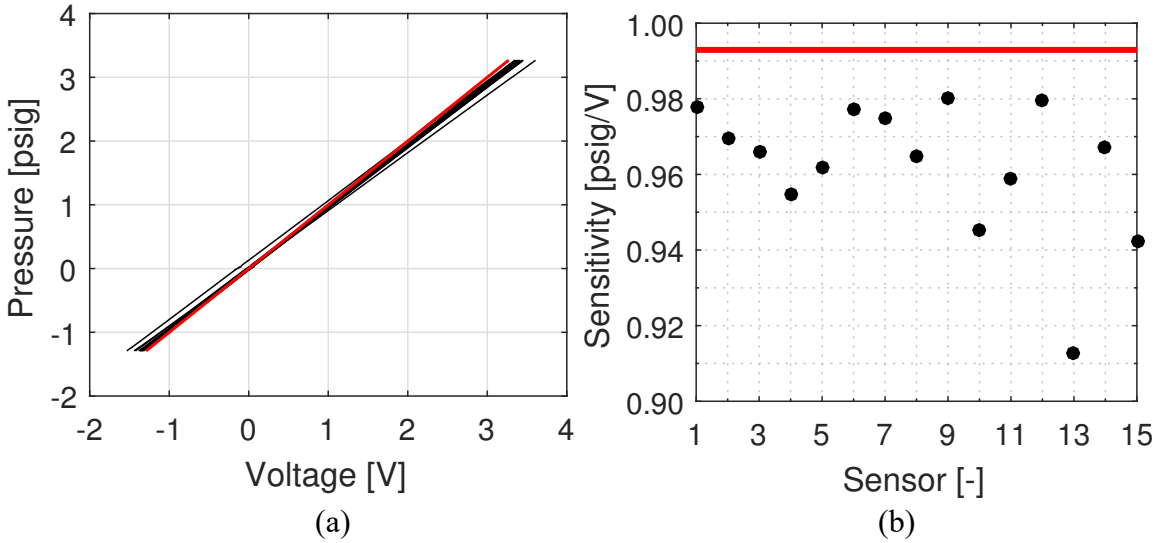


Figure 2.10: Best fit straight lines and sensitivities for the LQ-062 pressure transducers.

Figure 2.9 and Figure 2.10 show the importance of in-situ calibrations of the sensors. While several of these sensors have sensitivity closely matching the sensitivity provided by the manufacturer, some sensors have an almost 10% different sensitivity than the average of those provided by the manufacturer. In fact, the averages of the manufacturer provided sensitivities for the sensors are as much as 13.8% different from the nominal sensitivity stated on the sensor's datasheet. Figure 2.11 includes the pressure calibration chamber and bulkheads used for the calibration of the pressure transducers of this study.

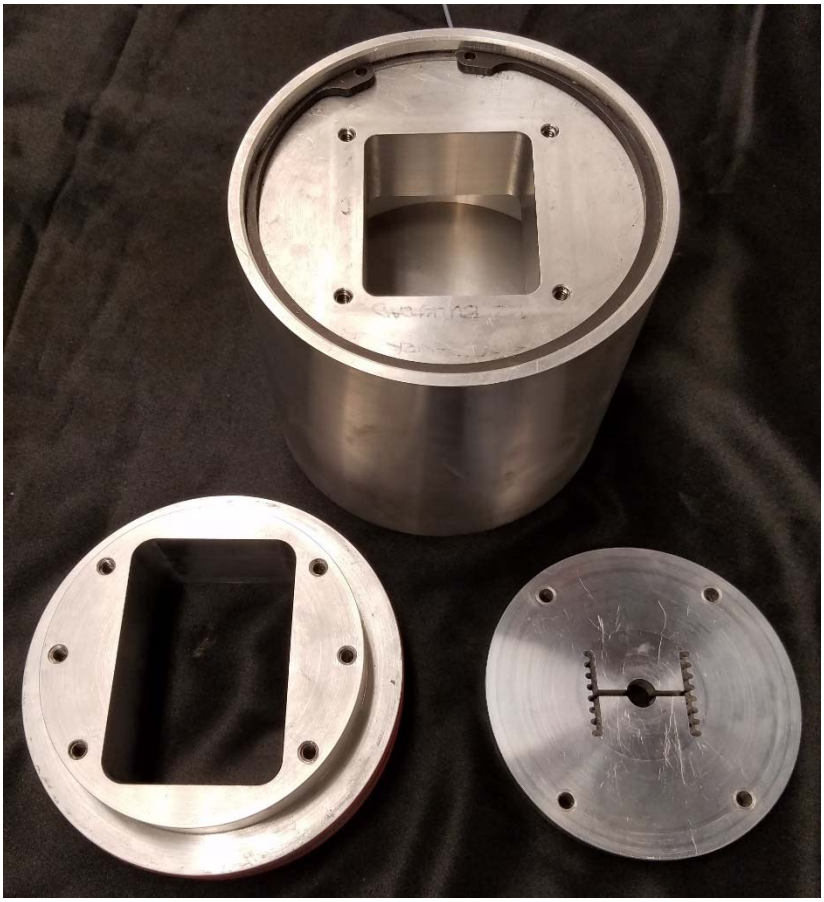

Figure 2.11: Pressure calibration chamber with R2 window bulkhead installed (top) and new S2 vane passage insert bulkhead and lid (bottom).

# 3. TIME-RESOLVED PRESSURE MEASUREMENTS OF EMBEDDED STAGE ROTOR

## 3.1 Data Processing Techniques Applied to Unsteady Pressure Data

Signals acquired with fast-response pressure transducers are phase-locked and time-resolved with a 1/rev signal from the optical tachometer on the compressor high-speed driveline. Data have been collected at a sampling rate of 300 kHz with a low-pass anti-aliasing analog filter cut-off frequency of 100 kHz for a total of 300 revolutions for the baseline configuration and 400 revolutions for the reduced S1 vane count configuration. These are statistically sufficient numbers of samples to represent phase-locked ensemble averages of the measured pressures. For the steady-state compressor loading conditions and acquisition time scales, the signal can be assumed a stationary process, allowing the time series signal to be partitioned into ensembles of single revolution measurements and averaged to produce an ensemble average revolution of data, example Figure 3.1, using the formula

$$\langle P(t_{\mathrm{i}})\rangle = \frac{1}{N}\sum_{\mathrm{k}=1}^{N}[P(t_{\mathrm{i}})]_{\mathrm{k}}\,, \tag{3.1}$$

where $P$ denotes pressure and $N$ is the total number of samples, and is defined for each revolution k and each time i. The angle brackets denote ensemble averaged values.

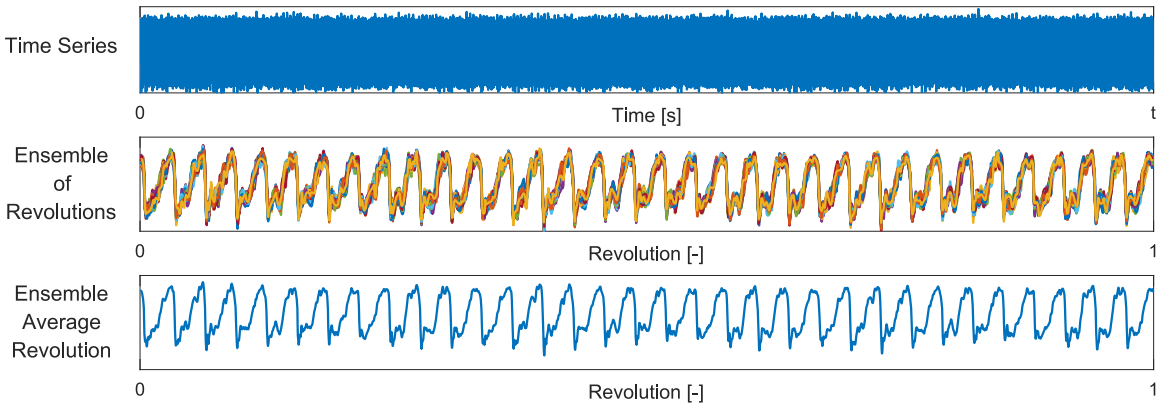


Figure 3.1: Example of the ensemble averaging of a stochastic time series.

This data acquisition technique is repeated for several pitchwise locations by traversing the individually indexable stator vanes together. The target position for the vanes is calculated based on the lowest vane-count of the four stationary rows installed in the casing at a given time, ensuring the vane-rows are moved as a block and at least one full passage of each vane-row is covered during the traverse. After each raw time history is acquired, an ensemble average revolution defining the pitchwise location may be obtained.

Further averaging techniques have been applied and are illustrated in Figure 3.2, as adapted from Smith et al. (2015). The ensemble average revolutions, shown in black, calculated for each vane passage position can be averaged across a stator pitch to represent a mean passage ensemble average revolution, shown in blue, or across the circumferential ensemble average revolution to obtain a mean measurement representing the average of the circumferential location, shown in green. The mean measurement is also referred to as a mean blade passing or blade-pass period (BPP). Either mean value can be averaged across the mean revolution or the mean measurement, respectively, to obtain an overall mean vane passage or overall blade-pass period measurement characterizing the loading condition. The mean passage ensemble average is useful for highlighting blade-to-blade differences

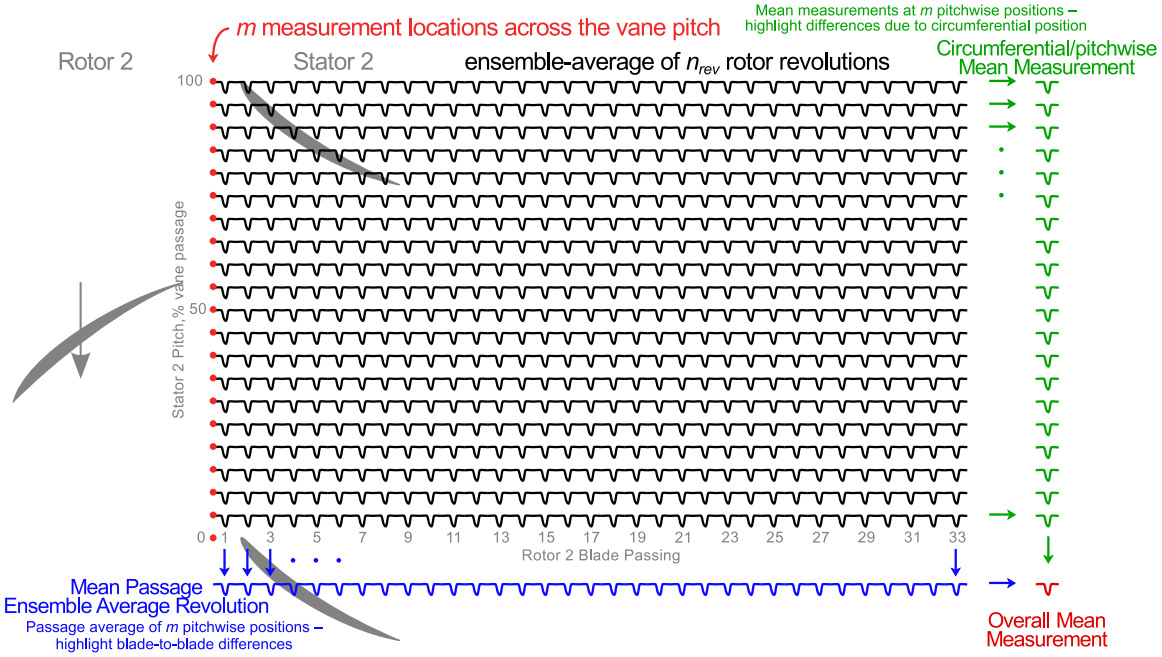


Figure 3.2: Illustration of averaging techniques used in this analysis.

whereas the circumferential mean measurement highlights differences due to pitchwise location.

For a frequency spectrum analysis, an ensemble average revolution is replicated for the same number of revolutions as the acquired signal. Ensemble averaging the time history increases the signal-to-noise ratio and distinguishes shaft frequency components; replicating this ensemble average revolution increases the resolution in the frequency domain. The periodic replicated ensemble average signal does not need to be windowed; hence, no window power compensation is necessary to correct the gain of the attenuated signal frequency amplitudes. Figure 3.3 shows a comparison of the frequency spectra, normalized to the maximum amplitude density value of the replicated ensemble average, with different window functions applied to the pressure time history without compensation to investigate signal amplitude attenuation caused by windowing.

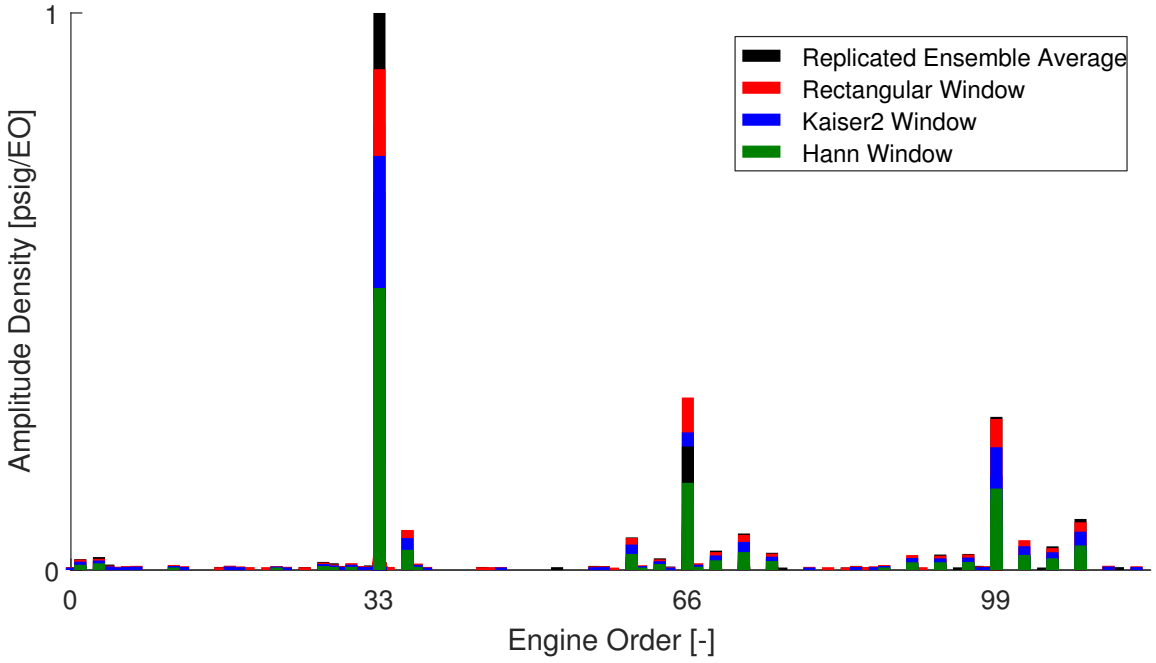


Figure 3.3: Comparison of the effects of window amplitude attenuation against the replicated ensemble average.

The root-mean-square (RMS), also known as the standard deviation in statistics, with respect to the ensemble average pressure signal,

$$P_{\mathrm{RMS}}(t_{\mathrm{i}}) = \sqrt{\frac{1}{N}\sum_{\mathrm{k}=1}^{N}[P(t_{\mathrm{i}}) - \langle P(t_{\mathrm{i}})\rangle]^2{}_{\mathrm{k}}}\,, \tag{3.2}$$

is calculated by summing the squared difference between pressure and ensemble average pressure at each time point, finding the arithmetic mean of the squared values, and then finally taking the square root of the result. The RMS with respect to the ensemble average pressure is useful for further highlighting unsteadiness in the pressure fluctuations.

## 3.2 Characterization of Rotor Tip Clearance Flow in the Embedded Stage

Static pressure data were acquired over Rotor 2 with the linear-array pressure transducer window for corrected speeds associated with the 88EO-1CWB baseline vane configuration engine order crossing and the 76EO-1CWB and 38EO-1T reduced count vane configuration crossings. At each crossing, a 20-point circumferential traverse of the vane passage was performed for the PE and HL conditions. These data were subsequently ensemble averaged for each vane position and further averaged to get a mean blade-pass period for each vane position. These pitchwise mean blade-pass periods were also averaged to get an overall mean measurement of the loading condition. All over-rotor contours have been repeated to show a full rotor passage, assuming circumferential periodicity around the machine annulus, and the abscissa features markers showing the axial locations of the sensors used to produce the contour. The colorbar axis values have been normalized by the area-averaged inlet total pressure measured at the aerodynamic inlet plane. Limits of the ensemble average pressures have been chosen to be the minimum and maximum values of each loading condition measured across the 20-point vane traverse, and the limits of the ensemble RMS pressures have been adjusted to compare pressure unsteadiness on the same scale. These choices for axes limits allow relative comparison between vane positions, individual rotor blades, and the overall mean measurements. For this study, discussion will focus on the 88EO-1CWB crossing. Data characterizing the rotor aerodynamics of the 76EO-1CWB and 38EO-1T crossings are included in Appendix A and Appendix B.

### 3.2.1 Rotor Tip Leakage Flow Inception and Passage Trajectory

In the overall mean ensemble average pressure of the PE 88EO crossing shown in Figure 3.4a, the low-pressure region beginning near the tip of the suction side of the blade identifies the location of inception of the tip leakage jet originating from the pressure side of the blade. The tip leakage jet, driven by pressure gradient, escapes across the rotor tip to the suction side, where it interacts with shear layers in the main rotor passage flow and rolls up forming the tip leakage vortex. In the ensemble averaged overall mean blade-pass period data, this jet of fluid influences the neighboring rotor passage pressure to between 60% and 80% axial chord before exiting the rotor at more uniform conditions. The contour of RMS with respect to the ensemble average of the same condition in Figure 3.4b allows better visualization of the tip leakage vortex and correlates regions of pressure deficit in Figure 3.4a to regions of high unsteadiness in the ensemble average. Qualitative inspection of these contours approximately place the loci of tip leakage flow inception near 13% axial chord and impingement on the pressure side of the neighboring blade near 90% axial chord.

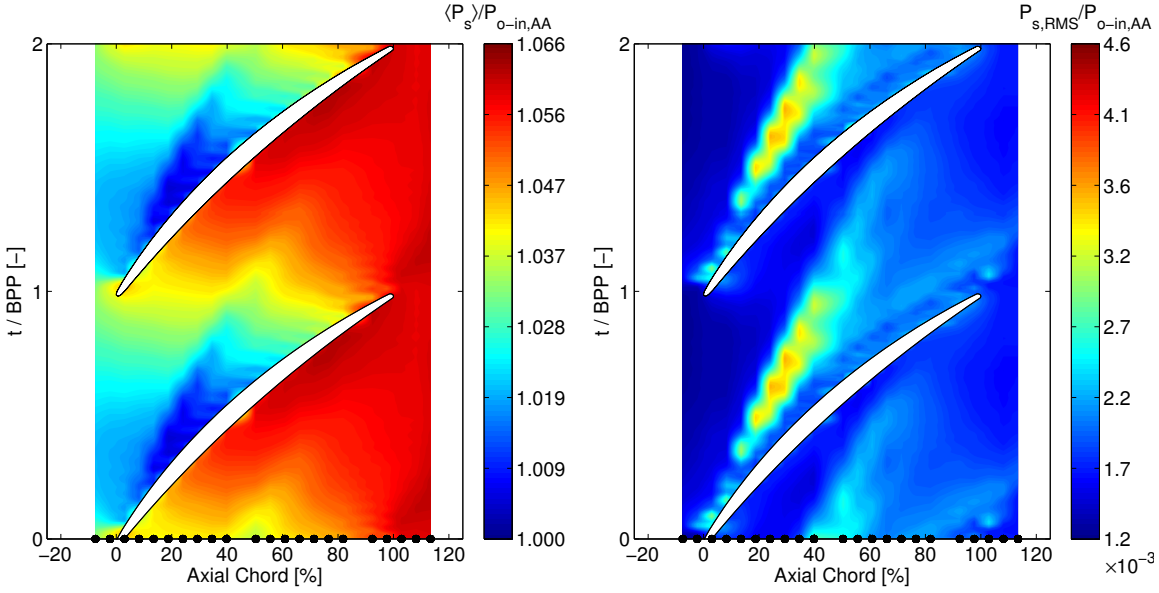


Figure 3.4: Overall mean blade-pass periods of ensemble average static pressure (3.4a) and ensemble average RMS pressure (3.4b) over R2 for PE 88EO crossing.

Increased compressor loading increases the pressure gain through the machine while decreasing the mass flow through the core. The decreased mass flow through the machine

accompanies lower axial velocity entering the embedded rotor and increased incidence. This results in greater flow turning when compared with lower loading and higher mass flow rate conditions. Incidence affects blade loading by influencing the local surface velocity distribution and, therefore, pressure distribution on the blades and loss generation in the boundary layers. As the subsonic flow approaches the rotor blades at increased positive incidence, the increased streamline current around the leading edge causes a higher peak velocity and corresponding lower static pressure. This increases the pressure difference between the pressure and suction surfaces, thereby strengthening the potential for tip leakage flow across the rotor tip. The overall mean ensemble average pressures of the HL 88EO crossing condition in Figure 3.5 show the effects that increased loading and positive incidence on the rotor blades have on the surrounding flow field.

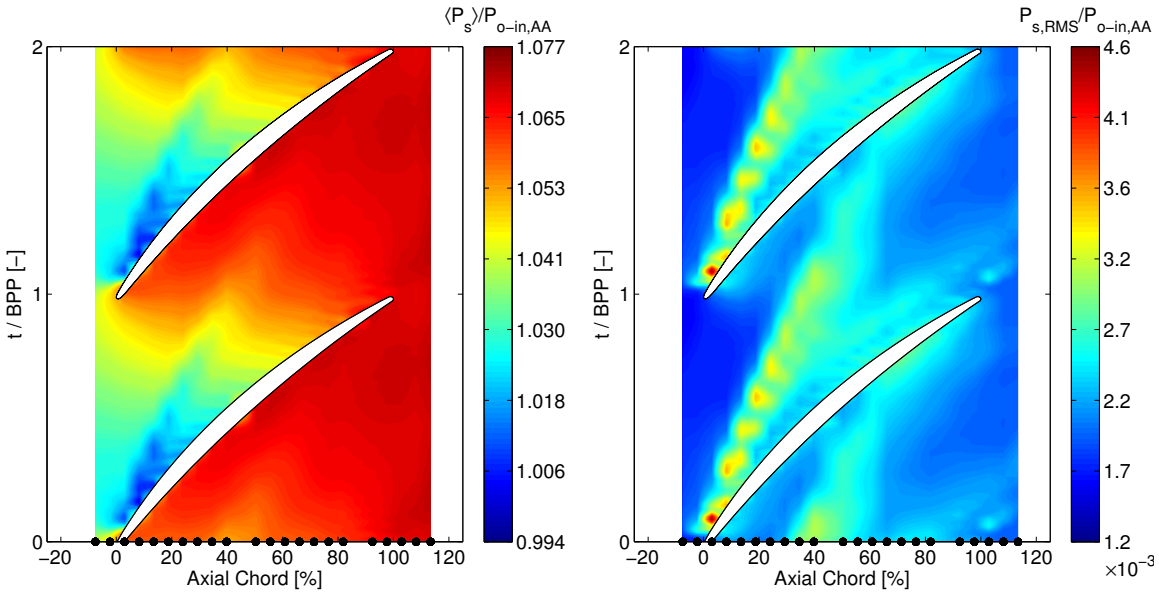


Figure 3.5: Overall mean blade-pass periods of ensemble average static pressure (3.5a) and ensemble average RMS pressure (3.5b) over R2 for HL 88EO crossing.

In the HL case, Figure 3.5a, the static pressure has decreased over the suction side surface's leading edge while the pressure at the exit of the blade-row has increased, with minimum pressure decreasing by about 1.2% and maximum pressure increasing by about 0.4%. These flow field changes show that although the overall velocity of the fluid at the lower flow conditions has decreased, it has locally increased over the leading edge. The local

velocity increase caused by the increased flow incidence angle results in a higher difference in pressure between the pressure and suction sides near the leading edge—higher blade loading—and is shown by the higher levels of ensemble average pressure moved towards the tip.

Comparing the overall mean passage RMS unsteadiness of Figure 3.4b and Figure 3.5b, the overall unsteadiness of the flow in the rotor passage has increased with the decreased flow rate operating condition. The increased flow incidence and the pressure differential between pressure and suction sides of the blade increases the leakage flow trajectory angle by shifting both the points of tip leakage flow inception and neighboring blade impingement toward the leading edge. Relative to the PE condition, the location of leakage flow inception of the HL condition has decreased by about 40% from near 13% axial chord to near 8% axial chord while the impingement location on the neighboring pressure side surface has decreased by about 17% from near 90% axial chord to near 75% axial chord. The trajectories of the leakage flowpaths can be traced by identifying locations of maximum RMS pressure unsteadiness for each sensor position across the axial chord of the blade. Figure 3.6 compares the paths taken by the PE and HL tip leakage flows from their respective inception locations to their near impingement locations. It is challenging to isolate the exact locations of inception and impingement in these data due to the general

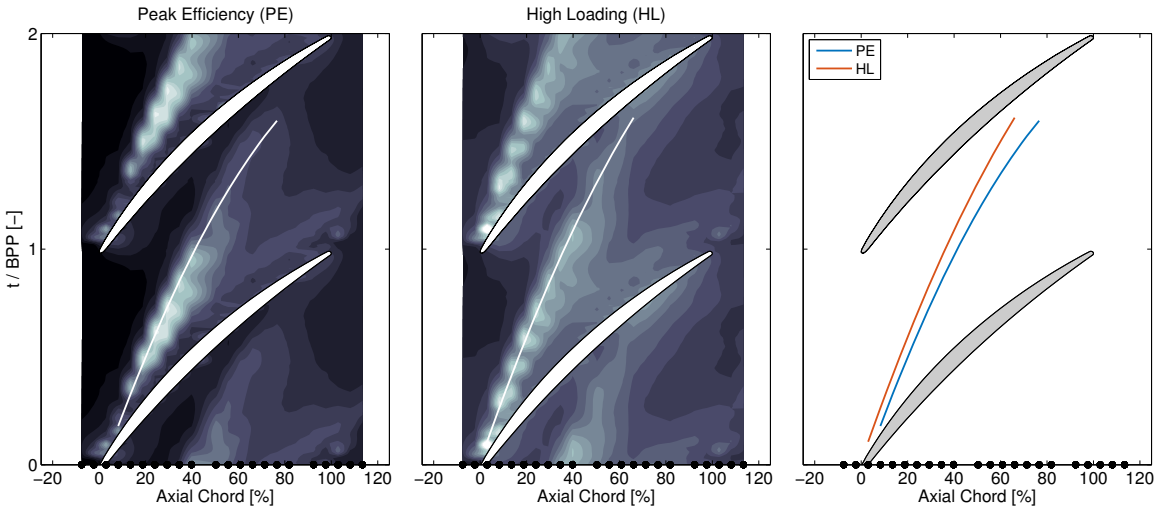


Figure 3.6: Comparison of tip leakage flowpath trajectories at PE (3.6a) and HL (3.6b) 88EO crossing conditions.

higher unsteadiness near the blade surfaces, recognized as blade passing events. Mapping each loading condition's trajectory onto the same coordinate axes, Figure 3.6c, a direct comparison between flowpath trajectories can be made.

Figure 3.6c shows these changes in the leakage flowpath trajectories. At the higher flow rate PE condition the flow travels a shallower path across the rotor passage; as the flow nears the trailing edge, its trajectory turns toward the axial direction. The lower flow rate HL condition exhibits a steeper trajectory when compared with PE with an inception point nearer the leading edge. Differences in path trajectories can be quantified by calculating the angles between the vectors comprising the traced leakage vortex flowpaths and the axial chord. The results shown in Figure 3.7, again, indicate the higher loading, higher incidence case causes a steeper flowpath trajectory closer to the leading edge. Increased loading has increased the angle of the tip leakage flow by about 5.6% at the inception point. Moving aft, the regions of unsteadiness begin to widen or fan out across the passage for both loading conditions. These wider regions of unsteadiness indicate the roll-up of the jet into the tip leakage vortex as it meets shear layers in the passage. General higher levels of unsteadiness near the impingement point and the blade-row exit indicate the dissipation of the high-energy tip leakage vortex and subsequent redistribution of the flow energy to the

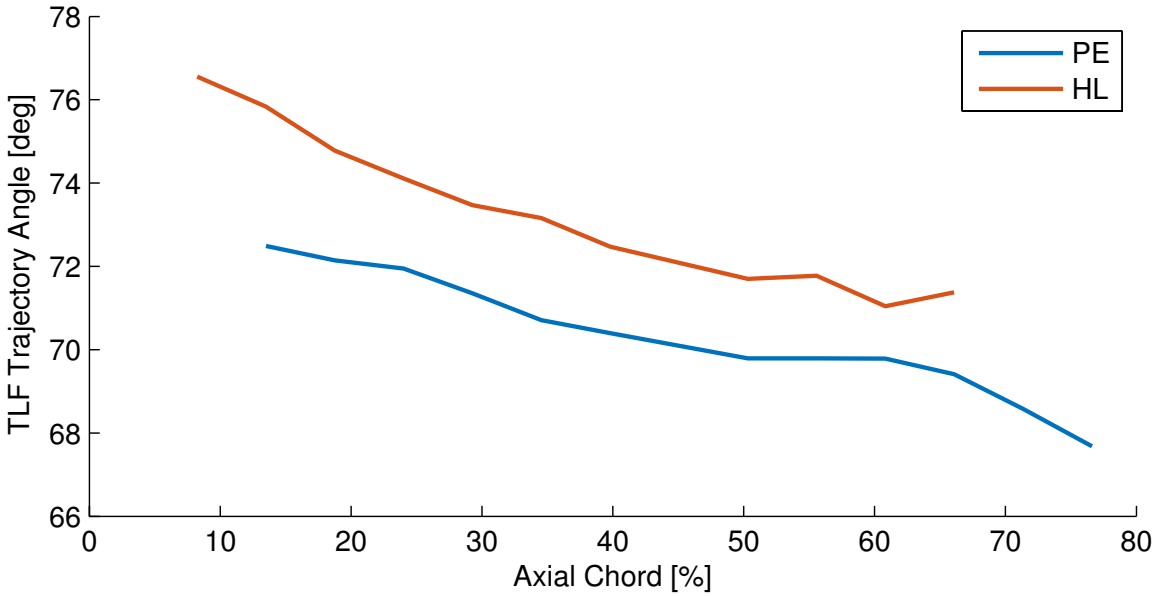


Figure 3.7: Comparison of tip leakage flow angles along the axial chord for PE and HL loading conditions.

surrounding volume, in addition to the potential presence of a double-leakage tip clearance flow phenomenon, described in the next section.

### 3.2.2 Roll-up of the Tip Leakage Jet into the Tip Leakage Vortex

Interaction between the tip leakage jet and shear layers of the main passage flow leads to the roll-up of the jet into a vortical structure. Insight into the formation of these vortices can be gained by studying time-resolved total pressure measurements at the rotor exit plane. A high-frequency pressure transducer embedded in a Kiel head total pressure probe was traversed radially and circumferentially at an axial location just downstream of the embedded Rotor 2 exit. Identical data acquisition settings and analysis techniques as the casing static pressure measurements have been applied to these datasets resulting in a highly resolved flow field at the embedded rotor exit plane. For these data, a 25-point circumferential traverse (0–96% vane passage in 4% increments) of the baseline vane count 88EO crossing and a 20-point circumferential traverse of the reduced vane count 38EO crossing were performed. Data at the rotor exit plane for the reduced vane count 76EO crossing are not available. The different pitchwise resolution results in vane passage

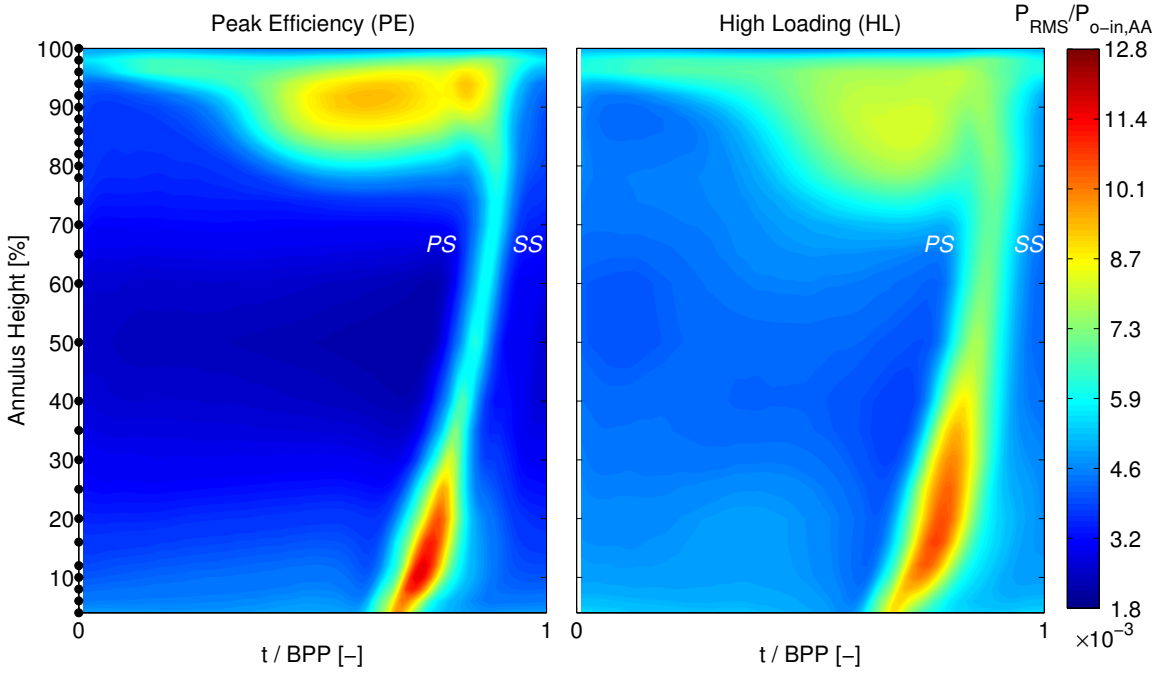


Figure 3.8: Overall mean blade-pass periods of ensemble RMS total pressure at the rotor exit plane for PE (3.8a) and HL (3.8b) conditions of the 88EO-1CWB crossing.

locations of either 1% or 2% difference between the baseline and reduced vane-count configurations, or about 0.030 in. The uncertainty in the vane location measurement is about 25% of this value.

The overall mean vane passage flow field measured at the exit plane of the blade-row for the baseline 88EO-1CWB crossing is shown in Figure 3.8. These contours depict three rotor flow phenomena: the tip leakage vortex, rotor wake, and corner separation near the hub of the blade. The tip leakage vortex is the high RMS pressure unsteadiness in the upper one-third sector of the rotor passage plane while the separation near the hub is characterized by the higher intensities in the bottom one-third of the rotor passage. The rotor wake is the band of higher intensity connecting the hub separation and the tip leakage vortex at about three-quarters of the blade-pass period. The PE case, Figure 3.8a, shows higher local unsteadiness occurring in the tip and hub regions compared to the HL case, Figure 3.8b, but exhibits a thinner rotor wake. Although the PE condition has higher local unsteadiness, the HL condition shows higher RMS unsteadiness occurring throughout the passage, with broader regions associated with the previously introduced rotor flow phenomena.

Comparing the HL condition to the PE condition, the tip leakage vortex has spread radially inward by about 8% while maintaining circumferential width in the passage, the hub separation regions have grown radially into the passage by about 33% and circumferentially by about 25%, and the rotor wake has expanded by about 100%, nearly doubling in width. Higher associated tip leakage vortex unsteadiness occurs with lower relative unsteadiness levels near the hub. The opposite, a presence of greater hub corner separation unsteadiness, corresponds to lower unsteadiness measured in the leakage vortex. The higher unsteadiness tip leakage vortex jet corresponds with more unsteadiness and higher penetration into the neighboring rotor passage, indications of blockage. When higher unsteadiness of the hub corner separation occurs, more blockage exists at the hub. Higher blockage in one region introduces more flow into the other leading to a lower local static pressure and unloading of the region.

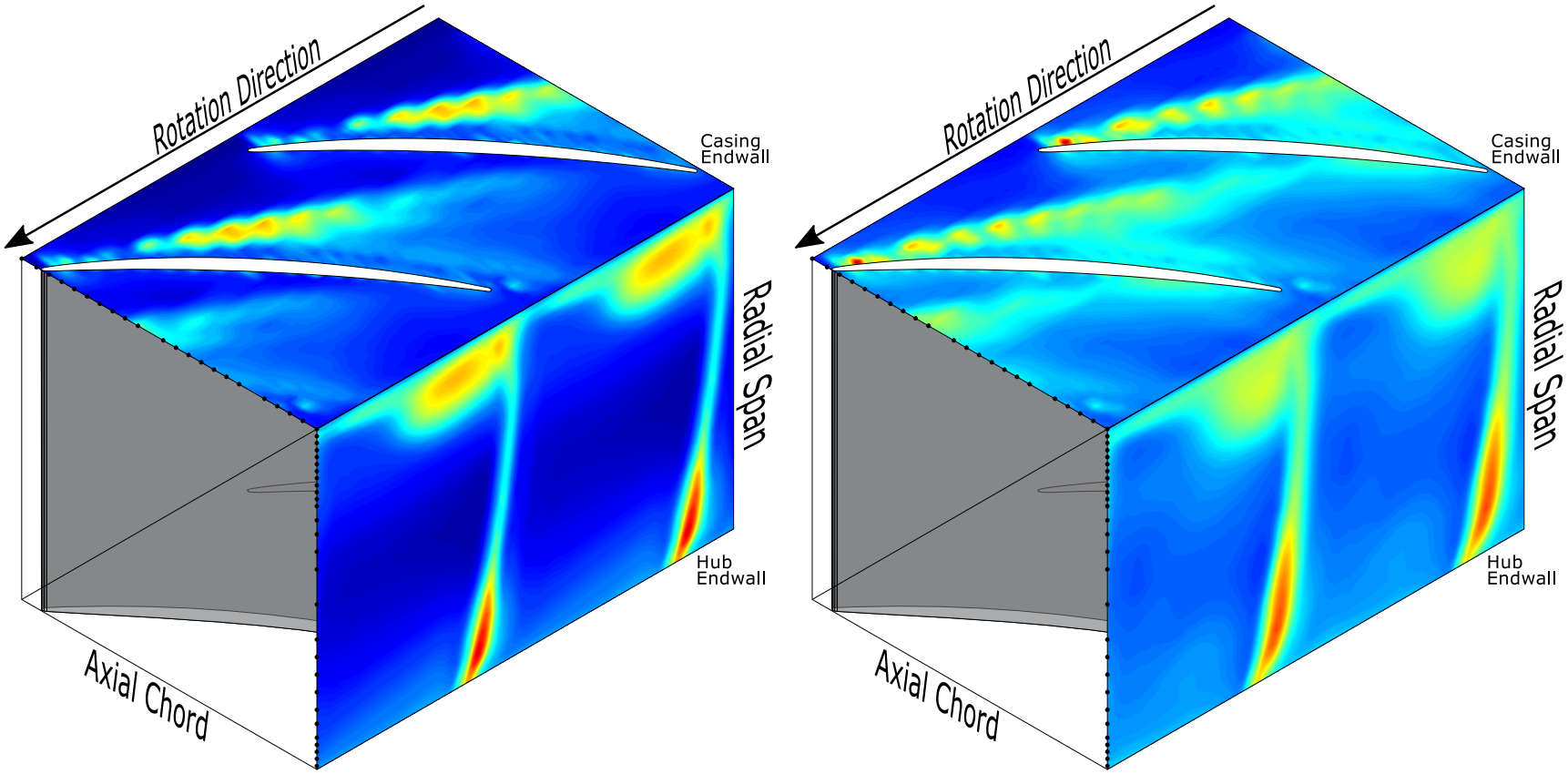


Figure 3.9: Composite mean vane passage RMS pressure contours of the PE (3.9a) and HL (3.9b) 88EO-1CWB crossing.



(b)

The casing static pressure measurements and the total pressure measurements downstream of the rotor exit provide data in orthogonal planes. Combining these data, as in Figure 3.9, provides a composite “three-dimensional” perspective of the flow interactions occurring to be examined. Figure 3.9a contains composite ensemble RMS pressures measured over the rotor and at the exit plane for the PE condition. The shallower trajectory of the tip leakage vortex across the rotor axial chord propagates to the exit plane with a smaller area blockage and higher local unsteadiness when compared to the HL condition in Figure 3.9b. In comparison, the steeper flow trajectory of the HL condition, and its earlier impingement on the blade, serves to dissipate the vortical structure and redistribute the flow energy to the surrounding volume as the energy is mixed out through viscous interaction before being measured at the exit plane. This, in part, explains the general higher RMS pressure unsteadiness and larger blockage area in the tip region of the HL condition when compared to the PE case.

Compressor loading affects the tip leakage flowpath trajectory in three components; a steeper pitchwise trajectory (in plane with the casing measurements towards the neighboring pressure side surface) corresponds with a radial (spanwise) trajectory nearer the casing endwall and a shorter axial trajectory with dissipation beginning to occur before reaching the exit plane. The higher unsteadiness and increased blockage could also be evidence of double-leakage tip clearance flow occurring, described in detail by Khalid (1994), Khalid et al. (1999), and Sirakov and Tan (2003). This phenomenon occurs when tip clearance fluid over a rotor tip is transported across the neighboring rotor passage and passes through the neighboring tip clearance gap. Traveling across the neighboring rotor passage the tip leakage flow incurs significant loss, illustrated in Figure 3.10 adapted from Sirakov and Tan. The evidence for this flow structure exists as a region of high unsteadiness along both pressure and suction surfaces of the blade between 50% axial chord and the trailing edge of the blade. Sirakov and Tan note that double-leakage tip clearance flow structures typically occur at higher loading conditions, but can also be present at design conditions.

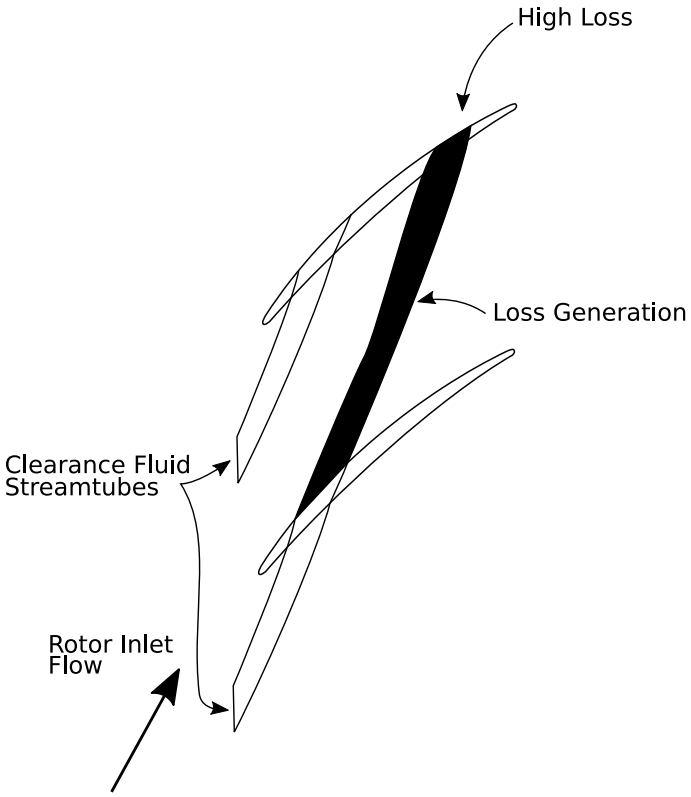


Figure 3.10: Illustration of the double-leakage tip clearance flow structure.

## 3.3 Pitchwise Pressure Measurement Variations from the Overall Mean

The preceding discussion focused on mean traversed stator vane passage measurements and provided a broad depiction and description of the complex flow interactions in a rotor passage. Expanding the investigation to the individual mean vane passage positions comprising the overall mean pitch measurements shows interesting interactions between the upstream stationary vane-row and the embedded rotating blade-row. Figure 3.12 and Figure 3.13 show contours of the mean vane positions of the 20-point circumferential traverse representing the overall PE 88EO mean blade-pass period. Each circumferential mean measurement's position is described relative to the upstream S1 vane passage location used to position the traversed stationary vane-rows. Assuming periodicity, the measurement locations of the radially traversed pressure transducer probe and the casing pressure transducers have almost 17.5 44-vane (IGV, S1, & S2) pitches between them, illustrated in Figure 3.11. Therefore, results from the exit plane should be compared to casing measurements about one-half vane passage out-of-phase.

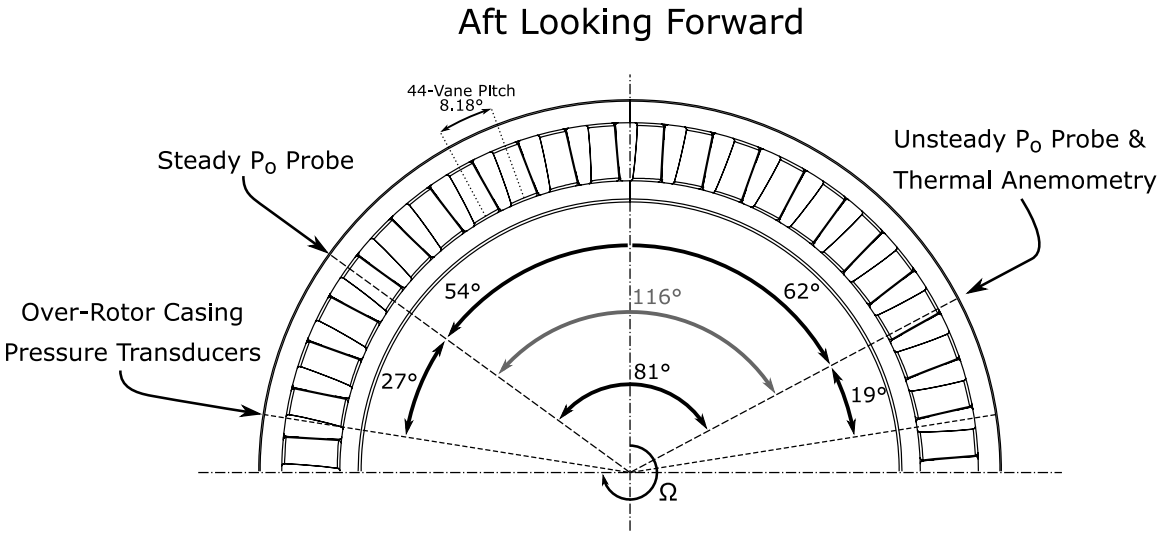


Figure 3.11: Circumferential measurement locations for detailed aerodynamic characterization of the aerodynamic response to forced response excitation for GUIde V.

The mean blade-pass periods of ensemble average pressures in Figure 3.12 and RMS pressures with respect to the ensemble average in Figure 3.13 exhibit circumferential modulation of the measured signal. Computing the mean of the ensemble average contours at each pitchwise location (the mean $\langle P_s \rangle / P_{o-in,AA}$ at each vane position) for all axial sensors in addition to only the rotor exit sensor, at 97.6% axial chord, an approximate trend of the static-to-total pressure ratio as a function of vane position can be characterized, shown in Figure 3.14 for the PE 88EO-1CWB crossing. Comparing the contours of Figure 3.12 and Figure 3.13 with Figure 3.14, the greatest mean ensemble average static-to-total pressure ratios occur between 20–35% vane passage, coinciding with the greatest mean exit pressure ratios occurring at these vane passage locations. These greater pressure ratios occur with an increased strength of the tip leakage vortex near the casing endwall and with greater attenuation of RMS pressure unsteadiness between midchord and rotor exit. The vane passage positions associated with lower pressure ratios, between 55–65% vane passage, exhibit deeper tip leakage flow trajectories across the rotor passage to the neighboring pressure side. It will later be shown an upstream vane wake exists develops and impinges on the embedded rotor between the 15–40% vane passage locations. These locations show a sharp, albeit small, 0.06% increase in the mean ensemble average pressure between 15–20% vane passage. Another noticeable, although even smaller increase

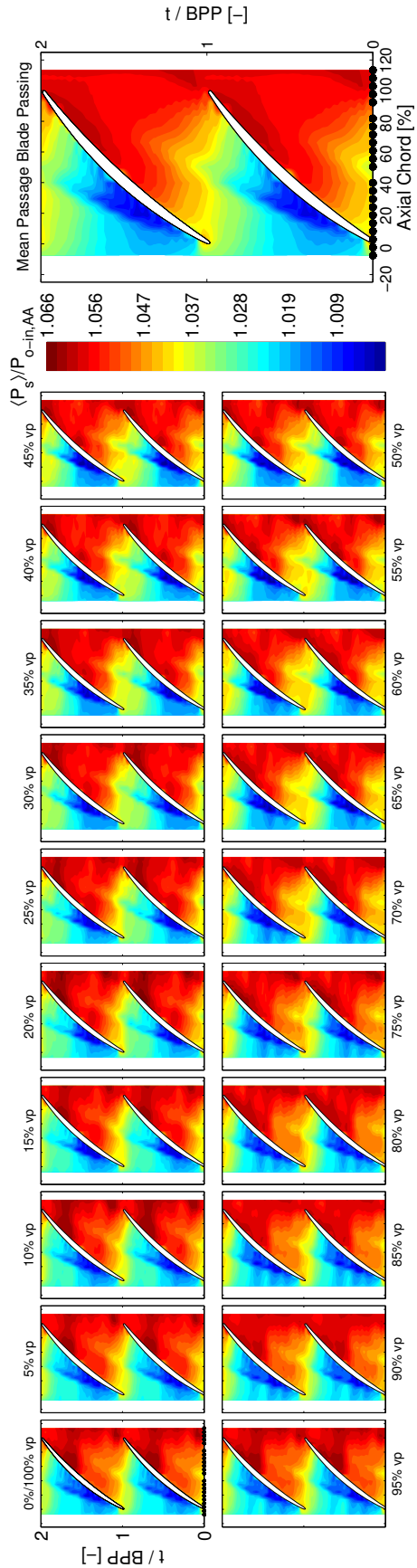


Figure 3.12: Mean blade-pass periods of ensemble average static pressures comprising the PE 88EO-1CWB flow condition.

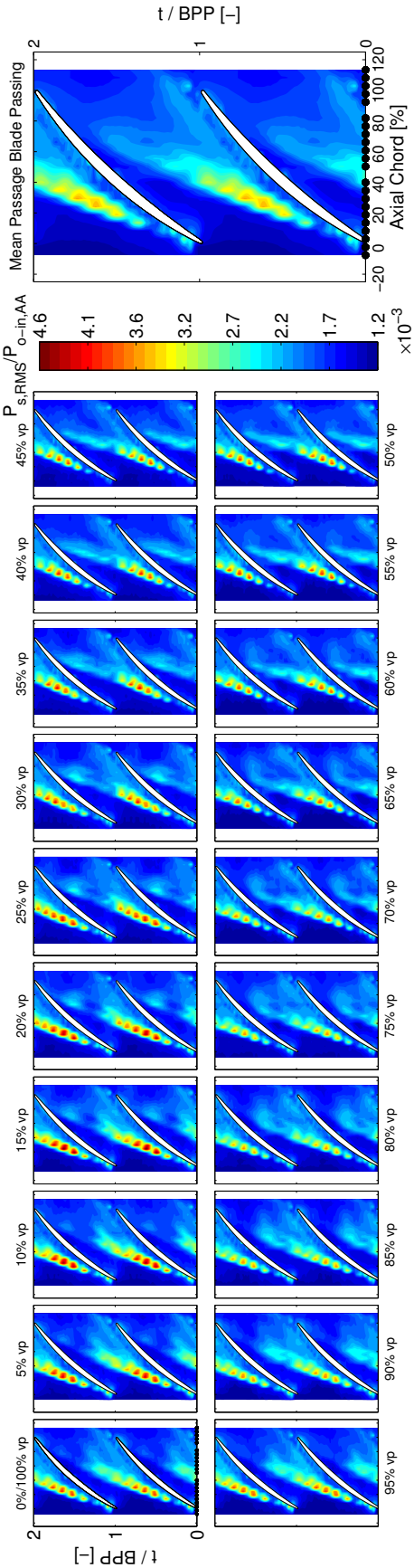


Figure 3.13: Mean blade-pass periods of ensemble RMS static pressures comprising the PE 88EO-1CWB flow condition.

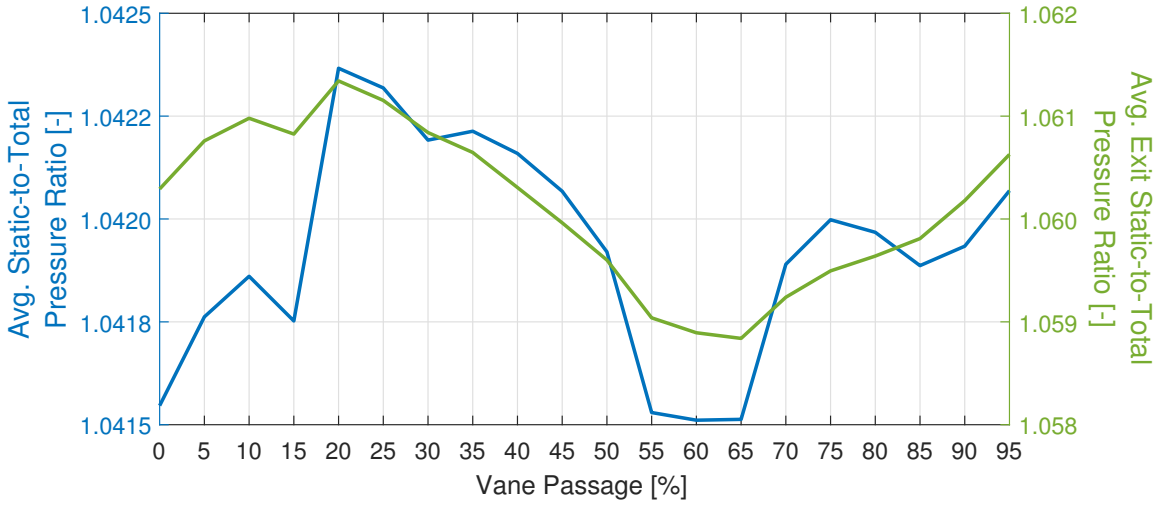


Figure 3.14: Circumferential variation of the mean over-rotor ensemble average pressure ratios for the PE 88EO-1CWB flow condition.

between the 30% and 35% vane passages occurs. These locations will later be shown to exhibit greatest unsteadiness in the passage associated with the upstream vane wake.

Similar trends are shown in the HL loading condition contours of ensemble average pressures, Figure 3.15, and ensemble RMS pressures, Figure 3.16. Comparing these contours with the similarly computed mean values in Figure 3.17, the greatest ensemble average pressures, again, occur in similar circumferential locations between the 10–35% vane passage positions for both the pitchwise and exit averages while the lowest values occur between 60–80% vane passage. Comparing these pitchwise regions with the RMS contours, similar trends to the PE loading case are drawn. The circumferential regions associated with the highest passage pressures coincides with the stronger tip leakage flows near the wall and dissipating near the midchord before impinging on the neighboring blade's pressure surface. The lowest pressures occur with relatively lower strength tip leakage flows and more continuous, less attenuated contour bands throughout the rotor passage. The lower strength tip leakage flows impinge near the trailing edge, whereas the higher strength flows impinge upstream near the three-quarter chord of the rotor blade. This impingement at the trailing edge in part explains the circumferential sine-like shift in the plots of average pressures in Figure 3.17. Between 0–40% vane passage the further

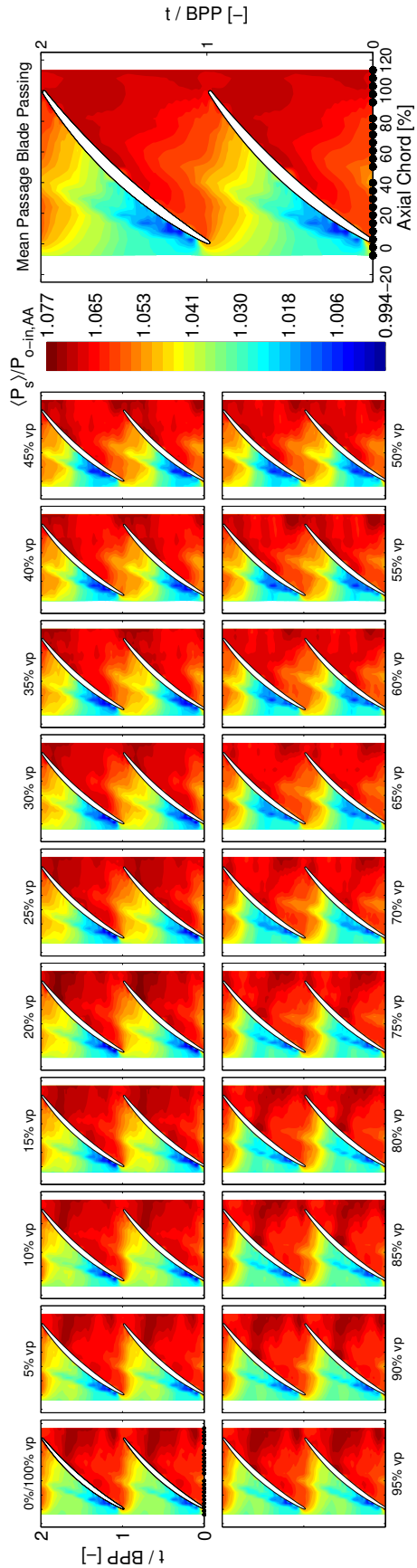


Figure 3.15: Mean blade-pass periods of ensemble average static pressures comprising the HL 88EO-1CWB flow condition.

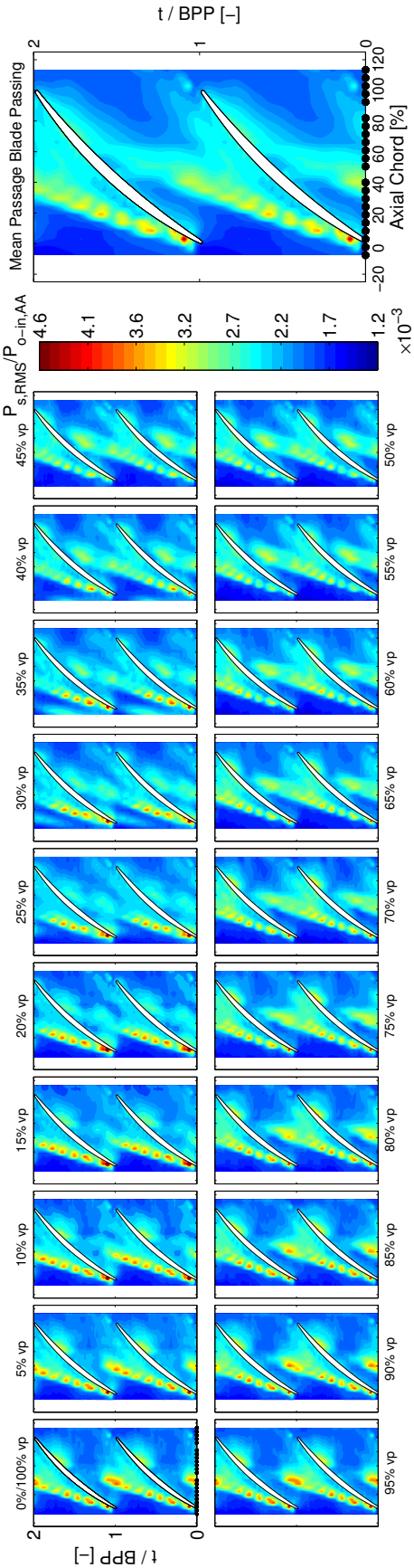


Figure 3.16: Mean blade-pass periods of ensemble RMS static pressures comprising the HL 88EO-1CWB flow condition.

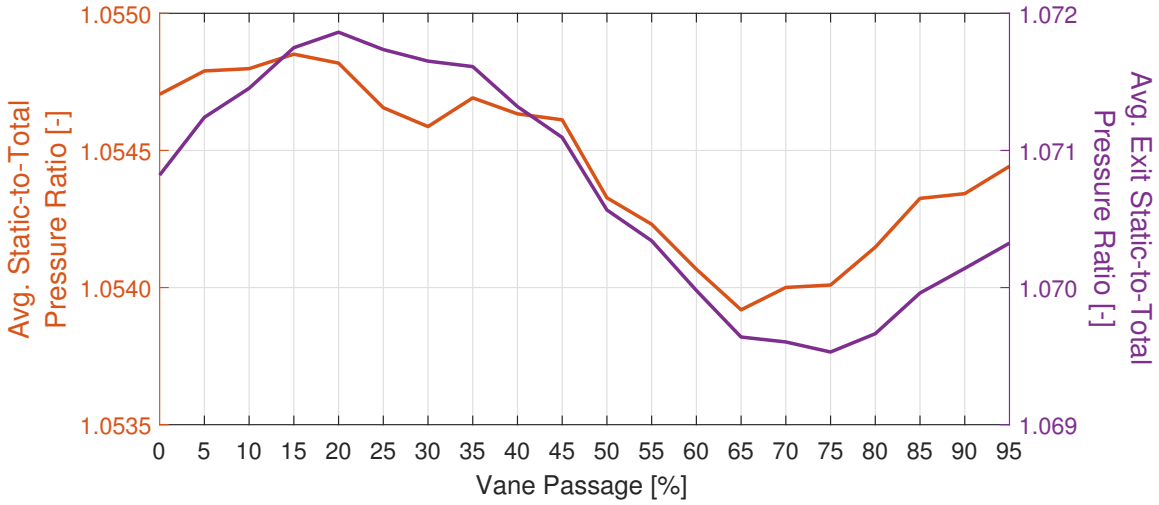


Figure 3.17: Circumferential variation of the mean over-rotor ensemble average pressure ratios for the HL 88EO-1CWB flow condition.

upstream impingement at about 70% axial chord precedes an axially local higher-pressure region just downstream, whereas the impingement near the trailing edge causes a circumferentially local pressure drop. Figure 3.17 shows this trailing edge impingement affects the average exit pressures to a higher degree relative to the pitchwise average, decreasing by just more than twice the pitchwise average. The slight increase in mean pitchwise pressures similarly occurs between 30–35% vane passage locations associated with the upstream vane wake.

Radial traverse at discrete pitchwise locations of the unsteady rotor exit plane flow field provides a similar contour dataset of ensemble average and ensemble RMS pressure measurements at the rotor exit. The PE 88EO-1CWB exit plane contours, ensemble average total pressures in Figure 3.18 and ensemble RMS total pressures in Figure 3.19, are consistent with the previously presented over rotor measurements. A similar technique to Figure 3.14 and Figure 3.17 can be used to show the pitchwise trend of the mean exit plane total pressure ratio (the mean $\langle P_o \rangle / P_{o-in,AA}$ at each vane position) for all spanwise measurements as well as only the 100% span measurement nearest the casing endwall and is shown in Figure 3.20. The radial measurement location nearest the casing endwall exhibits the greatest mean ensemble average pressure ratio near the beginning and middle of the circumferential traverse. Comparing the 100% span, near endwall measurement with

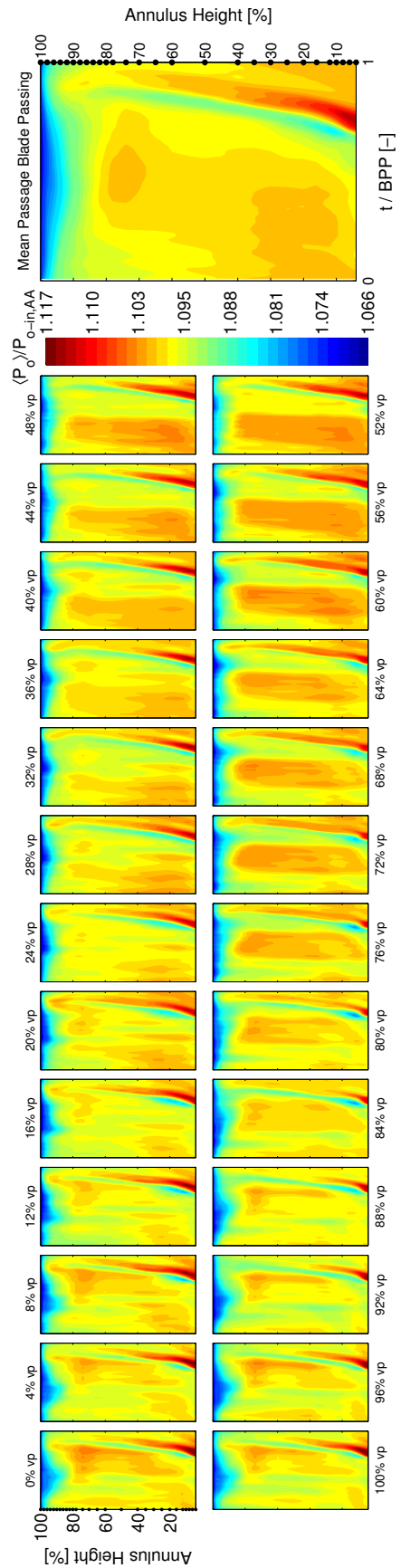


Figure 3.18: Mean blade-pass periods of ensemble average total pressures of the PE 88EO-1CWB rotor exit plane.

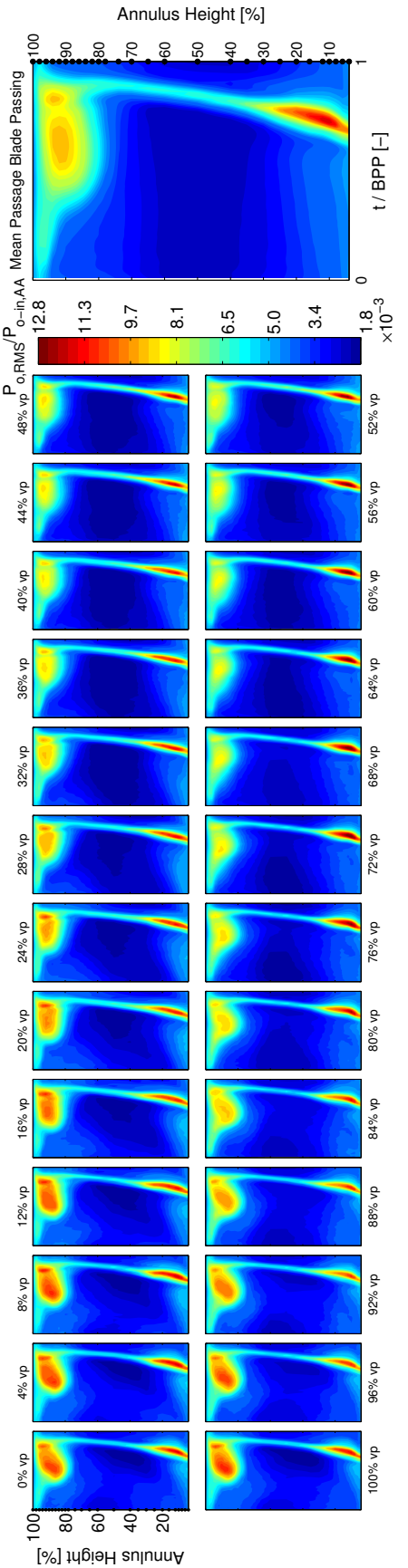


Figure 3.19: Mean blade-pass periods of ensemble RMS total pressures of the PE 88EO-1CWB rotor exit plane.

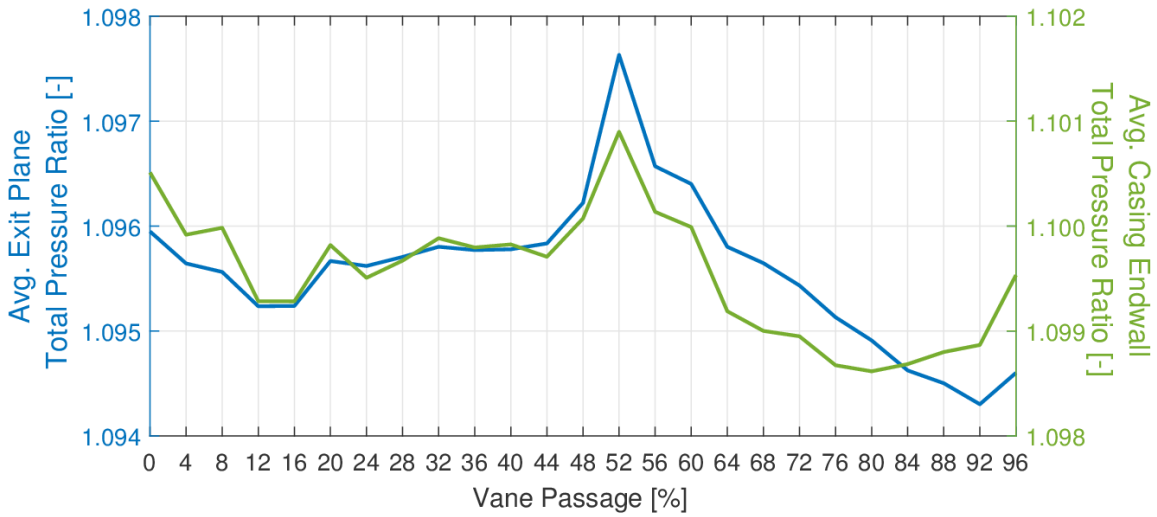


Figure 3.20: Circumferential variation of the mean exit plane ensemble average pressure ratios for the PE 88EO-1CWB flow condition.

the casing static pressure measurements shows agreement between measurement techniques in capturing the respective (total or static) pressure rise at the rotor exit near the casing endwall, with slight pitchwise phase shift due to measurement locations. A sharp pressure increase at the rotor exit, 0.091% or 0.46% depending on the measurement considered, occurs near 50% vane passage and precedes a relatively steep decline over half of the pitch.

Comparing over-rotor and exit plane contours directly, similar trends are also shown between measurements. Highest mean exit plane total pressures occur between 48–60% vane passages. These total pressures correspond with the highest measured exit casing static pressures nearly one-half vane passage out-of-phase (between 10–30% vane passages over the rotor). The 10–30% over-rotor vane passage locations were identified to have a stronger tip leakage flow measured near the endwall. The exit plane measurements agree with this identification, showing higher regions of unsteadiness measured near the casing endwall relative to the other vane passage locations, but lower unsteadiness associated with the vortex roll-up. These locations characterized by lower unsteadiness associated with the vortex roll-up also show greater hub separation pressure unsteadiness. The stronger hub separation has unloaded the tip region flow, decreasing the blockage in the region.

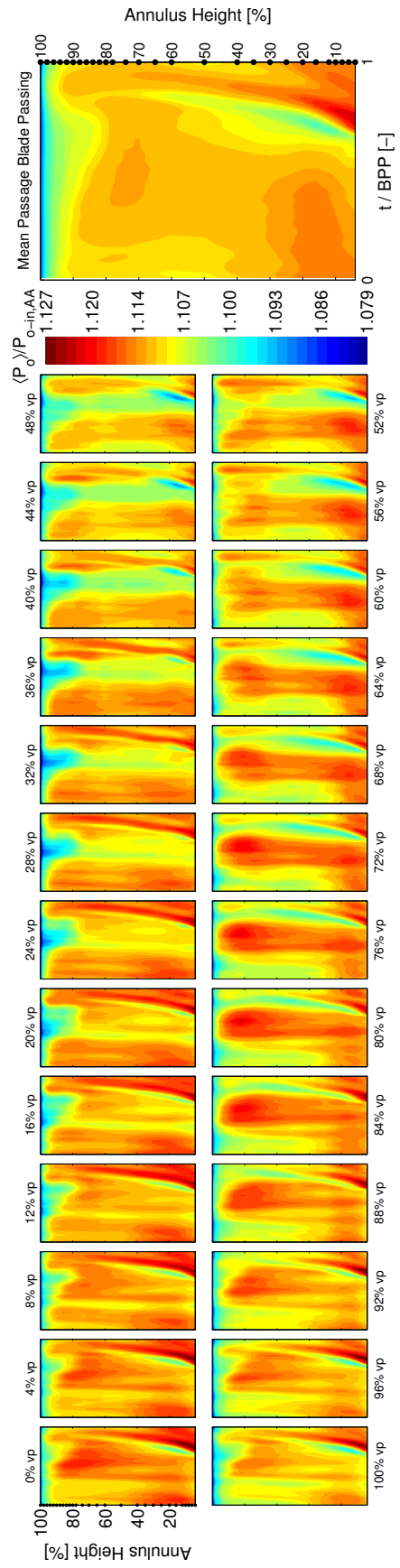


Figure 3.21: Mean blade-pass periods of ensemble average total pressures of the HL 88EO-1CWB rotor exit plane.

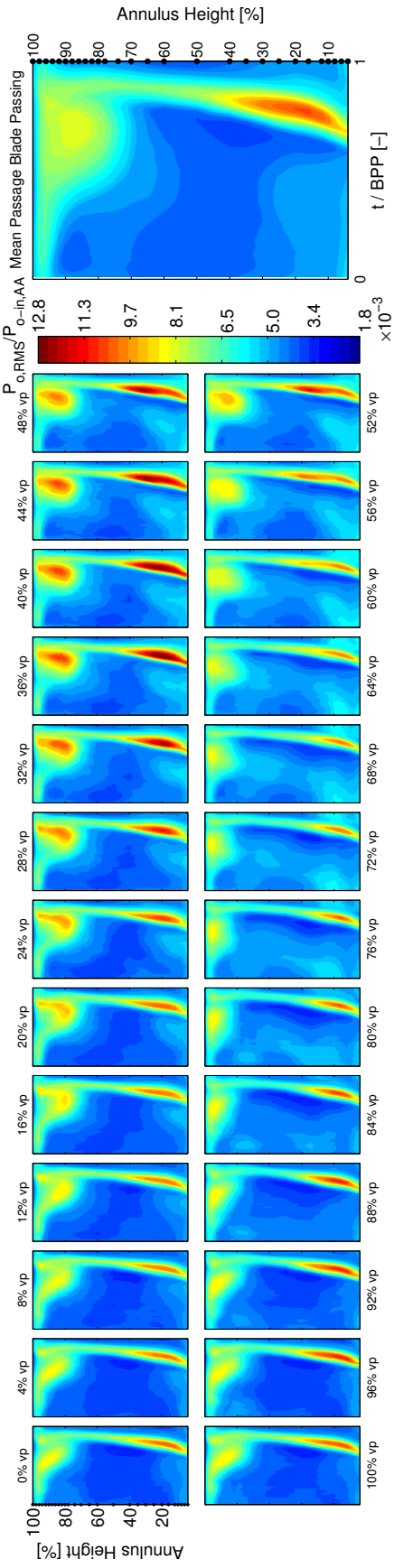


Figure 3.22: Mean blade-pass periods of ensemble RMS total pressures of the HL 88EO-1CWB rotor exit plane.

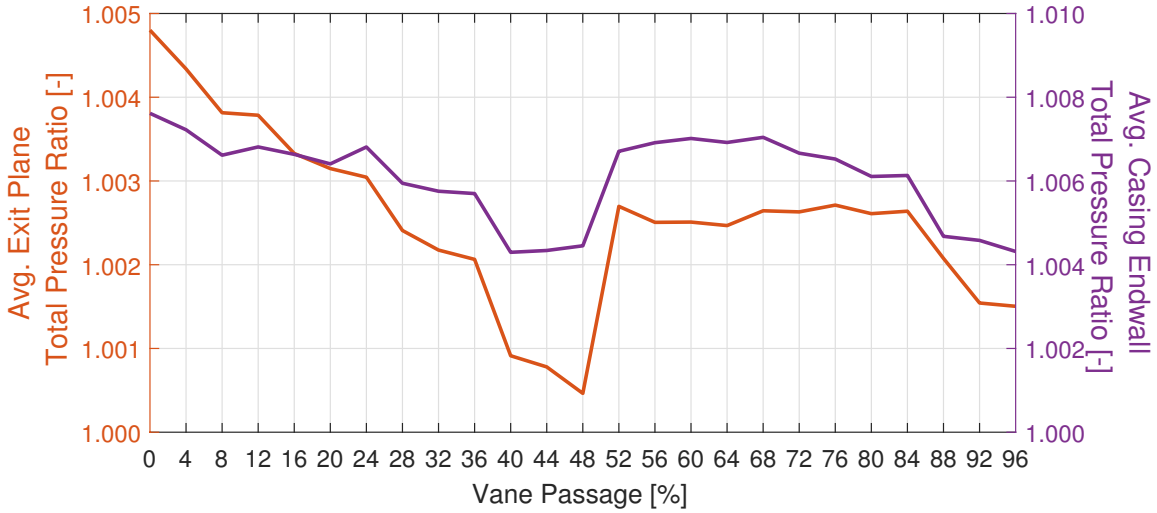


Figure 3.23: Circumferential variation of the mean exit plane ensemble average pressure ratios for the HL 88EO-1CWB flow condition.

Over-rotor vane passage positions between 45–60% exhibited lower local unsteadiness associated with endwall-measured tip leakage vortex but showed deeper penetration to the neighboring pressure side, coinciding with the lowest mean ensemble average pressures measured across the passage. Exit plane measurements nearly one-half pitch out-of-phase, between 0–20% vane passage at the exit, again, display similar characteristics with the greatest unsteadiness associated with the roll-up of the tip leakage vortex measured across the pitch. This stronger vortex roll-up allows the high-energy tip leakage flow to be transported further across the passage. The lowest pressures measured at the exit plane, between 76–92% vane passages are characterized by moderate unsteadiness relative to the other vane passage location measured in the hub and tip regions. Although neither the tip nor hub region display greater unsteadiness relative to other measurements, the moderate unsteadiness levels in both regions increase the overall area of the exit plane affected by the produced blockage. This is expressed in the pitchwise mean ensemble averages with greater total pressure deficits in the tip and hub regions of these vane passage positions.

Similar data and comparisons of the HL conditions in the casing, Figure 3.17, and exit plane measurements, Figure 3.23, also exhibit some similar characteristics. The highest mean static pressure in the casing endwall occurs between 0–20% vane passage, matching the region of higher relative total pressures measured between 52–80% vane passages at

the exit plane. The PE and HL exit plane data share the large relative jump near the 50% vane passage location, but the HL data are distinguished by a decrease in the mean exit plane total pressure before a significant increase and subsequent level pressure measurements for several vane passage locations. The pressure increase near 50% vane passage is once again affected by the higher compressor loading. At PE, the mean pressure ratio between 48–52% vane passage increases by about 0.14%, while at HL this same jump is about 0.24%. The troughs of lower pressures between 40–48% vane passages correspond to locations of highest unsteadiness associated with both the tip leakage vortex and the hub corner separation.

A pitchwise modulation of the ensemble RMS pressure unsteadiness in the hub and tip regions is apparent, and appears to be out-of-phase when comparing loading conditions. Unlike the PE condition, the HL flow phenomena modulate jointly through the pitchwise measurements, shown in Figure 3.21 and Figure 3.22. The RMS pressure unsteadiness associated with both the tip leakage vortex and hub corner separation is greatest between 32–44% vane passage, and corresponds to a mean exit plane total pressure ratio decrease of about 0.17%. Vane passage locations associated with higher unsteadiness in the tip region and lower unsteadiness in the hub region at PE loading tend to show reversed trends at the HL condition. This circumferential modulation mirrors that shown in the casing over-rotor measurements; however, the over-rotor measurements show similar pitchwise trends in the unsteadiness levels of the tip leakage vortex at both loading conditions. Further investigation of the pressure signal spectra reveals the many components of the signal causing the pitchwise modulation.

## 3.4 Spectral Analyses of Unsteady Pressure Signals

Spectral analysis provides insight into the "strength" of the pressure signals at the various engine order frequency bands measured at the sensor axial locations. The amplitude density spectrum—magnitude of the single-sided amplitude spectrum—via the discrete Fourier transform has been chosen to analyze the content of the frequency domain of the collected signals due to its relative speed and computational efficiency compared to other methods for random processes like the segment averaged power spectral density estimation, e.g. Welch's method. The amplitude density spectrum is additionally one simple step, the squared magnitude, from the periodogram power spectral density estimation. A significant disadvantage of this technique is that the variance does not decrease with an increased number of samples, a disadvantage not shared with segment averaged power spectral density estimates. Figure 3.24 introduces the locations of sensors at three axial chord positions chosen to investigate the amplitude density spectra: 13.5% axial chord, 29.3% axial chord, and 55.6% axial chord. These locations have been chosen for their proximity to the tip leakage vortex inception (13.5% axial chord), a common region of high unsteadiness attributed to blade- passing events near the quarter axial chord (29.3% axial chord), and proximity to the impingement of the tip leakage vortex on the neighboring blade's pressure surface near midchord (55.6% axial chord).

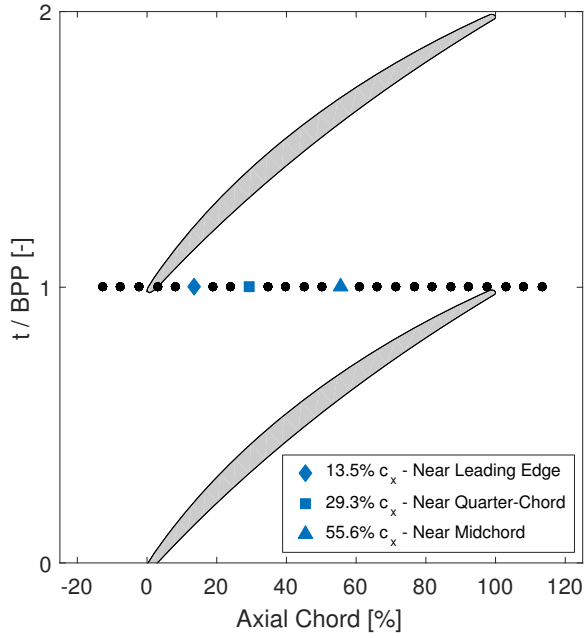


Figure 3.24: Illustration of selected sensor positions.

### 3.4.1 Spectral Analyses of Over-Rotor Static Pressure Measurements

Figure 3.25 represents the replicated overall mean ensemble average spectra of the traversed vane passage pressure time series of the PE 88EO-1CWB crossing. An important result from the spectral analysis of the replicated mean passage ensemble averages is the increase in first few harmonics of the R2 blade-pass frequency engine order with increased machine loading near the leading edge. The axial position near the tip leakage flow inception, Figure 3.25a, shows increases of 52.8% for the fundamental blade-pass frequency, 62% for the second harmonic, under 20% for the third and fourth harmonics, and an increase of almost 105% for the fifth harmonic. Near the quarter-chord, Figure 3.25b, the amplitude density of the fundamental blade-pass frequency is nearly the same for each loading condition, however, the PE case produces a higher amplitude density than the HL condition.

As loading increases, the second harmonic decreases by about 27.8%, the third harmonic increases by about 49.6%, and the higher harmonics decrease with loading but produce similar magnitude. Near the midchord, Figure 3.25c, all harmonics have decreased with increased loading, with the largest relative decrease of 35.9% occurring for the fundamental blade-pass frequency and the lowest relative decrease of 14.8% of the second harmonic. These results support previous results, showing increased loading condition shifts tip clearance flow inception and trajectory towards the leading edge of the rotor blade. For each of these sensors at both loading conditions, the amplitude density decreases from the fundamental blade-pass frequency to the higher harmonics, with the exception of a 7.1% increase between the HL fourth and fifth harmonic near the leading edge and an increase of 2.4% between the PE third and fourth harmonic near quarter-chord.

Figure 3.26 shows the variation of the amplitude density spectra across the axial chord of the blade. The solid lines represent the mean passage amplitudes at each axial location and the translucent regions represent the range of amplitudes measured across all vane positions. The R2 blade-pass frequency, again, shows amplitude shifting to the front of the blade for increased loading. The axial modulation of the 3/rev, the fundamental engine order of the

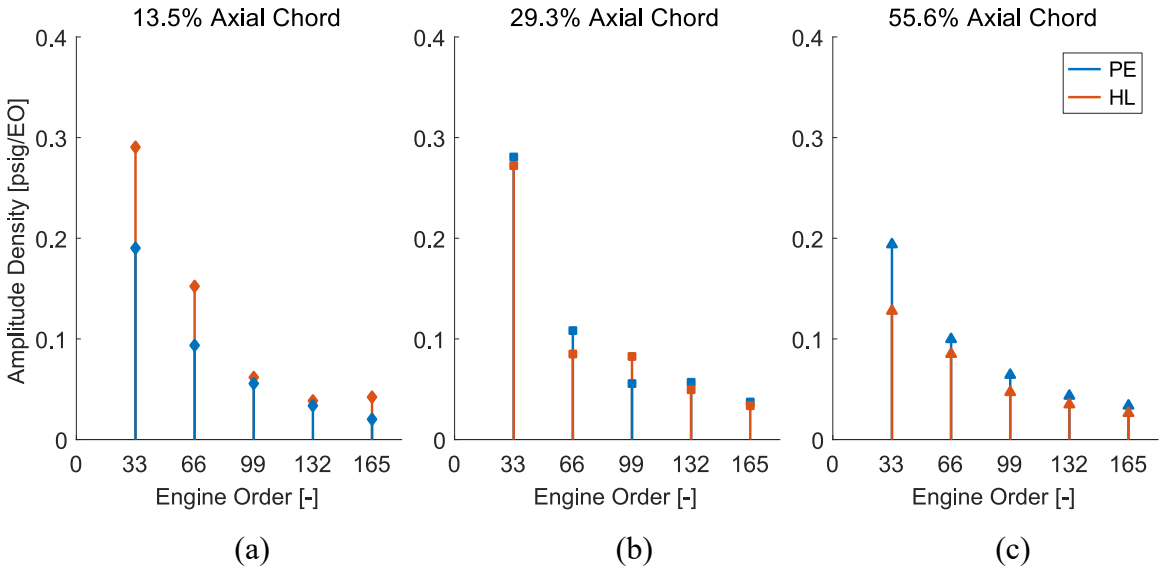


Figure 3.25: Amplitude density spectra of the 88EO-1CWB crossing for harmonics of the R2 blade-pass frequency for a replicated overall mean blade-pass.

differences in rotor blade counts, is shown in Figure 3.26a. The pattern of this modulation shows larger relative regions at the leading edge, trailing edge, and the midchord. The leading and trailing edges have a larger amplitude variation likely because of their proximity to the surrounding rotor blade-rows; the especially large variation and higher magnitude near midchord could be caused by the interaction of amplitude response from both the upstream and downstream rotor blade-rows.

Axial measurements of the first stage rotor blade-pass frequency, Figure 3.26b, show maximum amplitude at the foremost sensor and minimum amplitude near the midchord, after the midchord the amplitude density increases to the sensor furthest aft. These results are, again, a result of sensor proximity to the surrounding rotor rows. Foremost sensors are closer to the first stage rotor while sensors further aft are closer to the stage three rotor. The increased magnitude of the R1 blade-pass frequency at axial locations nearest R2 exit and R3 are produced, aside from the R1 blade-pass frequency itself, by sums of the R2 and R3 blade-pass frequencies with harmonics of the 3/rev from the rotor blade count difference. The R2 blade-pass frequency measurements, Figure 3.26c, have an amplitude density of one order of magnitude greater than the other frequencies of interest. The

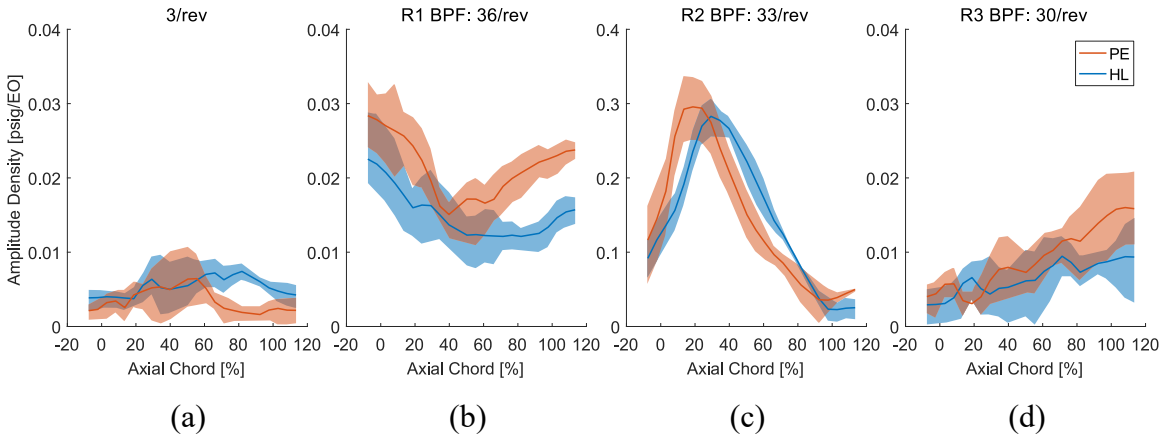


Figure 3.26: Axial variation of amplitude density for 88EO-1CWB crossing.

response of the fundamental R2 mean passage amplitude density grows slightly in magnitude between PE and HL, and the location of maximum amplitude density is shifted forward. Response associated with the R3 blade-pass period, Figure 3.26d, shows the trend in magnitude increasing across the axial chord as the sensor proximity to R3 decreases.

Following the convention introduced in Figure 3.24, Figure 3.27 shows the variation of amplitude density across the different vane passage locations. Sinusoidal patterns as functions of vane passage location are present for many of the spectra and all of the embedded R2 spectra, indicating the effects of surrounding blade-row interactions as the vane-rows are traversed relative to the sensors. Increases in loading intensify the fluctuation of the amplitude density between vane passages and accentuates the sinusoidal patterns. The 3/rev content changes relatively significantly across the pitch. At the beginning of the circumferential vane traverse, calculated at 20% vane passage, the sensors at all positions have spectral magnitudes with a maximum difference of about 34.4% at PE and about 65.1% at HL. Through the mid-passage, calculated at 50% vane passage, this maximum difference grows to 70.2% at PE and 140.8% at HL. Near the end of the traversed pitch, around 80% vane passage, differences become 77.7% at PE and 108.9% HL. These results show increased loading causes these differences between chosen sensors to approximately double at the 0% vane passage and 50% vane passage, while near 80% vane passage, the change between the sensor differences at PE and HL increases by about 40%.

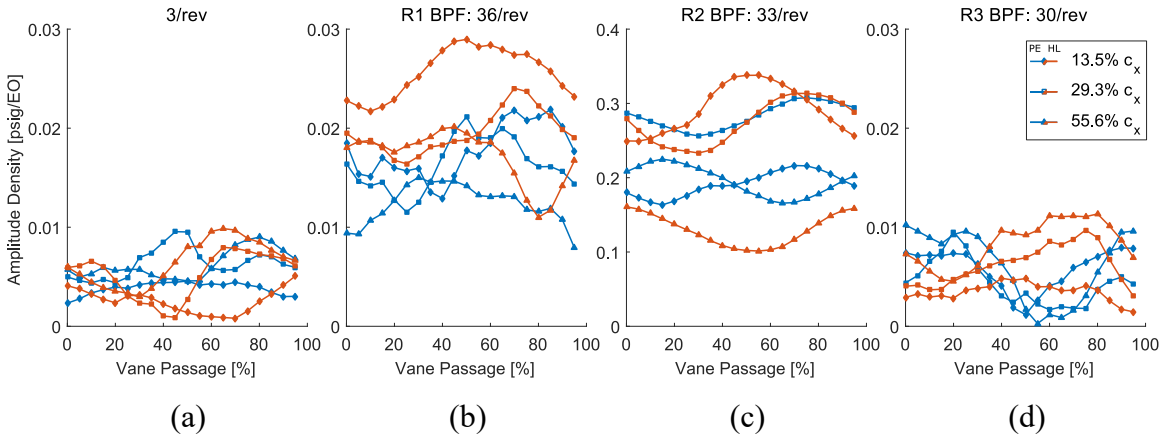


Figure 3.27: Pitchwise variation of amplitude density spectra for 88EO-1CWB crossing.

The R1 blade-pass frequency, Figure 3.27b, shows the highest response occurring in the pitch. Using similar computations for circumferential positions as for the 3/rev, differences of 23.0%, 39.4%, 83.1% and 30.9%, 42.6%, and 58.3% for the selected sensors (axial chord locations 13.5%, 29.3%, and 55.6) at each loading condition, respectively, are calculated. These results show the range in response at the selected axial positions increase near the beginning of the pitch with a change of 34.3%, remain close at the mid-passage with an 8.1% increase, before decreasing near the end of the pitch with a decrease in difference of 29.8% with different loading conditions. The differences between the PE curves are, generally, lower than the differences of the HL condition for the R1 blade-pass frequency.

The embedded stage rotor, located under the sensors and shown in Figure 3.27c, has smoother curves and a scale of an order of magnitude larger compared to the other blade-pass frequencies. The shapes of these curves are out-of-phase when comparing axial locations. This is most apparent when comparing the 13.5% and 55.6% axial chord locations (diamond and triangle markers, respectively) of both loading conditions. At PE, the R2 blade-pass frequency response of these sensors almost exactly cross at 45% and 90% vane passage, while at HL the 50–55% vane passages show a maximum of the 13.5% axial chord sensor and a minimum of the 55.6% axial chord sensor and opposite characteristics at the 0% and 95% vane passage locations. The phase of the sensor located between them, at 29.3% axial chord, is shifted between the curves of the upstream and downstream sensors for the same respective vane passage positions, indicating the circumferential position of

the surrounding vane-rows relative to the sensors causes an opposite frequency response in sensors of a certain axial distance away from one another. As shown in the over-rotor contours, incidence of the incoming flow on the rotor blades changes with pitchwise location and is reflected in the amplitude density spectrum through the vane passage. As the incidence of incoming flow increases, the amplitude on the leading edge sensor mirrors this trend while the sensors further downstream identify smaller relative responses. The effects of incidence and loading condition also become apparent with an exchange in positions of the curves relative to each other between the PE and HL cases. At PE loading, the lowest magnitude response is nearly equally shared by the sensor nearest the leading edge and at the midchord whereas the quarter-chord sensor maintains the greatest magnitude response. When increased to the HL condition, the relative position of these sensor curves shift in opposite ways. Using the mid-passage location (50% vane passage) as reference, the leading edge sensor response has increased by 73.2%, the quarter-chord has remained nearly the same, and the midchord sensor has decreased by 43.8%. Resulting from these shifts, the difference between the minimum and maximum 50% vane passage responses for the corresponding PE and HL loading conditions are 7.4% and 107.1%.

The R3 blade-pass frequency, Figure 3.27d, shares some similarities with the R1 blade-pass frequency, with each having a low magnitude and irregular pitchwise pattern when compared to the R2 blade-pass frequency. However, whereas the leading edge sensor tends to register the greatest response of the R1 blade-pass frequency for most of the passage at both loading conditions, the midchord sensor tends to record greater responses of the R3 blade-pass frequency for much of the passage, with some notable exceptions. Near the beginning of the pitch, the midchord sensor has the greatest magnitude response for both PE and HL conditions but the PE response is greater than the HL response. The changing flow incidence between the loading conditions causes the R3 blade-pass frequency response of the PE case to be greater than the HL case because of the resulting longer axial trajectory and shallower pitchwise trajectory of the PE condition, discussed previously. These trends are reversed near mid-passage, where, at 55% vane passage, the PE measurement of the midchord sensor is the minimum of all curves in Figure 3.27d, while the HL midchord sensor registers the maximum amplitude density. Similar to the changing

flow incidence with loading condition, the change in pitchwise flow incidence causes these comparatively large fluctuations as functions of axial and circumferential location.

### 3.4.2 Spectral Analyses of Rotor Exit Plane Total Pressure Measurements

An identical frequency domain investigation of the exit plane total pressure measurements has been performed by choosing discrete locations along the axis of measurement, in this case the radial span, for a more detailed examination. These locations have been well distributed across the span, and have been chosen to include measurement locations in the region of the tip leakage vortex in the upper one-third of the span, the midspan to examine the effects the rotor wake, and near the hub to investigate effects of hub corner separation.

The amplitude density spectra for the chosen spanwise spectra are shown in Figure 3.28. Since these spectra have been measured in the axial gap between R2 and S2, frequencies other than the R2 blade-pass frequency are present when compared with the measurements taken directly over the rotor, particularly the fundamental blade-pass frequencies of R1, R3, and 3/rev content. Amplitude density in the tip region, 90% span, shows greater fundamental R2 blade-pass frequency content when compared to its harmonics. The PE condition has a stronger spectral magnitude than the HL condition for the fundamental blade-pass frequency. The shallower tip leakage flow trajectory at the PE condition facilitates the tip leakage flow transport further aft; since the sensor is located at the exit plane, the shallower trajectory causes a greater amplitude at the exit plane. The second and third harmonics have similar amplitudes, but they have opposite effects caused by loading. The HL condition shows the spectral magnitudes decreasing steadily from the fundamental blade-pass frequency to its fifth harmonic. In contrast, the PE condition shows an initial decrease between the fundamental and second harmonic and an increase between the second and third harmonics before a similar steady decrease to the fifth harmonic.

The 80% span spectrum follows similar trends as that at 90% span. The PE amplitude is still stronger at the fundamental blade-pass frequency, and the HL is stronger at the second harmonic. The third, fourth, and fifth harmonics have similar amplitudes, but between

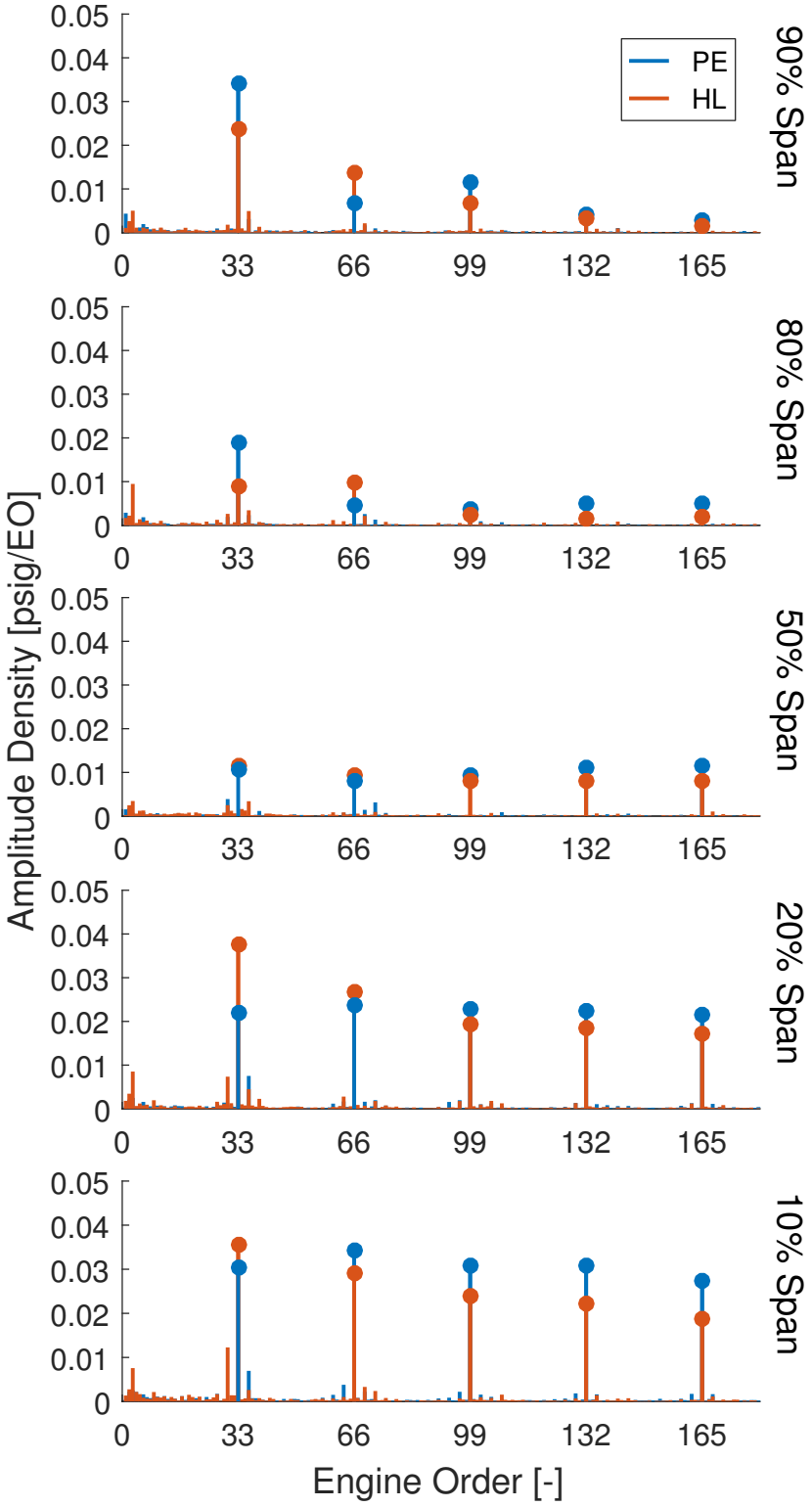


Figure 3.28: Amplitude density spectra of the 88EO-1CWB crossing for harmonics of the R2 blade-pass frequency for a replicated overall mean blade-pass.

them, a small increase in amplitude response occurs. The HL condition shows a notable amplitude peak at the 3/rev, nearly equal to the fundamental and second harmonic of the blade-pass frequency. At the 50% span, energy is nearly equally spread across the frequencies with similar amplitudes for both loading conditions.

As the sensor approaches the hub, 20% span, higher amplitudes for each spectrum are registered. The fundamental R2 blade-pass frequency amplitude is similar its harmonics, with the second harmonic having the greatest amplitude. Increased loading increases the fundamental response by 71.1%, but the harmonics have similar amplitudes to the PE case. Larger spectral magnitudes for R1 and R3 blade-pass frequencies occur in both loading conditions with similar amplitudes, and the 3/rev magnitude increases nearly 240% between PE and HL. At 10% span, similar trends to the 20% span location are apparent. The fundamental R2 blade-pass frequency has similar amplitude between loading conditions, with a smaller increase between PE and HL when compared with the 20% fundamental R2 frequencies. The PE amplitude remains fairly constant across the R2 frequency harmonics while the HL amplitude slowly drops off towards the higher harmonics. The overall decrease between the fundamental and fifth harmonic of the HL condition is 46.6%.

Generally higher amplitudes across the spectra exist at this location, nearest the hub, when compared with the other chosen spanwise positions. Since, of these positions, these measurements are taken nearest the hub, flow energy from the rotor drum (e.g., unsteady flow velocity and lift from the spinning cylinder, stator hub leakage and cavity flows) could be causing the flatter, greater amplitude density response across the spectra. The downstream R3 blade-pass frequency is greater here than at the 20% span location for the HL condition, with an increase of 66.8% between the measurement locations. However, the PE condition shows the R3 blade-pass frequency to be less significant, only 19.4% of the HL amplitude at 10% span and a decrease of 61.2% from the PE amplitude at 20% span. A similar situation occurs with the 3/rev, with insignificant response at PE and a value 21.4% that of the fundamental R2 blade-pass frequency at the same loading condition.

Variation in the spanwise spectra measurements, Figure 3.29, shows greater variation across the circumferential traverse, indicated by the larger translucent areas surrounding the line representing the mean value, when compared with the similar axial variation of Figure 3.26. The maximum difference of the R2 blade-pass frequency spectra at the exit plane is about 188% while the over-rotor measurements have a difference of only 30.2%. The four engine orders of interest in Figure 3.29 show a general similarity of midspan shape of the mean spectra lines for both loading conditions, with differences occurring in the hub and tip regions for all but the R3 blade-pass frequency. The effects of loading are shown to push the higher amplitudes to near 20% span for each of the engine orders of interest when loading from PE to HL. Similar spanwise locations of greater spectral magnitude occur in the tip region, at about 90% span. The 3/rev, Figure 3.29a, shows similar amplitude density response across the span for both loading conditions, with a nearly 60% greater mean occurring through midspan for the HL condition. The PE R1 blade-pass frequency has the greatest amplitude occurring nearest the hub with an immediate 26.2% drop between the near hub and 20% span locations. The HL condition has an opposite trend, starting at a relatively lower amplitude and increasing by about 13.1% between the near hub and 10% span locations. After the amplitude decrease in the PE spectrum, the magnitude increases and similar shapes occur through the rest of the span for both loading conditions.

The R2 blade-pass frequency has nearly similar amplitude response near the hub, the HL condition shows an increase in amplitude through 20% span, and a difference of about 60% occurs through the midspan. Towards the tip region, both loading conditions have increased response between 60–80% span. After 80% both values decrease, but a sharp 239.1% increase in the PE mean spectrum line occurs between 84–96% span followed by a similarly sharp 50.9% decrease between 96–100% span. Comparing the mean blade-pass RMS pressure contours of Figure 3.8 with the R2 blade-pass frequency content of Figure 3.29c, the areas of greatest amplitude response occur at the spanwise locations of the greatest RMS pressure unsteadiness. The PE tip leakage vortex measured at the exit plane occurs near 96% span, and the sharp peak is caused by the more localized unsteadiness of the loading condition when compared to the less localized unsteadiness of the HL condition

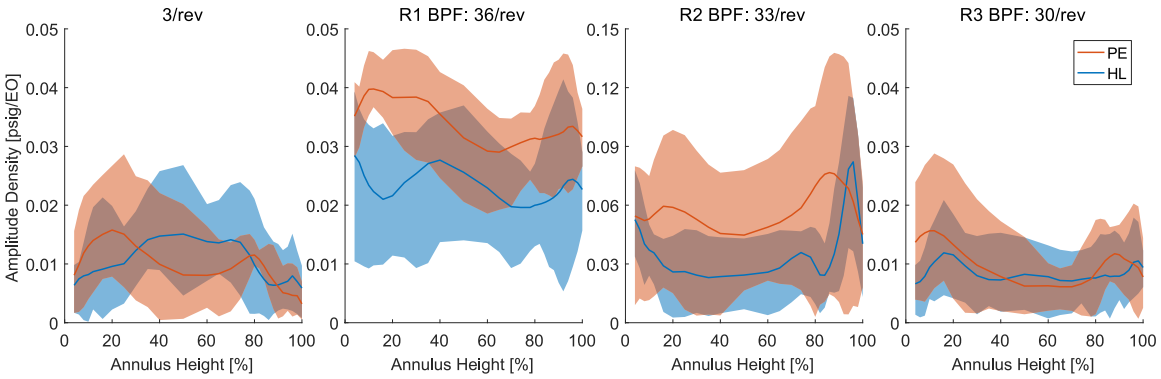


Figure 3.29: Spanwise variation of amplitude density for the 88EO-1CWB crossing.

occurring near 86% span. The hub flow separation of the PE case is similarly contained with greater unsteadiness near the hub compared to HL, causing the higher amplitude near the hub in Figure 3.29c. The bump in amplitude density at the PE 74% span location coincides with a location of the RMS pressure unsteadiness contour where the rotor wake begins to connect with the tip leakage vortex of Figure 3.8a, and a near minimum exists in the R1 blade-pass frequency from Figure 3.29b. The R3 blade-pass influence follows similar trends, fairly constant in the midspan with increases in the hub and tip regions. The relatively larger increase in the hub region could be affected by the downstream stator hub leakage flow across the knife-seal under the S2 hub shroud.

The pitchwise location across the vane passage has a significant effect on the amplitude density spectra. Figure 3.30 shows the pitchwise variation of amplitude density at three different span locations: near the rotor tip (80% span, top row), at midspan (50% span, middle row), and near the rotor hub (20% span, bottom row). Near the beginning of the circumferential traverse (8–20% vane passage), the variation of 3/rev blade-count difference in Figure 3.30a shows an opposite trend occurring when comparing the 80% span with both the 20% and 50% spans of the PE condition. Over this region, the PE spectral amplitude increases by 53%, whereas for the midspan and 20% span locations a decrease of 7.3% and 17.4% occurs, respectively. Similar amplitude density increase occurs for all three span locations between the midspan and about 60% span, followed by increased response increases between 60–100%. The location of maximum amplitude

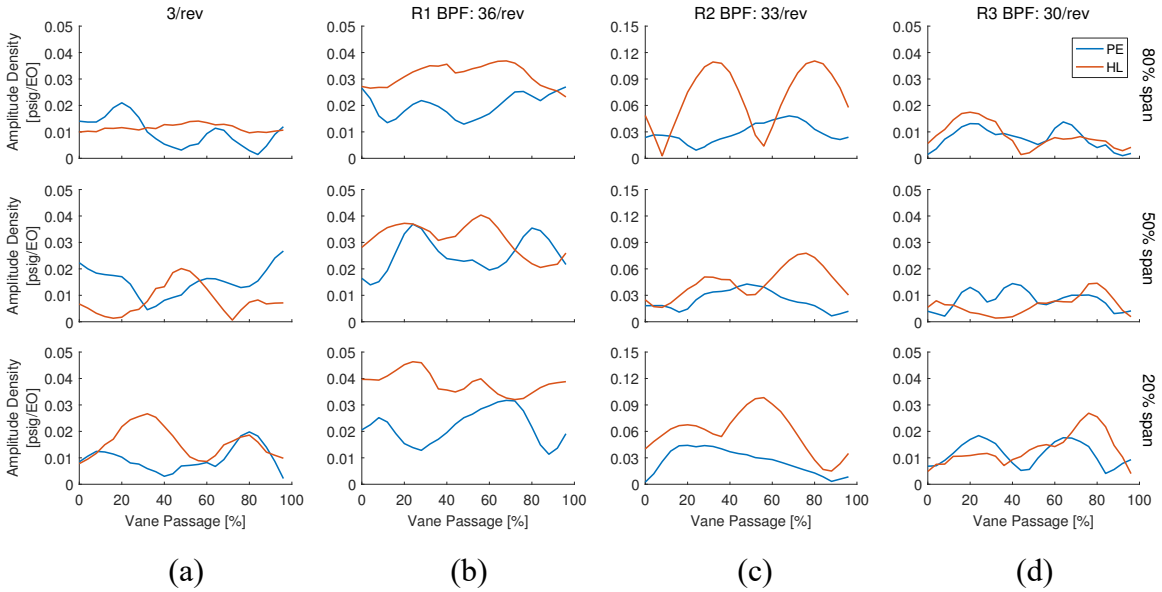


Figure 3.30: Pitchwise variation of amplitude density spectra for 88EO-1CWB crossing across rotor exit plane span.

density in this region near the hub is the location of minimum amplitude density in the 50%

and 80% span locations in the same pitchwise region. The HL condition shows the 80% span 3/rev amplitude remaining nearly constant across the traverse, while the 20% and 50% span locations show sinusoidal oscillation. Between 0–50% vane passage, relatively large rises and subsequent falls in amplitude occur, these regions coincide with similar variations in the PE amplitude.

From the trends in Figure 3.30a, the amplitude density response seems to shift around the circumference with spanwise location. Similar spectral structures exist in the spanwise data, but they are shifted to lower vane passage locations (as indicated by the abscissa) as the sensor approaches the hub. This shift is apparent in the fundamental rotor blade-pass frequencies as well. The R1 and R3 blade-pass frequencies, Figure 3.30b and Figure 3.30d, at each spanwise positions show similar, double amplitude peaks in the passage, shifted with decreased span. The PE condition R3 blade-pass frequency at midspan, however, shows a successive double peak occurring between 0–50% vane passage. The pitchwise neighboring region where the second peak might be expected to occur, between 60–80% vane passage, is relatively flat when compared to the other spanwise regions.

The variation of the R2 blade-pass frequency with pitchwise position, Figure 3.30c, shows two peaks in the measurements near the rotor tip, occurring near 8% and 68% vane passage for PE loading and 32% and 80% vane passage for the HL condition. The PE loading 20% and 50% span waveforms, show single peaks occurring near 20% and 50% vane passage, respectively, however had the circumferential traverse covered the neighboring 10–20% vane passage a similar two-peak response would appear to have occurred for the 50% span location. The single peak in the R2 waveform at 20% span for PE loading coincides with a peak in the R3 blade-pass frequency at the same location, spanwise and pitchwise, and loading. This, coupled with a steady decline across most of the pitch and its location to the hub, could indicate greater effects of stator hub leakage flow occurring in the circumferential region. Comparing the RMS pressure contours of the pitchwise region around 20% vane passage in Figure 3.19, these circumferential regions show lowest unsteadiness associated with hub corner separation and highest unsteadiness in the tip region within the passage. The HL condition 20% and 50% spans contains the characteristic two peaks shifted slightly circumferentially from each other.

## 3.5 Effects of Changing Upstream Vane Count and Rotational Speed

The majority of flow phenomena and trends discussed to this point remain the same with increased machine speeds and the change in S1 to a reduced vane count. Ensemble average pressures and the ensemble RMS pressure unsteadiness in the signals increase with compressor speed, and data from the 76EO-1CWB and 38EO-1T crossings are shown in appendices. Spectral analyses show nearly identical spectra for the reduced vane count compared to the baseline vane count. One particular difference in the baseline dataset compared to the reduced vane count datasets is the previously characterized flow phenomena appear to be shifted by about one-half vane passage. Using the over-rotor measured tip leakage flow as an indicator, the PE and HL 88EO-1CWB, PE 76EO-1CWB, and PE 38EO-1T crossings show strongest tip leakage flow unsteadiness between about 0–20% vane passage. In contrast, the HL conditions of the reduced vane count configuration, 76EO-1CWB and 38EO-1T, have greatest tip leakage flow unsteadiness between about 55–75% vane passage. This apparent shift in the development of the tip and hub leakage flows and rotor wakes seems to be caused by the reduced upstream vane count.

## 3.6 Blade-to-Blade Variation in Unsteady Pressure Measurements

It is important to consider the aerodynamic variation between individual rotor blades of an ensemble average revolution. These blade-to-blade differences, from blade-row interactions, manufacturing differences, or wear, can have a large impact on the rotor flow structures, including the tip clearance vortex. The most important geometric dimension in tip clearance flows is the tip clearance gap itself. As part of a previous comprehensive tip clearance study performed on the same machine (Berdanier, 2015), the static cold runout of the rotor blade tips with respect to Blade 1 was measured at three different circumferential locations. This study identified blade-to-blade tip clearance variation of Rotor 2 to be approximately to $5\times10^{-3}$ in. with an uncertainty on the order of $1\times10^{-4}$ in. Pertinent tip clearance measurements relative to Blade 1 and absolute tip clearances from this previous study are shown in Figure 3.31. These measurements indicate the largest clearance occurs for Blade 7 and the smallest clearance occurs for Blade 26. A smooth sinusoidal curve connects the two extrema, resulting in regions of the rotor having larger

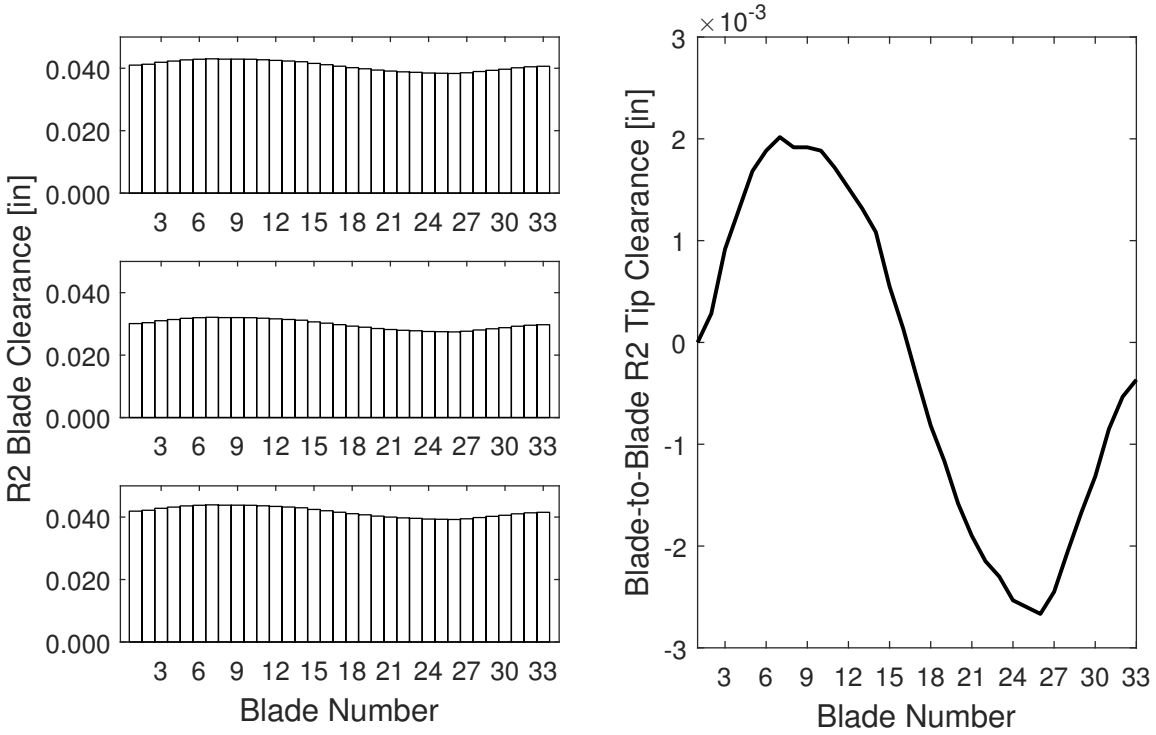


(a) (b)

Figure 3.31: Rotor 2 blade clearances measured at three circumferential locations (3.31a) and runout with Blade 1 as reference (3.31b).

tip clearances relative to each other (i.e., the region with the largest tip clearances occurs between Blade 4 and Blade 14). To investigate these blade-to-blade differences and their effect on the flow fields, the ensemble average revolution method introduced in Figure 3.2 will be used. Although averaging is still occurring, the pressure traces associated with each blade are averaged over many revolutions at each span position, rather than averaging many revolutions to get a single mean blade-pass pressure trace at each span position.

The mean passage ensemble average revolution of the HL 88EO-1CWB crossing, Figure 3.32, shows the effect of this region of greater tip gap between the rotor and casing endwall. A distinct increase in RMS static pressure unsteadiness is present in the rotor passages of Blades 7–10. The local increased unsteadiness measured over these rotor blades is the result from the mean pitch revolution; therefore, this increased unsteadiness is also an evident feature in each pitchwise location mean measurement. This phenomenon is also present, to a lesser extent, in the PE loading condition for the same blade region. In contrast to the region of greater tip clearance, the lower tip clearance region between Blades 23–28 shows lower unsteadiness measured near the casing endwall.

Interesting flow features, previously averaged without considering individual rotor blades, become apparent in the ensemble average revolution. At certain pitchwise locations, evidence of an upstream vane wake appears. This flow structure is identified as a vane wake because it is present upstream of all R2 blades. For the baseline vane count S1 configuration, the wake is present between the 30–40% vane passage locations, whereas for the reduced vane count S1, the wake is present between 70–80% vane passage locations. Figure 3.33 shows Blades 7–10 of the 30–40% vane passages and the presence of the upstream wake. Figure 3.34 shows Blades 7–10 through a full vane passage of measurements including the development, impingement, and propagation of a wake through the rotor passage for the 88EO-1CWB HL flow condition. The appearance of the upstream wake coincides with a reduction in the tip leakage vortex penetration across the rotor passage. Previously this reduction in passage penetration was linked to weaker roll-up of the tip leakage vortex and higher measured pressures.

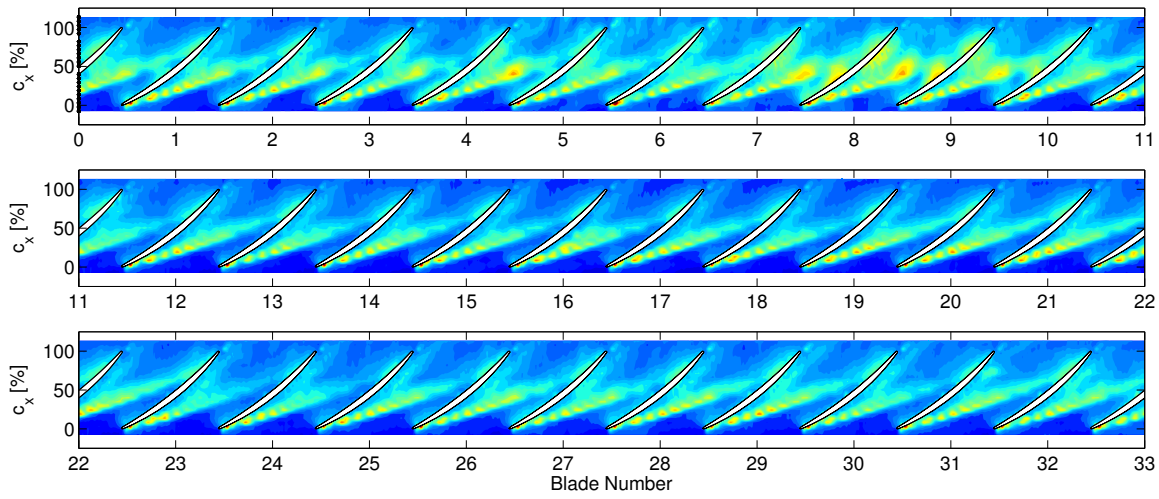


Figure 3.32: Mean passage revolution RMS pressure unsteadiness for R2 at 88EO-1CWB HL.

The pitchwise locations adjacent to the observable upstream vane wake typically have leakage flows nearing the neighboring blade's suction side with less RMS unsteadiness spread across the passage. As the shed upstream vane wake approaches and impinges on the rotor tips, the wake energy adds to the tip leakage flow and causes higher unsteadiness in the rotor passage. After the impingement, the tip leakage vortex begins to reach further across the passage and shows much higher local unsteadiness, particularly as it gets closer to the neighboring blade's pressure side. This increased unsteadiness in the tip leakage vortex develops for about one-third of the vane passage following the appearance and impingement of the wake. Effects of the flow incidence angle from the upstream stator

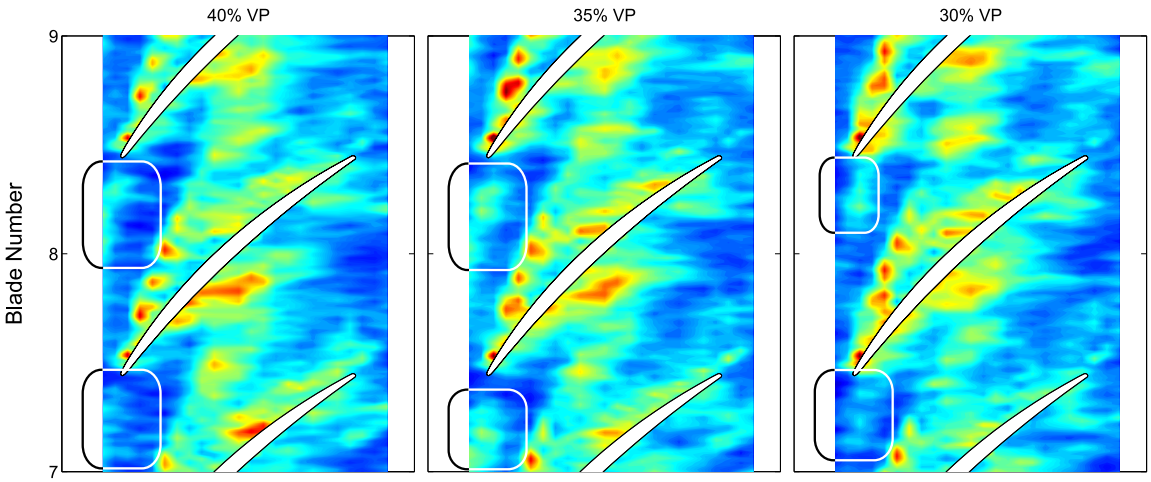


Figure 3.33: Upstream vane wake present in the 88EO-1CWB HL flow condition.

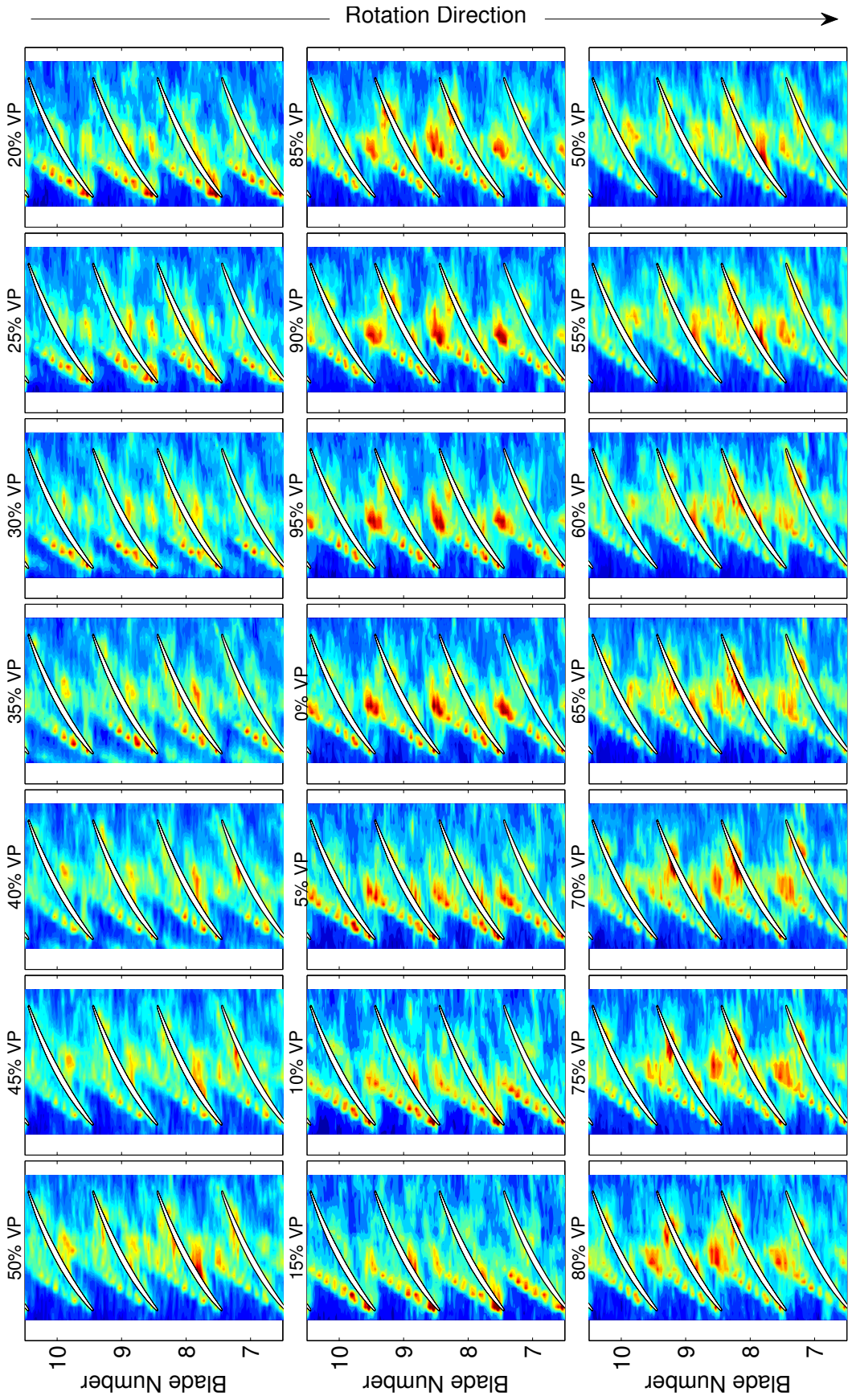


Figure 3.34: Full vane passage of over-rotor static pressure measurements of 88EO-1CWB HL flow condition.

vane can be identified in the ensemble average revolutions of Figure 3.34 with modulation of regions of greater unsteadiness around the rotor blades along the chord of the blade as a function of vane position. Sirakov and Tan (2003) state that while double-leakage tip clearance flow significantly decreases performance through blockage and loss, interaction of the rotor tip flow with steady upstream wakes has a beneficial effect on rotor double-leakage tip clearance flow behavior leading to improved performance. Circumferential locations associated with the upstream vane wake, between 30–40% vane passage, show lower unsteadiness in the rotor passage associated with the tip leakage vortex and the double-leakage flow. In contrast, vane positions between 70–95% vane passage show relative significantly higher unsteadiness of both flow phenomena.

Figure 3.35 shows a full vane passage of rotor exit plane measurements for Blades 7–10. Modulation of the unsteadiness associated with the tip leakage vortex, hub corner separation, and rotor wake occur as the vanes are traversed. These results show the importance the tip leakage vortex and hub separation have on the generated blockage through the rotor row. As the unsteadiness associated with these secondary flows increases, particularly between 32–48% vane passages, the effective flow area closes down through the middle of the rotor passage. This increased blockage causes a lower pressure rise across the rotor, previously identified in Figure 3.21 and Figure 3.23. The characteristic 3/rev modulation of the pressure signal in this machine caused by the difference in rotor blade counts is evident when considering the ensemble average revolutions. This 3/rev, although still occurring, is more difficult to detect in the over-rotor measurements since these signals are dominated by the embedded stage rotor. In contrast, the exit plane measurements, acquired in the axial gap between R2 and S2, show distinct evidence of the phenomenon occurring. The 3/rev modulation is expressed through stronger flow features occurring about one-third of the rotor circumference apart, or nearly every 11 blades for R2.

These stronger wakes, vortices, or separations, occurring about 120° apart at a particular vane passage location will then shift to different blades as a function of the upstream vane position. A particularly unique example of this 3/rev modulation occurs between

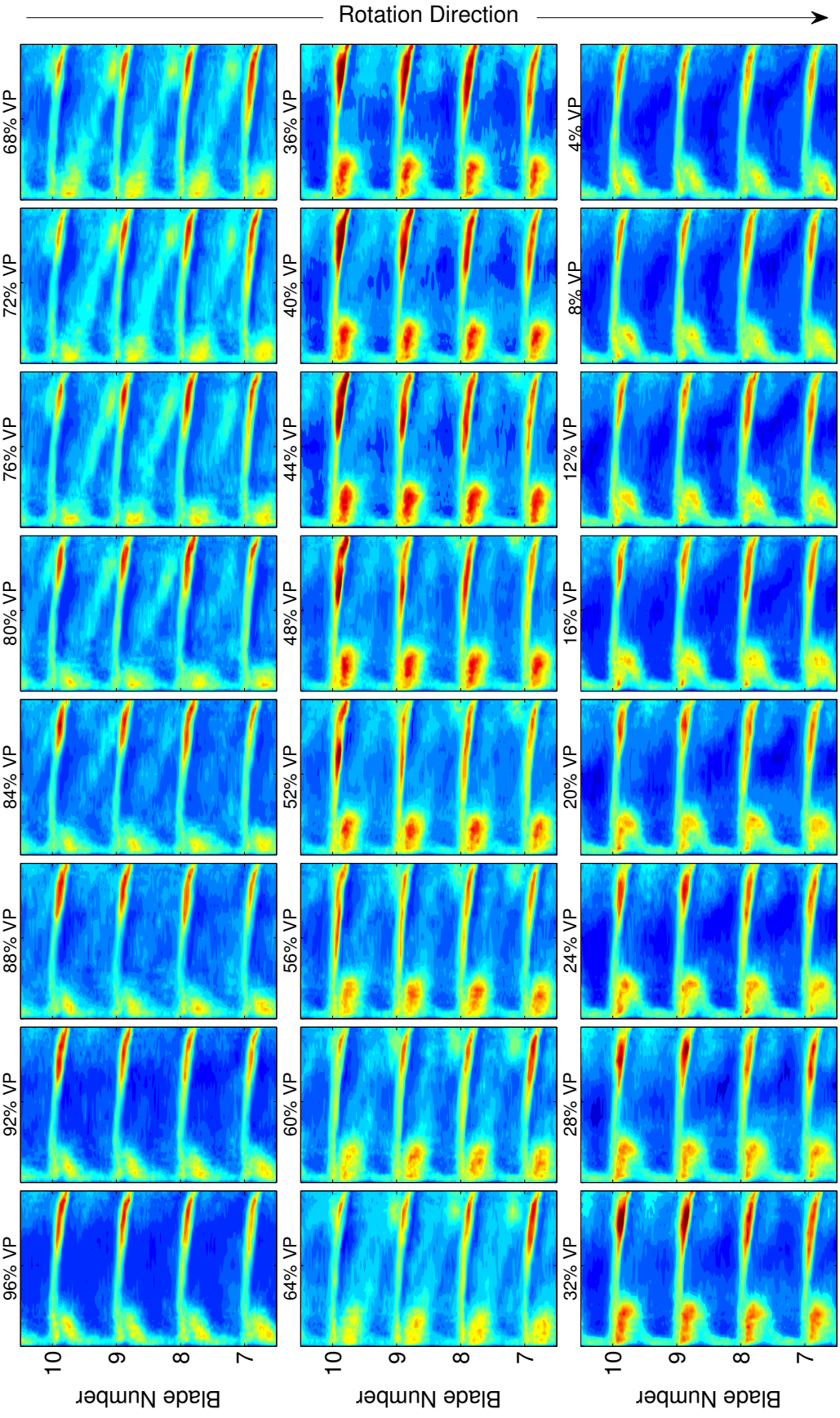


Figure 3.35: Full vane passage of rotor exit plane total pressure measurements of 88EO-1CWB HL flow condition.

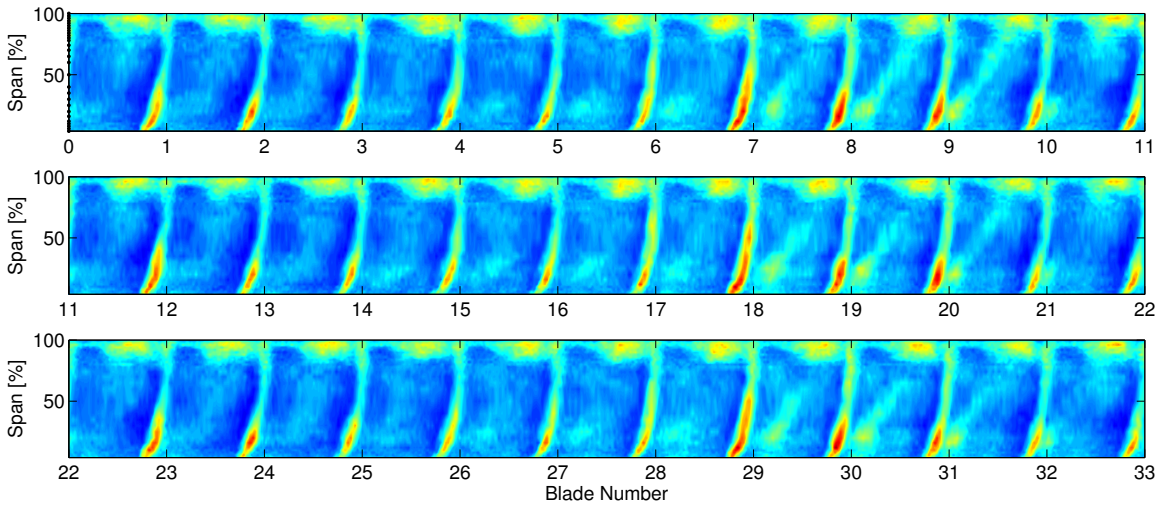


Figure 3.36: Ensemble RMS revolution of the 72% vane passage R2 exit plane for the HL 88EO-1CWB crossing.

approximately 60–80% vane passages measured at the exit plane. These circumferential regions show evidence of the upstream R1 wake at the exit plane of R2. This upstream rotor wake is identified by the band of greater unsteadiness connecting the region of hub separation on the suction side and the tip leakage vortex approaching the neighboring pressure side. This is identified as a rotor wake because of its connection with the 3/rev modulation, shown in Figure 3.36 for the 72% vane passage location. The wake can be identified every 11 rotor blades in the regions of Blade 8, Blade 19, and Blade 30. This pitchwise location, in particular, recorded strong enough wake-related unsteadiness at these regions for the wake to appear in the mean passage position of Figure 3.22.

The previous discussion demonstrates the importance of considering the pitchwise and blade-to-blade variations from the mean measurement when designing and analyzing turbomachinery. Popular methods of computational fluid dynamics boundary conditions between domains typically employ mixing plane and frozen rotor methods between stationary and rotating components. These methods, essentially, apply either the overall mean measurement (mixing plane) or a pitchwise mean measurement (frozen rotor) as boundary conditions and can miss important effects caused from variations from the mean. This is demonstrated in Figure 3.35, where high levels of fluctuation in the RMS pressure unsteadiness at the rotor exit plane are shown to occur across a full vane passage.

# 4. UNSTEADY LOADING OF EMBEDDED STAGE STATOR VANE

## 4.1 Unsteady Embedded Stage Stator Surface Pressures

High-frequency response pressure transducers flush-mounted with the pressure and suction sides of a stator vane passage measure the unsteady surface pressures at different positions of span and axial chord of the embedded stage within the vane passage. Measurements in this passage are significant for the identification and characterization of blade-row interactions of stationary and rotating flow components. Upstream wakes are one of the most prominent aerodynamic forcing functions in a multi-stage turbomachinery environment. These vortical disturbances in the flow field affect blade-rows downstream of their inception, and they may persist for several rows and interact with other wakes and flow structures. Jay & Fleeter (1993) identify four experimental facilities for the characterization of the aerodynamic gust: two-dimensional rectilinear cascades, stationary annular cascades, low-speed rotating machinery, and high-speed rotating machinery. Each facility has advantages and disadvantages, but the high-speed rotating facility is ideal for measuring quantities pertinent to forced vibration because engine-representative flow conditions can be achieved with realistic stage inlet and exit flows. Additionally, the essential synchronous vibration component of the rotating system is present, a component not present in stationary cascade studies.

The unsteady surface pressure measurements in the embedded stage vane passage are valuable for analyzing transient aerodynamics and the resulting forces causing vibratory response after the embedded stage rotor. Spectral analyses of these measurements can provide identification of the generating source of the synchronous excitation by isolating component frequencies, such as the various rotor blade-pass frequencies, from the response spectrum. The results of these data and analyses are beneficial for the design and validation of computational models and are particularly useful for flow-induced vibration models.

Identical signal processing methods discussed and applied in the previous chapter's measurements are similarly applied to these data. The 1/rev signal from the optical

tachometer to phase-locks the measurements in the stationary frame of reference to the rotor and allows partitioning of the time history into ensemble revolutions of measurements. This ensemble of revolution measurements is averaged into a mean revolution, with the number of revolutions comprising the ensemble revolution between 300 and 400 depending on compressor speed. The number of revolutions is a result of the acquisition time of the measurement and ensures a valid statistical representation of a rotor revolution.

Unlike the previous chapter, these measurements have been normalized by dynamic pressure based on rotor tip speed and are presented as surface gage pressure coefficients,

$$\langle C_P(t_\mathrm{i})\rangle = \frac{1/N \sum_{\mathrm{k}=1}^{N}[P(t_\mathrm{i})]_\mathrm{k}}{1/2\,\rho U_t^2}, \tag{4.1}$$

and surface pressure unsteadiness not locked to the rotor can be determined through the root-mean-square with respect to the ensemble average,

$$C_{P,\mathrm{RMS}}(t_\mathrm{i}) = \frac{\sqrt{\frac{1}{N}\sum_{\mathrm{k}=1}^{N}[P(t_\mathrm{i}) - \langle P(t_\mathrm{i})\rangle]^2}_\mathrm{k}}{1/2\,\rho U_t^2}, \tag{4.2}$$

defined for each revolution k and time i. The numerator of Equations (4.1) and (4.2) are the ensemble average pressure and the ensemble RMS pressure, respectively, introduced in the previous chapter. The terms in the denominator establish the dynamic pressure, denoted by $\rho$, inlet air density, and $U_t$, rotor tip speed, of the embedded stage. Inlet air density is obtained through the NIST-maintained fluid thermodynamic property database, REFPROP, using steady measurements obtained at the compressor inlet. This measurement normalization will allow better comparison between data acquired at different engine order crossings (different compressor speeds). Acquired data in the stator vane passage is limited to a single vane passage position for all conditions, as a detailed vane clocking study was not performed.

In addition to the pressure coefficient, a few metrics derived from the pressure coefficient are used to quantify each R2 blade's effect on the downstream stator, illustrated in Figure 4.1. The range of $C_P$ for each blade-pass period, denoted $\Delta C_P$, is the difference between the maximum and minimum values of the pressure coefficient. The mean $C_P$ for each blade-

pass period, denoted Avg $C_P$, is similarly computed and normalized by the overall revolution blade-pass period mean Avg $C_P$ and is presented as |Avg $C_P$|. While the illustration only depicts pressure side quantities, suction side values were calculated in the same way.

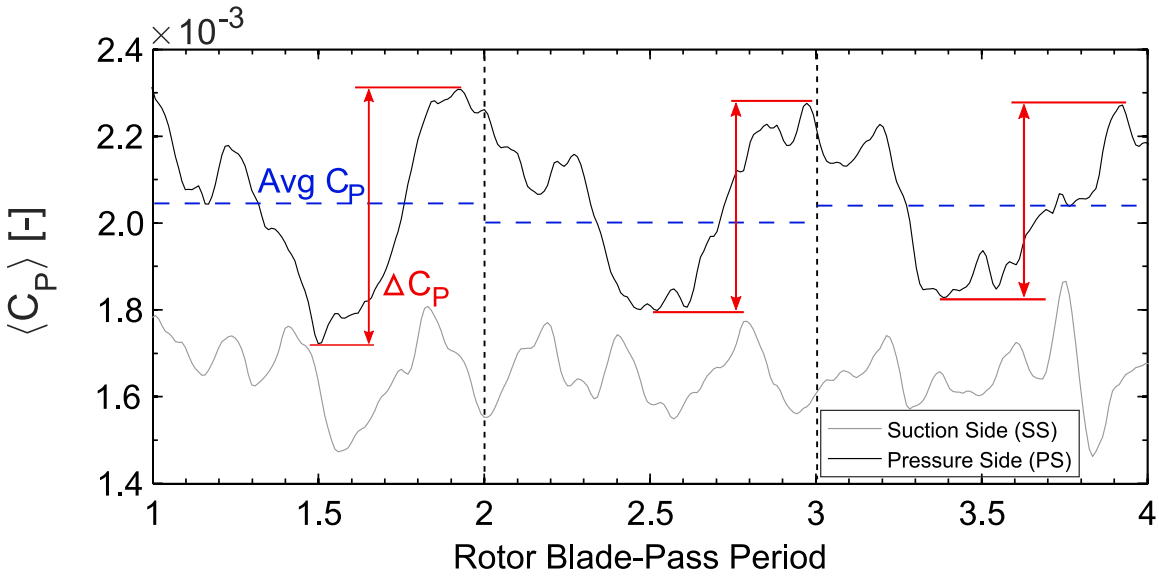


Figure 4.1: Illustrated definitions of Avg $C_P$ and $\Delta C_P$ for a blade-pass period.

Axial variation in surface pressure coefficient for the 88EO-1CWB crossing is shown in Figure 4.2 as mean surface pressure coefficients with bars showing the minimum and maximum measured coefficients. The PE condition measurements are shown in Figure 4.2a, represented by blue markers, and the HL condition, Figure 4.2b, are designated with red markers. Pressure side values have been assigned black lines and suction side values have gray lines. These conventions will be maintained for the remainder of this chapter. In the PE case of Figure 4.2a, the 50% span sensors show a 23.4% decline in suction side pressure coefficient near the front of the vane before a minimum is reached at 30% axial chord, whereupon pressure coefficient increases 10.6% toward the midchord. Similarly, the pressure side measurements show a pressure coefficient decrease of 16.7% across the chord before increasing after 30% axial chord by 10.5%. Between the 10% and 40% axial chord measurement locations at 50% span, the pressure side shows an overall drop in pressure coefficient of 7.9% and the suction side shows an overall pressure coefficient decrease of

15.3%. At the PE 80% span measurement locations, the pressure side shows an initial pressure coefficient rise of 7.8% between 10–20% axial chord before a subsequent drop of 7.3% between 20–30% axial chord. After 30% axial chord, the pressure begins rising again and realizes a pressure coefficient increase of 10.1%. The suction side, although absent the 20% chord sensor, shows a continual static pressure rise, with nearly equal pressure coefficients measured at the 30% and 40% axial chord locations when compared with the pressure side measurements. The overall pressure coefficient of the pressure side increases axially by 10.0% and the suction side increases by 15.1%. At the HL condition, Figure 4.2b, the pressure side at 50% span shows a continual increase in surface pressure coefficient, with an overall increase of 22.9%. The suction side, after an initial decrease between 10–20% axial chord, shows a similar profile with an increase of 16.0%. The HL 80% span measurements of both vane pressure and suction sides exhibit a similar profile to the PE 80% span pressure side measurements. The pressure side shows a slight 0.24% pressure coefficient increase between 10–20% chord before decreasing 8.3% and

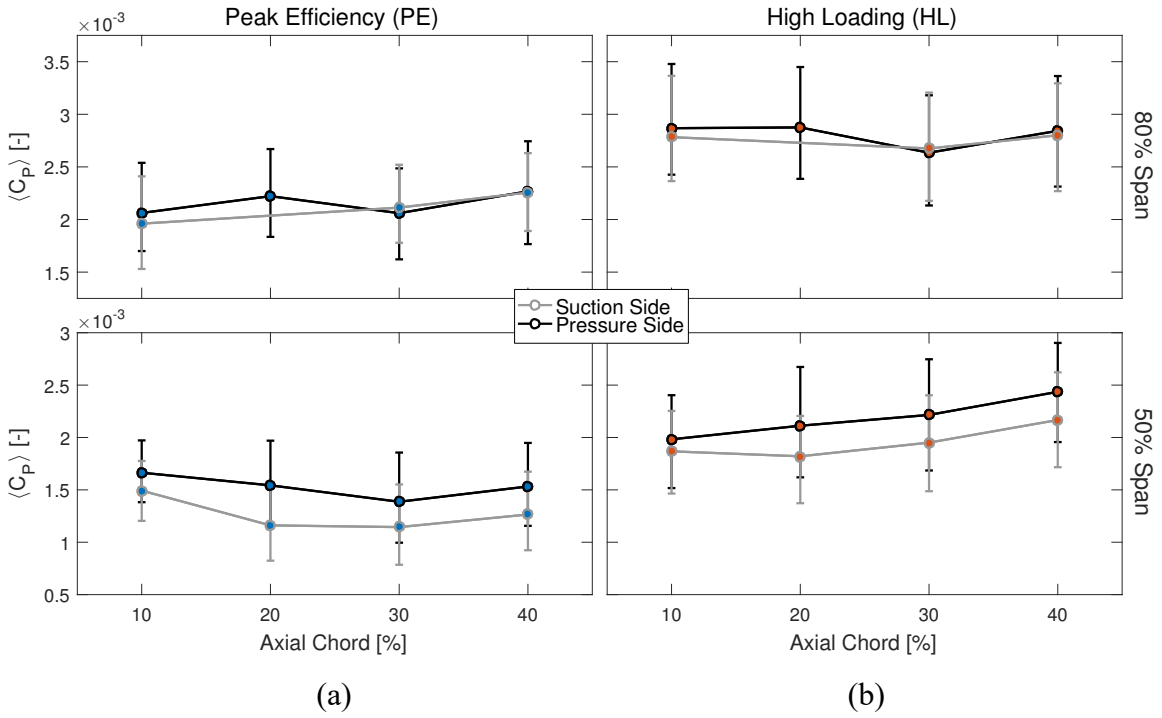


Figure 4.2: Axial variation of stator surface pressure coefficient for the 88EO-1CWB crossing at both spanwise locations.

subsequently increasing by 7.9%, resulting in an overall pressure coefficient decrease of 0.87%. The suction side shows a similar trend, however with an overall increase in pressure coefficient of 0.65%. Surface pressure coefficient, or static pressure, is expected to rise through diffusion across the stator vane; however, it is important to note the results shown in Figure 4.2 assume one-dimensional flow occurring between axial measurement locations and do not necessarily reflect the three-dimensional flow environment.

Using the metrics introduced in Figure 4.1, the results from the 10% axial chord measurement locations, the sensor positions nearest the leading edge, are shown in Figure 4.3 for both PE (Figure 4.3a) and HL (Figure 4.3b) conditions at each spanwise location. All measurement locations within the passage exhibit the 3/rev beating pattern in the ensemble average revolution trace of the pressure coefficient of the unsteady loading occurring in the ensemble average revolution pressure coefficient due to the difference in rotor blade counts. Peak pressure coefficients of the ensemble average revolutions register near Blades 11, 22, and 33. These relatively greater pressure coefficients linked to the 3/rev are caused by the interaction and combination of the R1 and R2 wakes before travelling through the downstream stator vane passage. Comparing the pressure coefficient traces with their respective dynamic range ($\Delta C_P$) and mean values (|Avg $C_P$|), correlations are shown to exist between these maximums and the peak pressure coefficient values of the ensemble average revolution occurring with the periodic 3/rev pattern.

The 50% span PE measurements show greater influence of the dynamic rotor wakes occurring on the pressure surface, where the difference in minimum and maximum values is 89.7% whereas the 50% span suction surface has a difference of 77.7% between extrema. Each surface measures the largest changes in the dynamic range to be more than twice the smallest change. These fluctuations influence the static pressure measured on the stator vane surface, with differences between minimum values and maximum values of the normalized mean pressure coefficients of about 2.5% for both the pressure and suction sides. The 80% span PE measurements are similar; however, the suction side has the greatest difference between the minimum and maximum dynamic range values, 88.7%, while the pressure side shows a difference of 63.0%. The greatest change in the dynamic

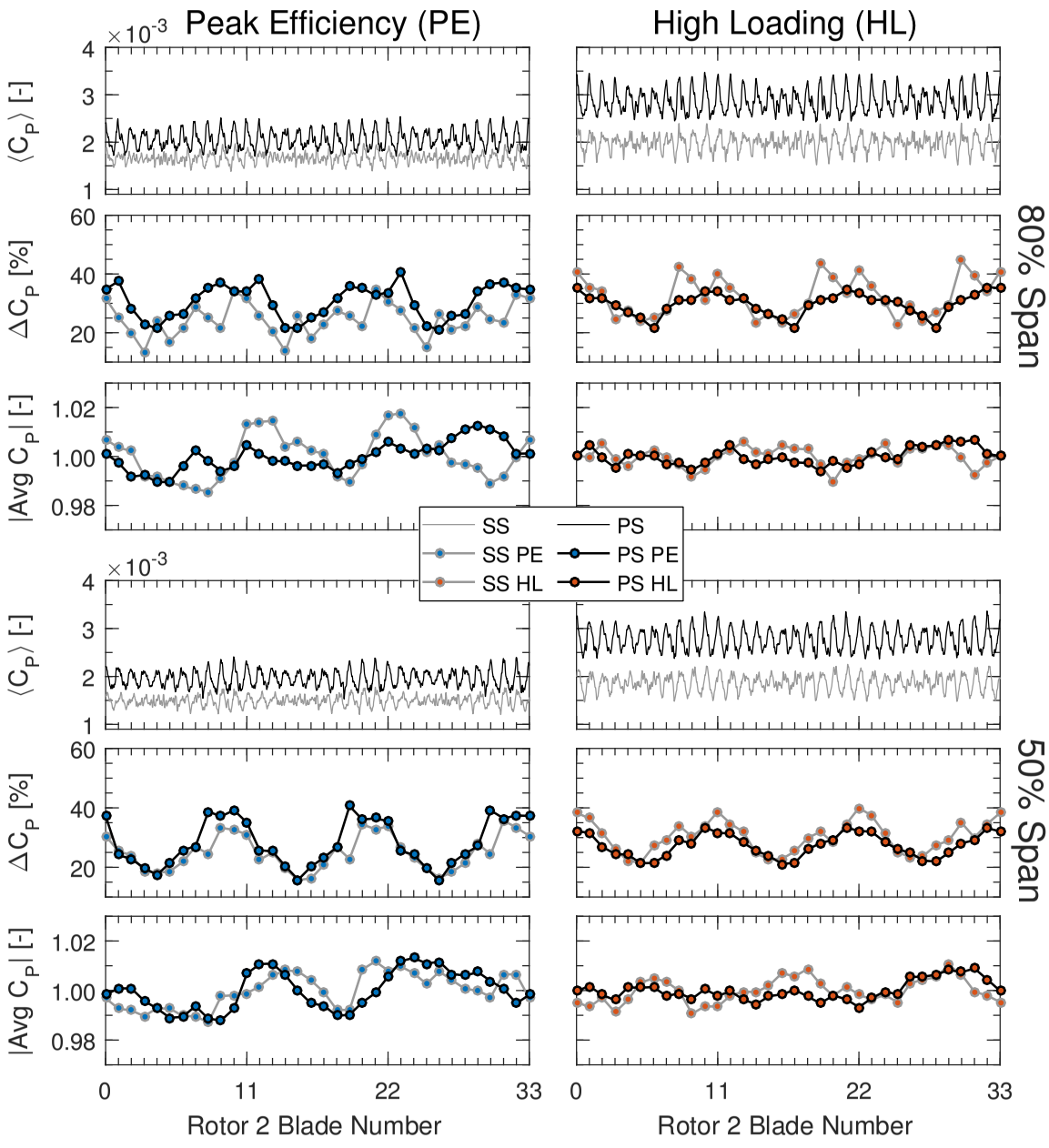


Figure 4.3: Surface pressure coefficient metrics of the 88EO-1CWB crossing measured at 10% axial chord.

(a) (b)

range at 80% span are about 2.6 and 1.9 times the minimum values for the suction side and pressure side, respectively. These surface pressure fluctuations are reflected in the mean pressure coefficients; the shapes of the data still exhibit the 3/rev modulation but the suction side peaks are greater and the troughs are lower than the pressure side measurements, resulting in differences in mean normalized pressure coefficients extrema of 3.2% for the suction side and 2.3% for the pressure side.

Increased loading to the HL condition, shown in Figure 4.3b for the 50% and 80% span locations, exhibits a corresponding increase in surface pressure coefficients for the respective pressure and suction sides of the vane passage. Comparing the pressure coefficient trace mean lines, the 50% span suction side pressure coefficient increases by 25.1% and the 80% span suction side increases by 19.2%. The stator vane pressure sides show greater increase with loading, with the 50% span pressure coefficient increasing by 41.9% and the 80% span increasing by 39.1%; 1.67 times the suction side increase at 50% span and just over twice the suction side increase at 80% span. The mean ensemble average revolution pressure coefficient is nearly uniform spanwise for the pressure side surfaces at both loading conditions. At PE, the difference in spanwise mean measurements is about 5.1% for the pressure side whereas increased loading to the HL condition decreases this difference to about 3.0%. The suction side measurements are similar, but have slightly larger spanwise differences. At PE a spanwise difference of 10.8% exists while the HL condition exhibits a difference of about 6.0%.

In addition to the greater mean line of the pressure coefficients, the peak-to-peak amplitude of the oscillating signals has also grown. Despite the greater relative increase in pressure side coefficient increases, it is the suction side measurements having the greatest dynamic range at both spanwise locations. At 80% span, the suction side shows greatest differences in the minimum and maximum dynamic range of 65.0% and 60.2% difference at 50% span. Comparing this with the pressure side, the 80% span has a largest difference of 49.9% and 50% span's largest difference is 45.3%. Although the oscillation amplitude of the ensemble average revolution signal has increased, the differences in dynamic range have slightly decreased between loading conditions for all measurement locations. These differences

correspond with the largest changes in dynamic range at 80% span of 1.6 to 1.9 times the minimum values for the pressure side and suction side, respectively. Similarly, the 50% span shows largest changes in dynamic range of 55.3% for the pressure side and 75.3% for the suction side. Like the dynamic range differences, these changes in values are less for the PE condition. The normalized mean pressure coefficients of the increased loading condition show less overall change relative to the lower loading condition for each span location. A 3/rev pattern is still evident, but is less pronounced than at the PE condition. Particularly for the 80% span location pressure side, the 3/rev feature manifests as a repeating double peak 3/rev (6/rev) with the first peak typically being slightly larger than the second peak.

At the 50% span pressure side, this double peak 3/rev (6/rev) modulation is also present, however all peaks emerge at similar values. These extra disturbances in the ensemble average revolution indicate secondary flow-field structures to the upstream rotor wakes, most prominently the tip leakage vortex or separation at the hub endwall. The normalized mean pressure coefficient on the 80% span suction side follows the 6/rev pattern of the pressure side; however, the 50% shows less evidence of this secondary disturbance and only appears to exhibit the 3/rev modulation. The increased loading and presence of these 6/rev patterns coincides with more level normalized mean coefficient profiles; the differences between minimum and maximum values of these coefficients are less than the corresponding coefficients PE condition measurements. Compared with the PE condition, the 80% span positions have differences between minimum and maximum values of 1.3% for the pressure side and 1.7% for the suction side whereas the 50% span measurements

Table 4.1: Greatest differences in dynamic range and normalized mean of the pressure coefficient and example of the change in dynamic range.

| | **Peak Efficiency (PE)** | | | **High Loading (HL)** | | |
|---|---|---|---|---|---|---|
| **80% Span** | **$\Delta C_P$ Difference** | **$\Delta C_P$ Change** | **\|Avg $C_P$\| Difference** | **$\Delta C_P$ Difference** | **$\Delta C_P$ Change** | **\|Avg $C_P$\| Difference** |
| Pressure Side | 63.0% | 80.0% | 2.3% | 49.9% | 64.0% | 1.3% |
| Suction Side | 88.7% | 155.6% | 3.2% | 65.0% | 87.1% | 1.7% |
| **50% Span** | **$\Delta C_P$ Difference** | **$\Delta C_P$ Change** | **\|Avg $C_P$\| Difference** | **$\Delta C_P$ Difference** | **$\Delta C_P$ Change** | **\|Avg $C_P$\| Difference** |
| Pressure Side | 89.7% | 156.5% | 2.5% | 45.3% | 57.8% | 1.6% |
| Suction Side | 77.7% | 111.7% | 2.5% | 60.2% | 80.1% | 2.0% |

show slightly greater differences of 1.6% and 2.0% for the pressure side and suction side, respectively. The differences and changes between loading conditions, span positions, and vane surfaces is summarized in Table 4.1.

The ensemble average revolution pressure coefficient traces shown in Figure 4.3 can be partitioned into three sets of eleven blade-pass periods and superimposed to demonstrate the repeatability of the 3/rev pattern present through the revolution, and is shown in Figure 4.4 for the HL 80% span measurements on the pressure and suction sides of the vane. The slight variations between the one-third ensemble average revolution sections are recognized as blade-to-blade variation in flow associated with blade-row interactions or due to slight variations in rotor blade geometry—manufacturing variation, blade wear, etc. An important result of this repeatable pattern is the reduction of the computational domain of this rotor by two-thirds would accurately capture the upstream forcing function and resulting unsteady loading on the vane passage surfaces.

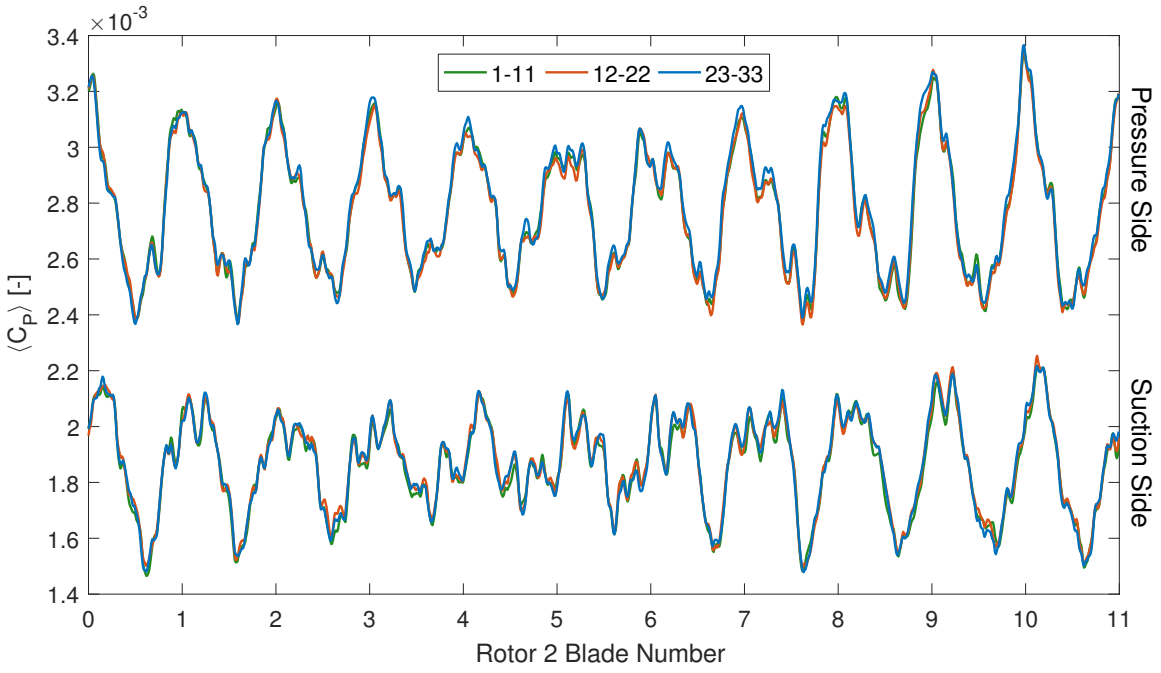


Figure 4.4: 3/rev modulation and repeatability across one-third sections of the R2 blade-row.

Computing the root-mean-square with respect to the ensemble average revolution allows the quantification of the unsteadiness of the surface pressure fluctuations independent of the phase-locked signal. Figure 4.5 shows the results of RMS pressure unsteadiness of both loading conditions measured at the 10% and 40% axial chord locations for 50% and 80% spanwise positions. Peaks in the RMS pressure coefficient indicate disturbances in the flow from the upstream rotor, namely the rotor wake and tip leakage flows. Results from the 10% axial chord measurement locations on the pressure and suction sides of the vane passage, Figure 4.5a, show these RMS pressure coefficient peaks occurring in many of the mean blade-pass period waveforms. This axial measurement location is closest in proximity to the upstream rotor, and is reflected in the strength of the unsteadiness peaks, particularly near the tip of the 80% span measurements. PE condition measurements, shown in blue, have a lower baseline unsteadiness than the HL conditions shown in red; however, maximum values of both loading condition measurements are nearly equal.

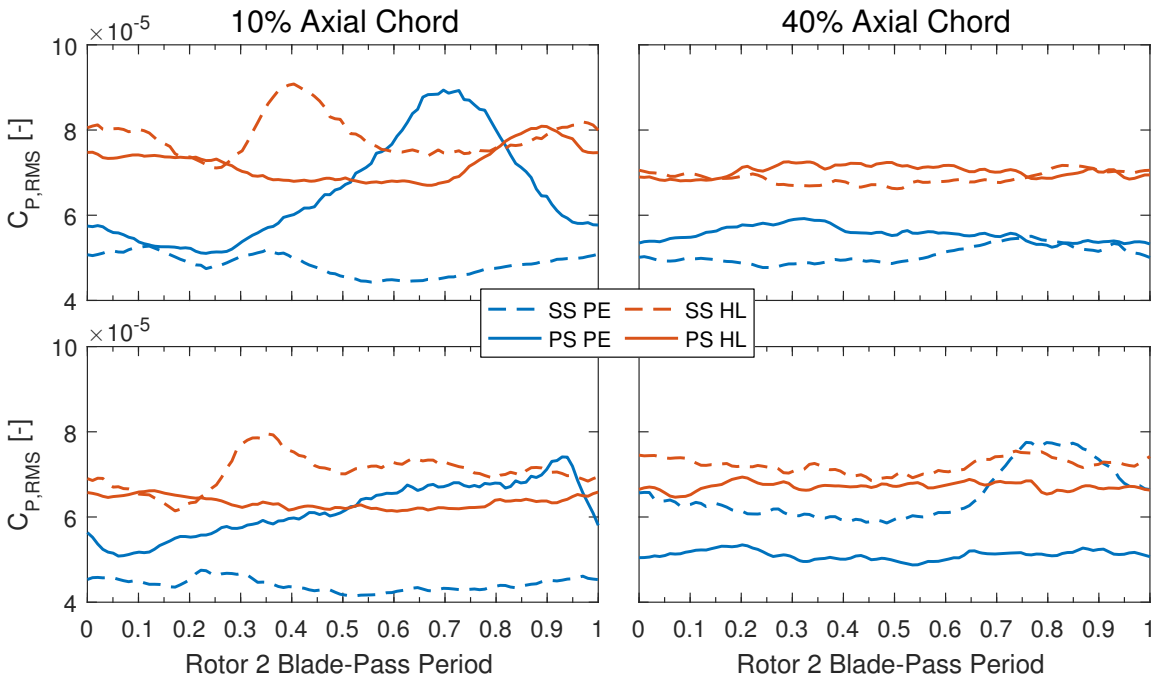


Figure 4.5: RMS surface pressure unsteadiness the 88EO-1CWB flow condition.

The PE suction side measurements at both spanwise measurement locations show low levels of unsteadiness compared while the PE pressure side sensors register some of the greatest unsteadiness peaks measured at the 10% axial location for their respective span positions. This trend is quite different when loading is increased to the HL condition. The HL suction side measurements show the greatest unsteadiness whereas the pressure side measurements are nearly flat, except for the bump in the latter one-third of the blade-pass period for the 80% span HL pressure side measurement. In association with this shift of unsteadiness from the suction side to the pressure side of the vane, a shift in the upstream rotor blades causing the disturbance also occurs. At 80% span this peak is shifted from PE pressure side at about Blade 23 to HL suction side at about Blade 13. At 50% span the shift occurs from the PE pressure side near Blade 31 to the HL suction side at about Blade 12. Each location shows a blade-shift in the peak of about 10 blades, or one-third of the rotor revolution. Closer to the midchord, 40% axial chord shown in Figure 4.5b, unsteadiness levels are typically flat when compared to the measurements near the leading edge of the vane. However, a peak in the PE suction side measurement at 50% span is evident near Blade 27. In contrast to the 10% chord measurements, where the PE suction side measurement was lowest across the revolution, the PE 40% chord measurement shows both a greater baseline unsteadiness than the PE pressure side as well as the greatest unsteadiness measured at this location for both loading conditions.

## 4.2 Spectral Analysis of Unsteady Surface Pressure Measurements in the Embedded Stage Vane Passage

Similar frequency analyses as applied to the over-rotor and rotor exit plane static pressure measurements can identify the driving sources of surface pressure fluctuations within the passage. The embedded pressure transducers of the vane passage are unscreened, and have a dynamic frequency response of more than five times the screened transducers installed in the casing endwall and radially traversed behind the rotor. Discrete Fourier transforms of the ensemble average static pressures have been performed for the previously selected sensor locations to compare the amplitude density of the signal in each frequency (engine order) band, and is shown in Figure 4.6 for the 88EO-1CWB crossing.

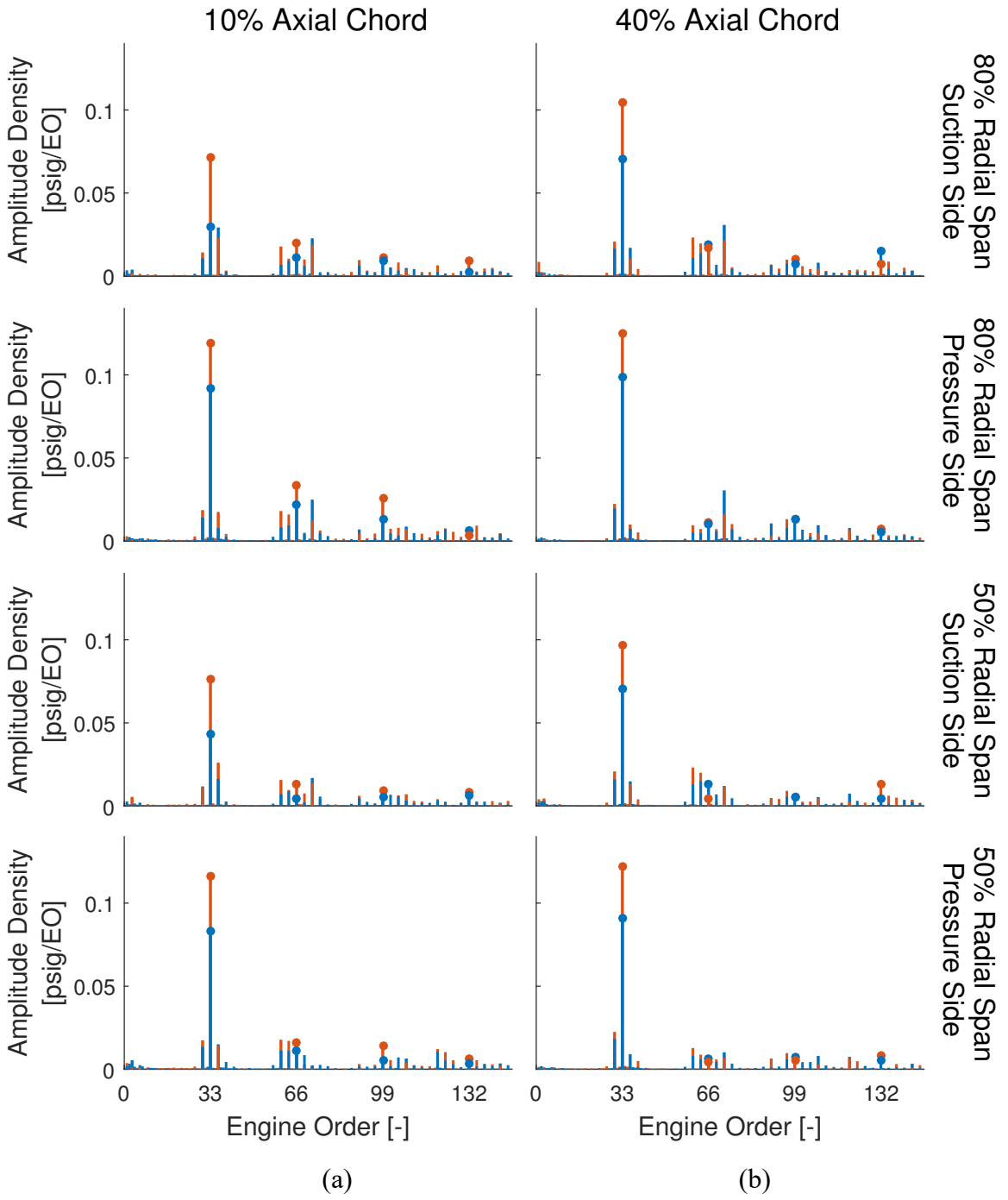


Figure 4.6: Amplitude density spectra of the 88EO-1CWB crossing.

The baseline vane count configuration exhibits expected trends based on rotor geometry. The R2 blade-pass frequency dominates the spectrum at all measurement locations and loading conditions. The measurements of the sensors located at 10% axial chord (nearest R2) are shown in Figure 4.6a and the sensors located at 40% axial chord are shown in Figure 4.6b. Spanwise measurements near at 10% chord 80% span show greater overall amplitude densities measured on the pressure side when compared with suction side measurements. At PE, the 80% suction side shows relatively strong first and second harmonics of the R1 blade-pass frequency response in addition to the R2 blade-pass frequencies. This indicates the R1 wake (36EO) and R1 tip leakage flow (72EO) have persisted through the embedded stage rotor and have a measurable influence on the suction side of the vane near the tip. At PE, the influence of the R1 blade-pass frequency on the suction side spectrum is nearly equal to the R2 blade-pass frequency. The second harmonic of these fundamental blade-pass frequencies actually shows a greater influence on the spectrum caused by R1 at PE. Pressure side measurements show a much stronger response corresponding with the R2 blade-pass frequency and its harmonics compared to the suction side, however, a strong second harmonic of R1 is, again, present.

Further downstream, at 40% axial chord, the R2 blade-pass frequency response has more than doubled on the PE suction side while its second harmonic has remained relatively unchanged. The second harmonic response of R1 has similarly increased by 35.7% while the fundamental frequency has decreased by about 26.7%. As the sensor positions are closer to the source of the R3 blade-pass frequency, the first and second harmonics of these engine orders has slightly increased. Frequency response of the R2 blade-pass frequency increases with loading condition. On the suction side, at 10% chord, R2 response increases by more than double while the 40% chord amplitude increases by a factor of nearly 1.5. Pressure side measurements experience a smaller loading-induced change in R2 response, and at 40% chord, the R2 second harmonic is nearly the same for both loading conditions.

Near the midspan of the vane passage at 50% span, the R2 blade-pass frequency dominates the spectrum for the suction and pressure sides of the vane. Similar amplitude levels occur on both surfaces for all rotor second harmonics except for R1 on the pressure side where

the response has nearly disappeared. The 10% axial chord generally shows a slightly higher amplitude associated with R1 when compared with R3 on the suction side whereas the pressure side measurements show little change. At 40% chord, the proximity to R3 blade-row increases the R3 blade-pass frequency magnitude relative to that at the R1 blade-pass frequency, however, the R2 blade-pass frequency amplitude still dominates the spectra. Increased loading has similar effects to the 80% span measurements, with an increase of R2 blade-pass frequency magnitude at all measurement locations.

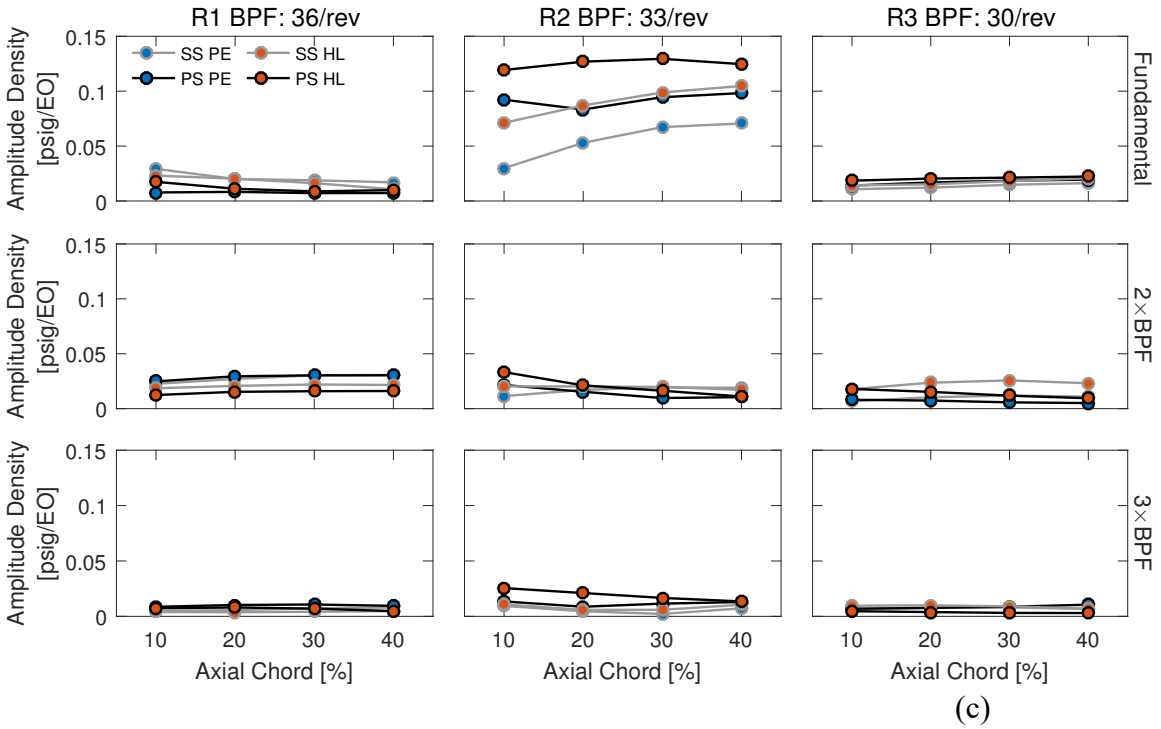


Figure 4.7: Axial variation of amplitude density at 80% span for 88EO-1CWB.

Axial variation of the amplitude densities measured at 80% span are shown in Figure 4.7 for the baseline vane count configuration at the PE and HL 88EO-1CWB operating conditions. The first three harmonics of each blade-pass frequency response are shown: Figure 4.7a contains R1 harmonics (36/rev, 72/rev, 108/rev), Figure 4.7b shows the embedded R2 harmonics (33/rev, 66/rev, 99/rev) and Figure 4.7c comprises R3 harmonics (30/rev, 60/rev, 90/rev). Harmonics of the 3/rev are not shown as these frequency responses were typically at least one order of magnitude below the lowest blade-pass frequency response. This axial variation in the frequency response of the system produces similar

conclusions from the full amplitude density spectra of the replicated ensemble-average revolution signal, but limiting the data selection to the pertinent blade-pass frequency harmonics can help trends become more apparent. For the 88EO-1CWB conditions, the R1 and R3 blade-pass frequency responses are low and show small changes when compared to the fundamental R2 blade-pass frequency. As previously indicated, proximity of the sensor locations to the blade-pass frequency source influences the associated frequency response. The fundamental R1 blade-pass frequency magnitudes are typically slightly higher at 10% chord than at 40% chord while the R3 blade-pass frequency amplitudes show the opposite trend. The R1 and R3 higher harmonics typically show slight increases in spectral magnitude across the axial chord. The suction side fundamental R2 blade-pass frequency amplitudes of the PE and HL flow conditions have nearly identical trends as they increase across the axial chord. The 10% chord sensor measurement of the PE pressure side shows an initial stronger response before a decrease in response of 9.7% between the 10% and 20% axial chord locations. After 20% chord, the amplitude trend follows suction side trends quite closely, particularly the HL suction side response. The HL pressure side shows amplitude density increasing 8.5% from 10–30% chord before a 3.8% decrease between 30% and 40% axial chord.

## 4.3 Effects of Reduced Vane Count Upstream Stator on Unsteady Loading of Embedded Stage Stator Vane Passage

As part of the concurrent aeromechanical investigation of the forcing function on the embedded stage from an upstream vane-row, a symmetric, reduced vane-count stator vane was designed and manufactured with 38 vanes to study the effects of disrupting the sequence of consecutive 44 vane-count vane-rows of the IGV, S1, and S2. This reduced vane-count configuration will also provide a new reference configuration to compare to an asymmetric S1 vane-count configuration to investigate the capability of non-uniform vane spacing to modify the strength and phase of unsteady aerodynamic forcing functions on the embedded stage. Although the same forced response mode (1CWB) is under investigation, the rotational speed that the mode occurs has shifted to a higher range and a lower frequency normalized by rotational speed. For the reduced vane count, 76EO-1CWB describes the higher-order chordwise bending mode.

The aerodynamics and unsteady loading of the reduced vane-count configuration are largely the same when the measured pressures are normalized by the rotational dynamic pressure to obtain the surface pressure coefficient. The increased speed of the compressor results in higher pressures generated through the machine. At PE, the 80% span suction side coefficients decrease between 8–13% and the 80% span pressure side coefficients increase between 5–20%. Coefficients at the 50% span suction side change by -6% to 5% and the 50% span pressure side values increase from 3–12%. Increased loading causes similar changes; with greater relative changes occurring at 80% span pressure side between 10–20% chord than between 30–40% chord due to the increased incidence and associated increased front-loading of the vane in the tip region. The 80% suction side surfaces show smaller relative changes between configurations, but it has increased pressure coefficients occurring at the 40% chord location. The 50% span measurements show overall greater increases in pressure coefficients for all measurements except the 10% chord suction side.

The resulting changes in surface pressure coefficients are summarized in Table 4.2, and the supporting data are included in Appendix C. Between S1 configurations, two sensors malfunctioned: the 80% span 10% chord sensor on the suction side and the 50% span 20% chord sensor on the pressure side in addition to the sensor located on the 50% span 20% chord on the suction side. For this reason, the sensor nearest the leading edge on the 80% span suction side is the 20% chord. Measurements from this sensor will be shown for the reduced vane count, with a notation in the figure shown for clarity.

Table 4.2: Change in surface pressure coefficients between baseline 88EO-1CWB and reduced S1 vane-count 76EO-1CWB.

| | **Peak Efficiency (88EO to 76EO)** | | | | **High Loading (88EO to 76EO)** | | | |
|---|---|---|---|---|---|---|---|---|
| **80% Span** | **10% Chord** | **20% Chord** | **30% Chord** | **40% Chord** | **10% Chord** | **20% Chord** | **30% Chord** | **40% Chord** |
| Pressure Side | 6.3% | 5.1% | 19.2% | 9.5% | 7.5% | 8.4% | 18.7% | 8.4% |
| Suction Side | - | -12.3% | -10.3% | -8.4% | - | -3.4% | -0.6% | 1.1% |
| **50% Span** | **10% Chord** | **20% Chord** | **30% Chord** | **40% Chord** | **10% Chord** | **20% Chord** | **30% Chord** | **40% Chord** |
| Pressure Side | 3.3% | - | 11.9% | 10.4% | 8.7% | - | 14.2% | 12.9% |
| Suction Side | -5.7% | - | 5.1% | 3.2% | -2.0% | - | 7.0% | 5.9% |

The reduced upstream vane-count and increased rotational speeds have caused distinct changes in the amplitude density spectra of the 76EO-1CWB crossing, shown in Figure 4.8, when compared with the 88EO-1CWB crossing spectra. Sensors nearest the leading edge, 10% axial chord with the noted exception at 80% span suction side, are shown in Figure 4.8a and sensors at 40% axial chord are shown in Figure 4.8b. The fundamental R2 blade-pass frequency is less dominant in the spectra for the reduced count configuration, despite faster rotational speed and greater work being imparted into the flow. At PE loading, the R3 blade-pass frequency (30EO) exhibits the highest amplitude response on the suction side for both span and axial locations. Pressure side measurements at PE conditions maintain the greatest amplitude density magnitude at the R2 blade-pass frequency, but they are closely followed by the R3 blade-pass frequency.

As loading is increased to the HL condition, the amplitude of the R2 blade-pass frequency nearly doubles, or in the case of the near leading edge suction side measurements increase by a factor of more than three. Despite this large increase in R2 blade-pass frequency amplitude on the suction side, the R3 blade-pass frequency maintains a similar amplitude. For higher harmonics of the R2 blade-pass frequency response, the PE 66EO response is surpassed by the 63EO for all measurements in Figure 4.8a and the pressure side measurements in Figure 4.8b. Higher R3 blade-pass frequency harmonics show strong response occurring as well, at PE the R3 second harmonic has smaller peaks than twice the R2 blade-pass frequency, but at HL the magnitudes are nearly equal for the suction side measurements. Near the leading edge, the HL 60EO response is greater than the 66EO response. In comparison to the baseline vane-count configuration, the spectra are spread among the nearby frequencies near the rotor blade-pass frequency harmonics.

Comparing the axial variation in amplitude response of the 76EO-1CWB fundamental blade-pass frequencies, Figure 4.9, to the 88EO-1CWB measurements in Figure 4.7 show the trend differences between engine order crossings. The R1 harmonics, Figure 4.9a, have smaller amplitude densities at the 76EO-1CWB despite the lower solidity S1 interfering with R1 exit flows. The fundamental R2 blade-pass frequency, Figure 4.9b, shows a

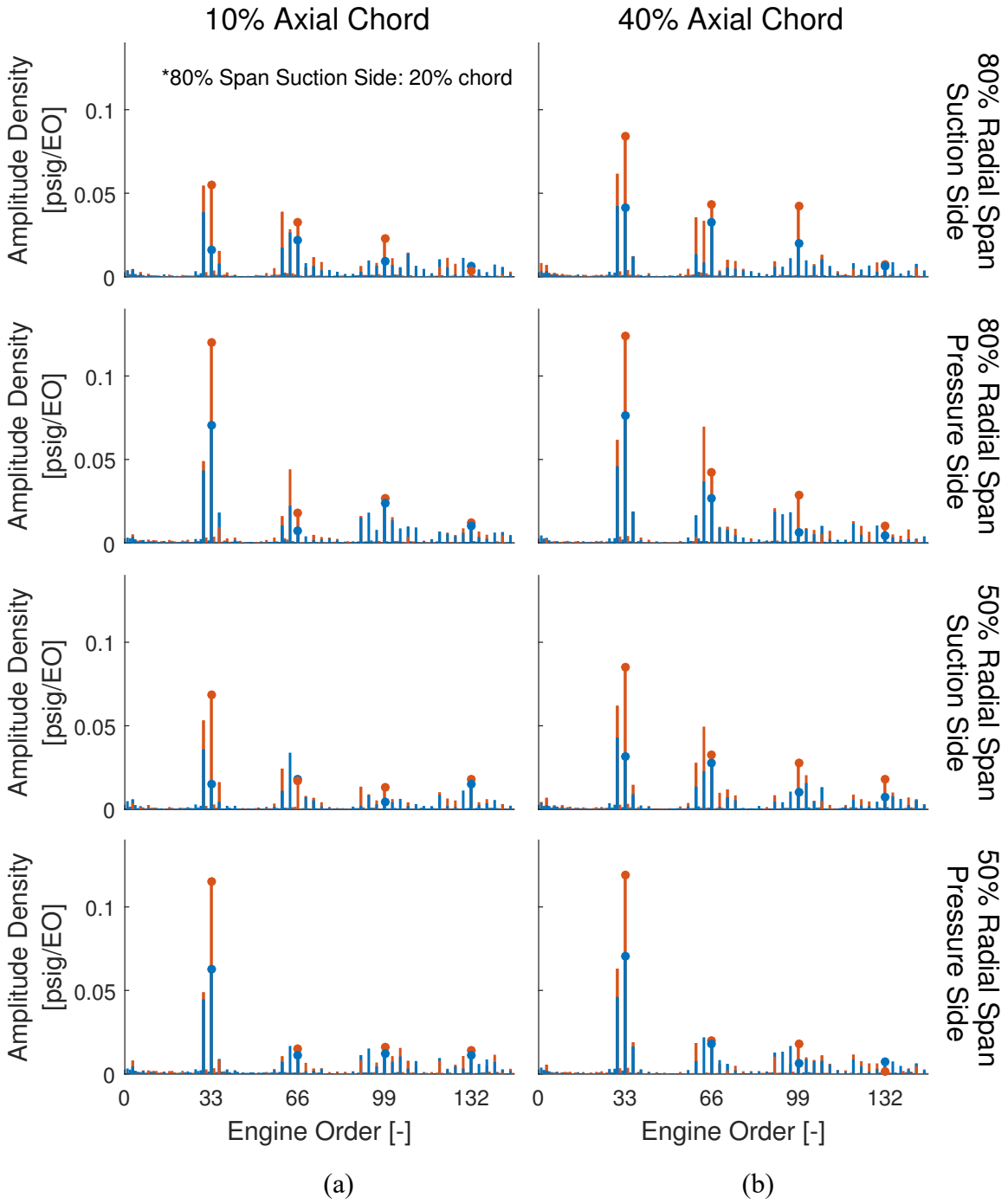


Figure 4.8: Amplitude density spectra of the 76EO-1CWB crossing.

decrease in amplitude response everywhere except the HL pressure side, where the response is nearly identical to 88EO-1CWB. The R2 harmonics increase in strength, and show an increasing trend across the axial chord. This trend is opposite the 88EO-1CWB R2 harmonic response, where a decrease occurs with axial chord. Second and third harmonics of the R2 blade-pass frequency show much smaller changes between vane surfaces and loading conditions, and several of these measurements show nearly equal or greater amplitudes than that of the fundamental R2 blade-pass frequency on the suction side surface.

R3 blade-pass spectral magnitudes have nearly doubled between engine order crossings. While the 88EO-1CWB R3 amplitude response shows little change for all vane surfaces and loading conditions, the HL pressure surface measurements of the 76EO show a relatively large separation in between the other measurement locations and conditions and nearly triple in amplitude density magnitude. The R3 second harmonic maintains similar amplitude between engine order crossings, apart from the HL suction side magnitude increasing by a factor of 1.5. The R3 third harmonic shows increased spectral magnitudes

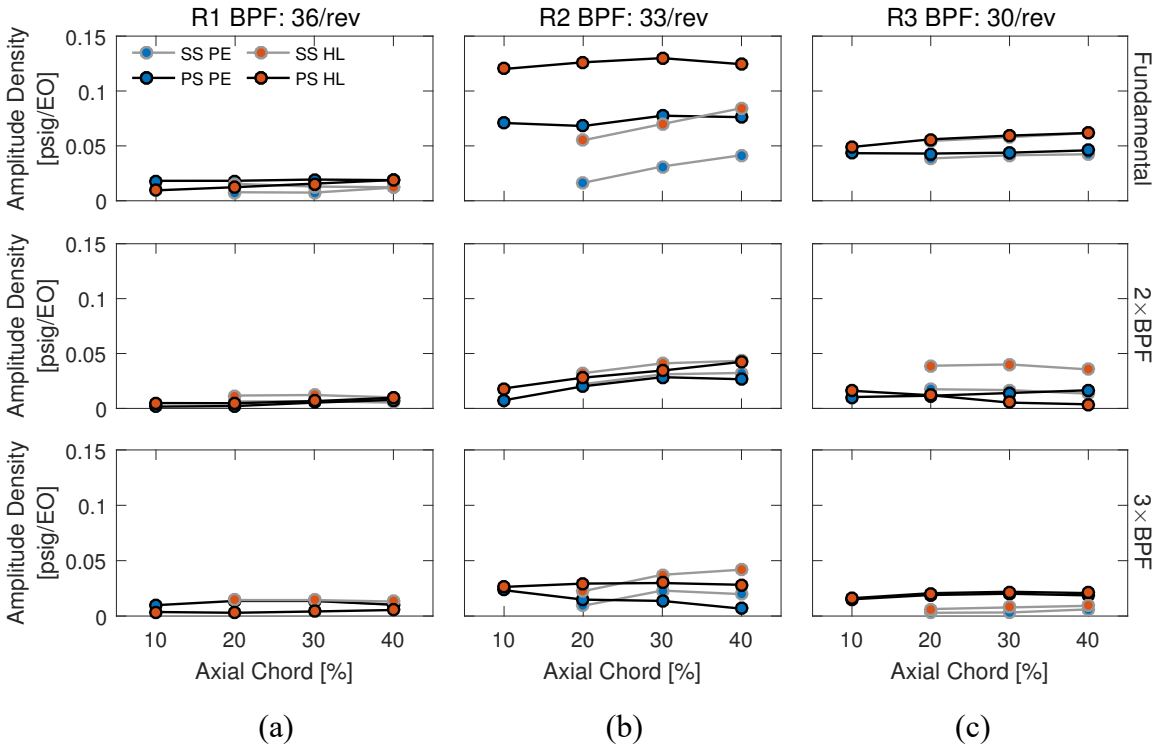


Figure 4.9: Axial variation of amplitude density at 80% span for 76EO-1CWB.

on the pressure side, nearly equal for both loading conditions, and have increased sevenfold between 88EO-1CWB and 76EO-1CWB conditions.

Increasing the speed of the reduced vane-count compressor configuration, the torsion mode crossing, 38EO-1T, is encountered on the Campbell diagram. Similar pressure coefficient trends to the 76EO-1CWB occur, with much lower changes between the engine order crossings. Between PE crossings, changes of -1.0% to 4.3% occur, while at HL conditions changes of 0.04% to 2.8% are measured. Similar spectral analyses of 38EO-1T data show interesting results and differ significantly from the 88EO-1CWB and 76EO-1CWB results. The amplitude density spectra of the 38EO-1T crossing is shown in Figure 4.10, with near leading edge measurements in Figure 4.10a and 40% chord measurements in Figure 4.10b. The ordinate scale of the 38EO-1T crossing spectra is nearly half that of the 88EO-1CWB and 76EO-1CWB spectra despite the higher rotational speed. The amplitude density spectra have much greater distribution, across any frequency bands when compared with the chordwise bending crossings.

The PE suction side measurements near the leading edge show similar amplitudes as those of the fundamental R2 and R3 blade-pass frequencies, with correspondingly low magnitude of the fundamental R1 blade-pass frequency. PE suction side measurements at 40% chord show the R2 blade-pass frequency response has decreased considerably at 80% span and is relatively low at 50% span. Fundamental PE pressure side measurements show greatest response of the R3 blade-pass frequency with similar amplitude levels of the R1 and R2 blade-pass frequency amplitude densities. PE measurements on the pressure side at 40% chord show similar amplitudes occurring for the fundamental R2 and R3 blade-pass frequencies, with a smaller relative magnitude in the R1 amplitude density. The second R2 harmonic near the leading edge shows greater amplitude magnitude than the R1 and R3 second harmonics at the 80% span pressure and suction sides and the 50% span pressure side. The 50% suction side shows greater amplitudes of the 63EO and 69EO produced from rotor blade-pass frequency and blade-count difference harmonics. Third and fourth harmonics on the vane surfaces near the leading sides show the R2 blade-pass frequency amplitude responses are stronger than the other rotor harmonic responses, excluding the

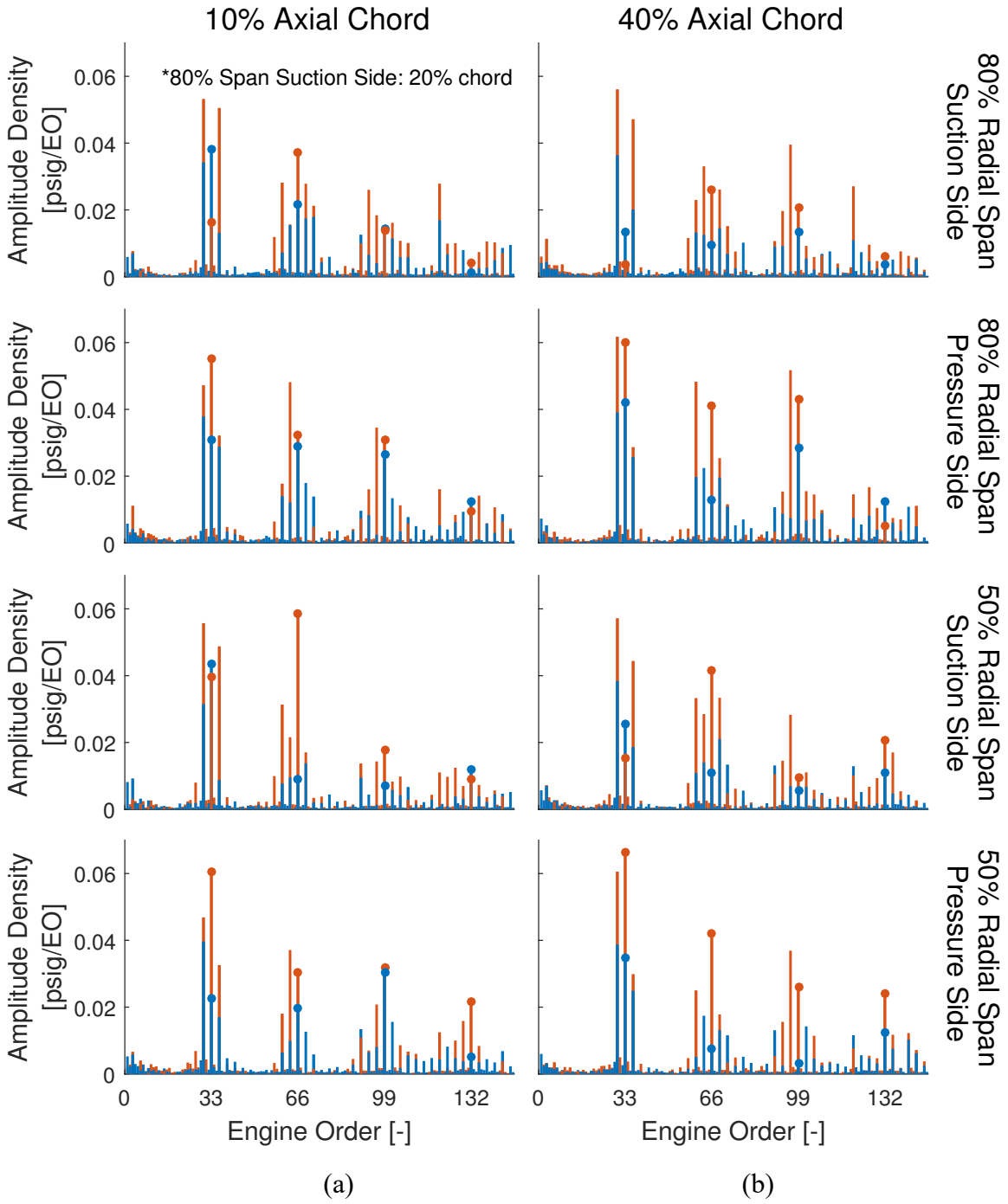


Figure 4.10: Amplitude density spectra of the 38EO-1T crossing.

fourth R2 harmonic at 80% suction side, with significant spread of spectral energy to the surrounding engine orders. At 40% chord, second harmonics of R2 have smaller responses than the R1 and R3 harmonics, as well as the dominant engine orders comprising rotor blade-pass harmonics and blade-count difference harmonics. Third harmonics dominate the nearby engine orders at 80% span, while they are less significant at 50% span and fourth harmonics typically show greatest response of their nearby frequencies.

The HL condition shows several significant changes in amplitude density response for every sensor location. At the 10% and 20% suction side sensors of 50% span and 80% span, respectively, the R1 and R3 blade-pass frequencies show greater amplitude magnitudes than the R2 blade-pass frequency. At 80% span, the R2 blade-pass spectral magnitude has decreased by 57.4% while the 50% span measurement is nearly the same. At the same locations, the 50% span and 80% span fundamental R1 response has increased by factors of 5.6 and 3.9, respectively, while R3 response has nearly doubled. While pressure side results show less increase in the R1 and R3 response, the R2 amplitude response has nearly doubled at 80% span and nearly tripled at 50% span. Fundamental HL rotor blade-pass frequency results at 40% chord are similar to PE conditions. The 80% span suction side R2 response has nearly disappeared while R1 and R3 have increased by factors of 1.5 and 2.3, respectively. Suction side results at 50% span follow a similar trend, increasing R1 and R3 response with decreasing R2 amplitude. HL pressure side results at 40% chord show nearly similar amplitudes between the fundamental R2 and R3 responses, each response has grown by nearly the same factor between loading conditions. Fundamental R1 response remains nearly identical between loading conditions.

Second harmonics of the near leading edge suction side sensors are show strong R2 response followed by R3. Several engine orders around the second harmonics of the rotor blade-pass frequencies also show significant response occurring. The second harmonic of the R2 blade-pass frequency at 50% span suction side has increased by 6.6 times with increased loading. Pressure side measurements are dominated by the 63EO and are followed by the 66EO. Frequency bands around the third and fourth rotor blade-pass frequency harmonics show strong responses of the 93EO and 96EO in addition to R2 and

R3 harmonics. Similar results occur at 40% chord, with significant response occurring at a central engine order and attenuating response at the nearby engine orders. At frequencies near the rotor blade-pass frequency second harmonics, this is typically the 60EO, 63EO, 66EO, or 69EO, near the third harmonic the central peak is the 96EO, and near the fourth harmonic the central peak is typically either the fourth harmonic of the R2 or R3 blade-pass frequencies.

To further compare the effects the 38EO-1T flow conditions have on the rotor blade-frequency harmonics, the axial variation of these magnitudes in Figure 4.11 can be compared to the previous Figure 4.7 and Figure 4.9. In contrast to the results of the 76EO-1CWB crossing, the results in Figure 4.11 show similar magnitudes occurring at all fundamental rotor blade-pass frequencies. The first and second harmonics of the R1 blade-pass frequency in Figure 4.11a have increased between 76EO-1CWB and 38EO-1T conditions. Particularly the HL measurements, where fundamental R1 response of pressure side measurements have increased by a factor of 1.5 and suction side response has

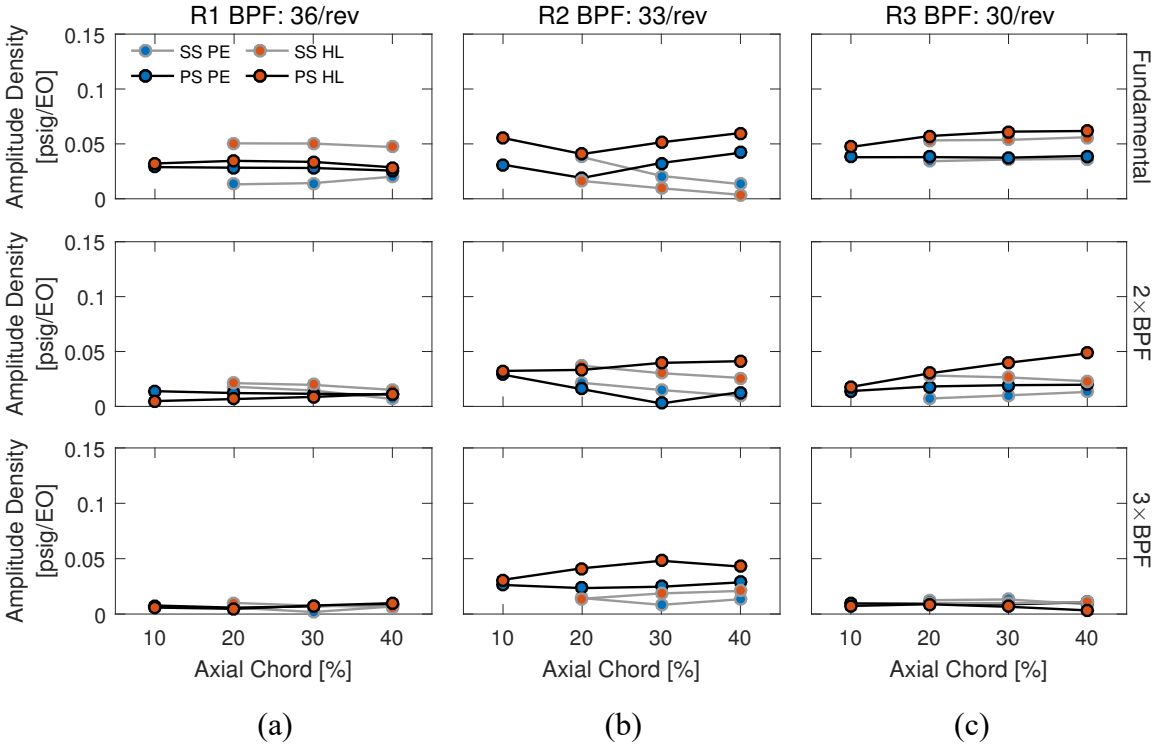


Figure 4.11: Axial variation of amplitude density at 80% span for 38EO-1T.

increased by a factor of 3.8. Response of the fundamental R2 blade-pass frequency has decreased by about 60% between pressure side measurements and 33% to 86% between suction side measurements. Despite large decreases in the fundamental response, the R2 harmonics largely maintain similar amplitude densities, with small decreases on the PE pressure side and suction side amplitudes occurring at the second harmonic and small increases of pressure side and small decreases of suction side spectral magnitudes occurring. Fundamental R3 response is similar between engine order crossings, but the second harmonic shows increase in the HL pressure side measurements of as much as nearly 13 times the 76EO-1CWB response while the HL suction side amplitude density decreases by about 35%. The third harmonic shows little change occurring at different measurement locations and loading conditions, and decreases in amplitude density between 76EO-1CWB and 38EO-1T.

# 5. SUMMARY AND CONCLUSIONS

The objective of this research was to investigate the unsteady aerodynamics of an embedded compressor stage at operating conditions simulating forced response R2 resonant conditions. As a part of this study, the unsteady flow field of R2 was characterized with fast-response pressure transducers installed in the casing endwall and at the rotor exit plane with a radially traversed fast-response pressure transducer embedded in a Kiel-head total pressure probe while the unsteady loading of S2 was studied with a fast-response pressure transducer instrumented stator vane passage. Three engine order crossings associated with forced response excitation were considered when the necessary mechanical speeds were outside of the engine order crossing resonance speeds. Two compressor configurations were studied: a baseline, and a reduced S1 vane count. The 88EO-1CWB crossing was examined for the baseline count and was compared against the 76EO-1CWB and 38EO-1T crossings of the reduced vane count. Full and partial speedlines associated with the engine order crossing speeds (88EO-68%, 76EO-78%, and 38EO-86% corrected speeds) were mapped in preparation for detailed measurements. Data were acquired at two different loading conditions at each speed, peak efficiency and high loading, corresponding with the design point operating line (PE) and an operating line between the design point operating line and the stall line (HL).

## 5.1 Characterization of Unsteady Aerodynamics of the Embedded Stage Rotor

Fast-response pressure transducers flush-mounted in the casing over the embedded stage rotor and at the rotor exit plane were used to capture unsteady pressure measurements in the casing endwall region over the rotor and in the axial spacing between embedded stage rotor and stator. Detailed circumferential traverses performed for each engine order crossing and loading condition, result in high-resolution pressure contours detailing over-rotor tip clearance flows and rotor exit flows for several operating conditions. With these measurements, comprehensive characterization of the tip leakage flow, including its inception, passage trajectory, and roll-up into the tip leakage vortex, was presented. Measurements at higher speeds correlate with higher ensemble average pressures and RMS

pressure unsteadiness. Better relative comparisons of contours at the different engine order crossings could be made through different normalization techniques, for example, instead of inlet area-averaged total pressures normalizing by dynamic pressure based on wheel speed and inlet density would shift contour levels to more similar scales. Pressure contours and leakage vortex trajectory traces show the trajectories at each engine order crossing become steeper with respect to the axial chord and move towards the leading edge as loading is increased. Increased loading corresponds to lower mass flow through the compressor, and a higher incidence entering the blade-row.

Spectral analyses of over-rotor measurements support conclusions from the time-resolved pressures. Near the location of tip leakage vortex inception, the R2 blade-pass frequency is dominant in the spectra and significantly increases with higher loading conditions. The axial variation of the R2 blade-pass frequency shows similar amplitudes occurring nearest the leading edge with maximum amplitudes occurring between the quarter and midchord (25%–50% axial chord). The high loading condition has nearly similar maximum amplitude as the peak efficiency maximum amplitude, but the location of maximum amplitude occurrence is shifted forward towards the leading edge. After the location of maximum amplitude, the amplitude density decreases to its minimum nearest the trailing edge, with each loading condition producing nearly the same magnitude. The spectra variation across vane passage locations results in sinusoidal variation of the amplitude of the R2 blade-pass frequency across the vane passage. Measurements at chosen sensor locations along the axial chord show this sinusoidal variation to occur nearly out-of-phase from one another. The variations in leading edge incidence caused by the upstream vane position are likely the result of these out-of-phase sinusoidal variations. A higher incidence on the leading edge results in a higher amplitude associated with these sensors, while further downstream this same higher incidence will result in lower amplitude.

Tip clearance was also shown to be an important factor in the development of tip leakage flows. Comparing the blade-to-blade variation in RMS pressure unsteadiness contours with R2 blade clearances presents high levels of unsteadiness coinciding with the highest relative blade tip clearance for the HL 88EO flow condition. Regions of lower relative

unsteadiness occur for blades possessing smaller relative tip clearances. Unsteadiness effects attributed to higher tip clearances were not observed in the other flow conditions, but they have been well documented in other similar studies; lower relative unsteadiness was consistently observed corresponding with lower blade clearances. Finally, considering blade-to-blade variation across sequential vane passages, evidence of the impingement and propagation of an upstream vane wake through the rotor passage with varying upstream vane position is evident, and is shown propagating through the embedded rotor row for Blades 7–10 across vane passage positions 40%–30%. The stator wake unsteadiness adds to the unsteadiness of the tip leakage vortex, and an overall higher unsteadiness through the rotor passage is evident.

In addition to the tip leakage vortex, the exit plane total pressure measurements provide high-resolution time-resolved rotor exit flow field measurements detailing the embedded stage rotor wakes and hub corner separation. Mean vane passage results demonstrate a more intense tip leakage vortex corresponds to a less intense hub corner separation. Higher blockage in one region, indicated by higher RMS pressure unsteadiness, allows a higher flowrate into the region of lower blockage. This higher flowrate causes a lower local static pressure and unloading in the region. This is further supported by contour variation across vane passage locations showing modulation in the unsteadiness present in the hub and tip locations, when one location is highly loaded, the other location becomes unloaded. The locations of high unsteadiness occur out-of-phase when comparing different loading conditions of the same engine order crossing. Vane passage locations with higher unsteadiness in the tip region and lower unsteadiness in the hub region at PE loading tend to be reversed at HL conditions. The Rotor 1 wake propagating downstream is also apparent in the exit plane contours, and shows up as a band of unsteadiness connecting the hub suction side to the tip pressure side of the rotor passage at locations distributed every one-third of the annulus.

Spectral analyses performed on the mean vane passage at discrete radial positions reflecting the tip region, midspan, and hub region show greater variation in the frequency content of the exit plane when compared to the over-rotor casing measurements. Near the

blade tip, frequency content of the signal is more heavily influenced by the R2 blade-pass frequency. Midspan frequency content shows a much lower amplitude spectrum, with similar amplitudes occurring for fundamental and harmonics of the R2 blade-pass frequency. Near the hub, fundamental and higher harmonics of the R2 blade-pass frequency are nearly the same magnitude, but increase from midspan.

Blade-to-blade variation in mean vane passage locations shows the prevalent 3/rev modulation associated with this machine, present from the difference in rotor blade-counts. Additionally, quite different flow phenomena can be observed associated with the individual blades of R2. A similar comparison to the over-rotor measurements of Blades 7–10 across vane passage positions shows the modulation of unsteadiness around the annulus of the compressor.

## 5.2 Characterizing Unsteady Loading of Embedded Stage Stator

High-frequency response pressure transducers flush embedded in a stator vane passage were used to measure unsteady surface pressures on the embedded stage vane-row originating from the upstream rotor. These measurements were performed for all engine order crossings and loading conditions. Normalization by dynamic pressure using wheel speed and inlet density yields a surface pressure coefficient allowing for better comparison between engine order crossings despite relatively large differences in compressor speed. Several metrics were proposed to analyze the surface pressure coefficients. The surface pressure coefficient traces show the 3/rev modulation characteristic of this compressor. These modulations also exist in the range of the surface pressure coefficient for each blade-pass period and the normalized average surface pressure coefficients. Splitting the ensemble average surface pressure coefficient trace into three parts of eleven blades each shows the repeatable nature of the measured surface pressures generated from the upstream rotor. This repeatability is important, allowing a smaller computational domain to be used capture the upstream forcing function from the embedded rotor and resulting unsteady vane passage surface pressures. The RMS unsteadiness results showed sinusoidal peaks near the leading edge of all measurement conditions and a settling of unsteadiness towards the

midchord. The peaks near the leading edge are indicative of rotor wakes and tip leakage flows impinging on the stator vane passage.

A spectral analysis of the ensemble average pressures showed a more broadband response than the previous measurement techniques. The 88EO crossing has a dominant fundamental R2 blade-pass frequency response, with smaller responses associated with Rotors 1 and 3 blade-pass frequencies. Higher order spectral magnitudes are quite low beyond the second harmonic of fundamental frequencies. The reduced vane count spectra were much more complex. While the R2 blade-pass frequency is typically dominant on the pressure side locations, the suction side location shows Rotors 1 and 3 to have higher amplitude responses. Frequency content in the higher engine orders has a much greater amplitude, and is sometimes larger than the fundamental frequency response. For some spectra, the R2 blade-pass frequency is nearly non-existent when compared with surrounding frequency bands. The emergence of two non-blade-pass frequencies, the 63EO and 96EO, is typically evident for HL loading condition. These engine orders, comprising the second and third harmonics of fundamental rotor blade-pass frequencies and multiples of the 3/rev from the difference in blade counts have very high amplitudes relative to their local cluster of frequency bands. The reduced vane count, designed and manufactured to disrupt the 44EO and 88EO forcing functions from the Stator 1 vane-row, has also greatly mitigated the amplitudes associated with the fundamental blade-pass frequencies of the rotor-rows through redistribution of amplitudes to nearby and higher order engine order bands.

## 5.3 Conclusions from High-Frequency Response Pressure Measurements

This investigation has established variations in flow-fields associated with blade-row interactions need to be considered throughout the design and operation of compressor technologies. The average flow characteristics used in computational fluid dynamics cannot capture the effects of these variations and their effects on blade-row interactions if they are not modeled. Previous work with the reduced vane count configuration has shown promise in the reduction of vibration associated with the 88EO-1CWB crossing through redistribution of energy to surrounding engine orders (Aye-Addo, 2016), there appears to

be an additional, similar, benefit in the reduction of the frequency response associated with the rotors, namely the embedded stage R2.

## 5.4 Recommendations for Future Research

With lessons learned over the duration of this investigation, the volume of collected data over the duration of this study could provide significant amount of further work to be addressed before the research potential of the dataset is exhausted. All data presented in this work was acquired at steady-state operating points, but additional data for many of the instrumentation setups were acquired during transient compressor speed sweeps, both acceleration and deceleration of the compressor through engine order crossings. Building upon methods developed and presented by Murray et al. (2015), it is possible to detect the vibration of the rotors using stationary pressure transducers. The further development of this method is interesting, as it could allow a robust and potentially easier solution for blade vibration and health monitoring than many of the popular methods in use, i.e. NSMS and strain gages. Additional aerodynamic phenomena captured in an unsteady operating environment may be studied through the acquired sweep data, including the evolution of the tip leakage vortex, rotor wakes, and hub corner separations as compressor speed is changing. To study these elements of the flow, some challenges in processing techniques would need to be overcome to handle the transient speed of the machine.

Further methods used to monitor non-synchronous flutter vibration with circumferential stationary pressure transducers located in the casing (Kurkov & Dicus, 1978; Kurkov, 1981, Gill and Capece, 2004) were presented. Interesting research could be performed with existing hardware and instrumentation to detect blade vibration of the research compressor under investigation in this study. The compressor casing has six circumferential ports located just upstream of the leading edge of each rotor row. This instrumentation has been used to study stall inception of the machine, but these ports can easily be used to investigate techniques the detection of synchronous rotor vibration caused by forced response resonant conditions.

Measurements with the single-element fast-response pressure probe can be used to identify regions of high RMS pressure unsteadiness with respect to the phase-locked ensemble average at the rotor exit plane. If coupled with velocity measurements acquired with thermal anemometry, regions of velocity deficit and generated blockage can be calculated. Robust methods for the quantification of blockage and associated losses are important for the overall aerodynamic performance of a turbomachine, and have been shown to be an area of active research. Comparing flow angles entering and exiting blade-rows measured with pneumatic probes or thermal anemometry would be useful to compare with all unsteady pressure measurements presented.

Lastly, all research techniques would benefit from data acquired through stator vane clocking and the reconciliation of all measurement positions relative to one another. Individually circumferential indexing of each vane-row allows vanes to be moved relative to each other. This technique would be especially useful for the instrumented vane passage, as when this passage is installed the vane-row needs to be fixed. Moving upstream vane-rows relative to the fixed instrumented vane-row can provide further characterization of the blade-row interaction of rotors and stators. The instrumented vane passage measurements of this study were acquired in a fixed vane configuration and further conclusions could be made with vane clocking techniques. Several circumferential measurement locations were utilized during the acquisition of the dataset. Effort has been made, where possible, to compare phase shifted data so flow trends dependent on vane position can be properly studied. Future efforts could be applied to reconciling relative circumferential positions of the existing data set, or, if necessary, reacquiring data of particular interest.

# REFERENCES

Aye-Addo, P. A. N. (2016). *An Experimental Study of the Effects of Vane Count and Non-Uniform Vane Spacing on Rotor Resonant Response* (Master's Thesis). Purdue University.

Baumgartner, M., Kameier, F., & Hourmouziadis, J. (1995). Non-Engine Order Blade Vibration in a High Pressure Compressor. In *Twelfth International Symposium on Airbreathing Engines*. Melbourne, Australia. Retrieved from https://hal.archives-ouvertes.fr/hal-01353829

Berdanier, R. A. (2015). *An Experimental Characterization of Tip Leakage Flows and Corresponding Effects on Multistage Compressor Performance* (PhD Dissertation). Purdue University, West Lafayette, Indiana.

Berdanier, R. A., & Key, N. L. (2015). *An Experimental Investigation of the Flow Physics Associated With End Wall Losses and Large Rotor Tip Clearances as Found in the Rear Stages of a High Pressure Compressor*. Retrieved from https://ntrs.nasa.gov/search.jsp?R=20150021045

Berdanier, R. A., Smith, N. R., Fabian, J. C., & Key, N. L. (2014). Humidity Effects on Experimental Compressor Performance—Corrected Conditions for Real Gases. *Journal of Turbomachinery*, *137*(3), 031011-031011-10. https://doi.org/10.1115/1.4028356

Boyd, D. M., & Fleeter, S. (2003). Axial Compressor Blade-to-Blade Unsteady Aerodynamic Variability. *Journal of Propulsion and Power*, *19*(2), 242–249. https://doi.org/10.2514/2.6105

Brossman, J. R. (2012). *An Investigation of Rotor Tip Leakage Flows in the Rear-Block of a Multistage Compressor* (PhD Dissertation). Purdue University, West Lafayette, Indiana.

Capece, V. R., Manwaring, S. R., & Fleeter, S. (1986). Unsteady Blade Row Interactions in a Multistage Compressor. *Journal of Propulsion and Power*, *2*(2), 168–174. https://doi.org/10.2514/3.22862

Chen, G. T., Greitzer, E. M., Tan, C. S., & Marble, F. E. (1991). Similarity Analysis of Compressor Tip Clearance Flow Structure. *Journal of Turbomachinery*, *113*(2), 260–269. https://doi.org/10.1115/1.2929098

Dong, Y., Gallimore, S. J., & Hodson, H. P. (1987). Three-Dimensional Flows and Loss Reduction in Axial Compressors. *Journal of Turbomachinery*, *109*(3), 354–361. https://doi.org/10.1115/1.3262113

Ernst, M., Michel, A., & Jeschke, P. (2010). Analysis of Rotor-Stator-Interaction and Blade-to-Blade Measurements in a Two Stage Axial Flow Compressor. *Journal of Turbomachinery*, *133*(1), 011027-011027-12. https://doi.org/10.1115/1.4001168

Feiereisen, J., & Fleeter, S. (1994). Linear Theory Unsteady Aerodynamics - Stator Row Response to Combined Vortical/Potential Forcing Functions. In *30th Joint Propulsion Conference and Exhibit*. American Institute of Aeronautics and Astronautics. https://doi.org/10.2514/6.1994-2974

Feiereisen, J. M., Montgomery, M. D., & Fleeter, S. (1994). Unsteady Aerodynamic Forcing Functions: A Comparison Between Linear Theory and Experiment. *Journal of Turbomachinery*, *116*(4), 676–685. https://doi.org/10.1115/1.2929460

Gallus, H. E., Grollius, H., & Lambertz, J. (1982). The Influence of Blade Number Ratio and Blade Row Spacing on Axial-Flow Compressor Stator Blade Dynamic Load and Stage Sound Pressure Level. *Journal of Engineering for Power*, *104*(3), 633–641. https://doi.org/10.1115/1.3227326

Gbadebo, S. A., Cumpsty, N. A., & Hynes, T. P. (2006). Interaction of Tip Clearance Flow and Three-Dimensional Separations in Axial Compressors. *Journal of Turbomachinery*, *129*(4), 679–685. https://doi.org/10.1115/1.2720876

Gill, J. D., & Capece, V. R. (2004). Experimental Investigation of Flutter in a Single Stage Unshrouded Axial-Flow Fan. In *42nd AIAA Aerospace Sciences Meeting and Exhibit*. American Institute of Aeronautics and Astronautics. https://doi.org/10.2514/6.2004-686

Griffin, O. M. (1972). Flow Near Self-Excited and Forced Vibrating Circular Cylinders. *Journal of Engineering for Industry*, *94*(2), 539–547. https://doi.org/10.1115/1.3428187

Hah, C., & Shin, H.-W. (2012). Study of Near-Stall Flow Behavior in a Modern Transonic Fan With Compound Sweep. *Journal of Fluids Engineering*, *134*(7), 071101-071101-7. https://doi.org/10.1115/1.4006878

Hall, K. C., & Verdon, J. M. (1991). Gust Response Analysis for Cascades Operating in Nonuniform Mean Flows. *AIAA Journal*, *29*(9), 1463–1471. https://doi.org/10.2514/3.10761

Hardigg, G. W. (1951, November 20). *US2575710 A*. Retrieved from http://www.google.com/patents/US2575710

Henderson, G. H., & Fleeter, S. (1993). Forcing Function Effects on Unsteady Aerodynamic Gust Response: Part 1—Forcing Functions. *Journal of Turbomachinery*, *115*(4), 741–750. https://doi.org/10.1115/1.2929309

Henderson, G. H., & Fleeter, S. (1993). Forcing Function Effects on Unsteady Aerodynamic Gust Response: Part 2—Low Solidity Airfoil Row Response, V005T14A027. https://doi.org/10.1115/92-GT-175

Inoue, M., & Kuroumaru, M. (1989). Structure of Tip Clearance Flow in an Isolated Axial Compressor Rotor. *Journal of Turbomachinery*, *111*(3), 250–256. https://doi.org/10.1115/1.3262263

Inoue, M., Kuroumaru, M., & Fukuhara, M. (1986). Behavior of Tip Leakage Flow Behind an Axial Compressor Rotor. *Journal of Engineering for Gas Turbines and Power*, *108*(1), 7–14. https://doi.org/10.1115/1.3239889

Johnston, R. T., Feiereisen, J. M., & Fleeter, S. (1998). Measured Rotor Wake and Potential Forcing Functions, Including Blade Row Interactions. *Journal of Propulsion and Power*, *14*(2), 191–198. https://doi.org/10.2514/2.5285

Kadambi, J. R., Quinn, R. D., & Adams, M. L. (1989). Turbomachinery Blade Vibration and Dynamic Stress Measurements Utilizing Nonintrusive Techniques. *Journal of Turbomachinery*, *111*(4), 468–474. https://doi.org/10.1115/1.3262295

Kemp, N. H. (1955). The Unsteady Forces Due to Viscous Wakes in Turbomachines. *Journal of the Aeronautical Sciences*, *22*(7), 478–483. https://doi.org/10.2514/8.3376

Kerrebrock, J. L., & Mikolajczak, A. A. (1970). Intra-Stator Transport of Rotor Wakes and Its Effect on Compressor Performance. *Journal of Engineering for Power*, *92*(4), 359–368. https://doi.org/10.1115/1.3445365

Key, N. L., Lawless, P. B., & Fleeter, S. (2009a). An Experimental Study of Vane Clocking Effects on Embedded Compressor Stage Performance. *Journal of Turbomachinery*, *132*(1), 011018-011018-10. https://doi.org/10.1115/1.3072714

Key, N. L., Lawless, P. B., & Fleeter, S. (2009b). Vane Clocking in a Three-Stage Compressor: Frequency Domain Data Analysis. *Journal of Propulsion and Power*, *25*(5), 1100–1107. https://doi.org/10.2514/1.43423

Key, N. L., Lawless, P. B., & Fleeter, S. (2010). Rotor Wake Variability in a Multistage Compressor. *Journal of Propulsion and Power*, *26*(2), 344–352. https://doi.org/10.2514/1.45715

Khalid, S. A., Khalsa, A. S., Waitz, I. A., Tan, C. S., Greitzer, E. M., Cumpsty, N. A., Marble, F. E. (1999). Endwall Blockage in Axial Compressors. *Journal of Turbomachinery*, *121*(3), 499–509. https://doi.org/10.1115/1.2841344

Khalsa, A. S. (1996). Endwall Blockage in Axial Compressors (PhD Dissertation). Massachusetts Institute of Technology, Cambridge, Maryland.

Koch, C. C., & Smith, J., L. H. (1976). Loss Sources and Magnitudes in Axial-Flow Compressors. *Journal of Engineering for Power*, *98*(3), 411–424. https://doi.org/10.1115/1.3446202

Koch, P., & Wolff, J. (1998). Vortical Forcing Function Variations with Axial Spacing and Blade Count. In *34th AIAA/ASME/SAE/ASEE Joint Propulsion Conference and Exhibit*. American Institute of Aeronautics and Astronautics. https://doi.org/10.2514/6.1998-3434

Kurkov, A., & Dicus, J. (1978). Synthesis of Blade Flutter Vibratory Patterns Using Stationary Transducers, V01BT02A059. https://doi.org/10.1115/78-GT-160

Kurkov, A. P. (1981). Flutter Spectral Measurements Using Stationary Pressure Transducers. *Journal of Engineering for Power*, *103*(2), 461–467. https://doi.org/10.1115/1.3230743

Lakshminarayana, B. (1970). Methods of Predicting the Tip Clearance Effects in Axial Flow Turbomachinery. *Journal of Basic Engineering*, *92*(3), 467–480. https://doi.org/10.1115/1.3425036

Lakshminarayana, B., & Horlock, J. H. (1965). Leakage and Secondary Flows in Cascades.

Lakshminarayana, B., Pouagare, M., & Davino, R. (1982). Three-Dimensional Flow Field in the Tip Region of a Compressor Rotor Passage—Part I: Mean Velocity Profiles and Annulus Wall Boundary Layer. *Journal of Engineering for Power*, *104*(4), 760–771. https://doi.org/10.1115/1.3227342

Lefcort, M. D. (1965). An Investigation Into Unsteady Blade Forces in Turbomachines. *Journal of Engineering for Power*, *87*(4), 345–354. https://doi.org/10.1115/1.3678275

Mailach, R., Lehmann, I., & Vogeler, K. (2008). Periodical Unsteady Flow Within a Rotor Blade Row of an Axial Compressor—Part II: Wake-Tip Clearance Vortex Interaction. *Journal of Turbomachinery*, *130*(4), 041005-041005-10. https://doi.org/10.1115/1.2812330

Manwaring, S. R., Rabe, D. C., Lorence, C. B., & Wadia, A. R. (1997). Inlet Distortion Generated Forced Response of a Low-Aspect-Ratio Transonic Fan. *Journal of Turbomachinery*, *119*(4), 665–676. https://doi.org/10.1115/1.2841176

Manwaring, S. R., & Wisler, D. C. (1993). Unsteady Aerodynamics and Gust Response in Compressors and Turbines. *Journal of Turbomachinery*, *115*(4), 724–740. https://doi.org/10.1115/1.2929308

McDougall, N. M., Cumpsty, N. A., & Hynes, T. P. (1990). Stall Inception in Axial Compressors. *Journal of Turbomachinery*, *112*(1), 116–123. https://doi.org/10.1115/1.2927406

Mengle, V. (1990). Acoustic Spectra and Detection of Vibrating Rotor Blades, Including Row-to-Row Interference. In *13th Aeroacoustics Conference*. American Institute of Aeronautics and Astronautics. https://doi.org/10.2514/6.1990-3987

Meyer, R. X. (1958). The Effect of Wakes on the Transient Pressure and Velocity Distributions in Turbomachines. *Transactions of the American Society of Mechanical Engineers*, *Vol. 80*, 1544–1552.

Müller, D., Sheard, A. G., Mozumdar, S., & Johann, E. (1997). Capacitive Measurement of Compressor and Turbine Blade Tip to Casing Running Clearance. *Journal of Engineering for Gas Turbines and Power*, *119*(4), 877–884. https://doi.org/10.1115/1.2817068

Murray III, W. L. (2014). *Experimental Investigation of a Forced Response Condition in a Multistage Compressor* (Master's Thesis). Purdue University, West Lafayette, Indiana.

Murray III, W. L., & Key, N. L. (2015a). Detection of Rotor Forced Response Vibrations Using Stationary Pressure Transducers in a Multistage Axial Compressor. In *International Journal of Rotating Machinery*. https://doi.org/10.1155/2015/198534

Murray III, W. L., & Key, N. L. (2015b). Experimental Investigation of a Forced-Response Condition in a Multistage Compressor. *Journal of Propulsion and Power*, *31*(5), 1320–1329. https://doi.org/10.2514/1.B35525

Platzer, M. F., & Carta, F. O. (1987). *AGARD Manual on Aeroelasticity in Axial-Flow Turbomachines: Unsteady Turbomachinery Aerodynamics*. North Atlantic Treaty Organization, Advisory Group for Aerospace Research and Development.

Sanders, A. J., & Fleeter, S. (2001). Multi-Blade Row Interactions in a Transonic Axial Compressor: Part II — Rotor Wake Forcing Function and Stator Unsteady Aerodynamic Response, V004T03A033. https://doi.org/10.1115/2001-GT-0269

Sanders, A. J., & Fleeter, S. (2002). Rotor Blade-to-Blade Wake Variability and Effect on Downstream Vane Response. *Journal of Propulsion and Power*, *18*(2), 456–464. https://doi.org/10.2514/2.5956

Shin, H.-W., Solomon, W., & Wadia, A. (2008). Transonic Fan Tip-Flow Features Revealed by High Frequency Response Over-Tip Pressure Measurements, 193–201. https://doi.org/10.1115/GT2008-50279

Sirakov, B. T., & Tan, C.-S. (2003). Effect of Unsteady Stator Wake—Rotor Double-Leakage Tip Clearance Flow Interaction on Time-Average Compressor Performance. Journal of Turbomachinery, 125(3), 465–474. https://doi.org/10.1115/1.1574822

Smith, N. R., & Key, N. L. (2017). Blade-Row Interaction Effects on Unsteady Stator Loading in an Embedded Compressor Stage. *Journal of Propulsion and Power*, *33*(1), 248–255. https://doi.org/10.2514/1.B35981

Smith, N. R., Murray III, W. L., & Key, N. L. (2015). Considerations for Measuring Compressor Aerodynamic Excitations Including Rotor Wakes and Tip Leakage Flows. *Journal of Turbomachinery*, *138*(3), 031008-031008-9. https://doi.org/10.1115/1.4032006

Storer, J. A., & Cumpsty, N. A. (1991). Tip Leakage Flow in Axial Compressors. *Journal of Turbomachinery*, *113*(2), 252–259. https://doi.org/10.1115/1.2929095

Storer, J. A., & Cumpsty, N. A. (1994). An Approximate Analysis and Prediction Method for Tip Clearance Loss in Axial Compressors. *Journal of Turbomachinery*, *116*(4), 648–656. https://doi.org/10.1115/1.2929457

Suder, K. L. (1998). Blockage Development in a Transonic, Axial Compressor Rotor. *Journal of Turbomachinery*, *120*(3), 465–476. https://doi.org/10.1115/1.2841741

Weaver, M. M., & Fleeter, S. (1994). Turbine Rotor Generated Forcing Functions for Flow Induced Vibrations, V001T01A107. https://doi.org/10.1115/94-GT-328

Wisler, D. C. (1985). Loss Reduction in Axial-Flow Compressors Through Low-Speed Model Testing. *Journal of Engineering for Gas Turbines and Power*, *107*(2), 354–363. https://doi.org/10.1115/1.3239730

Zhong, J., Han, S., Lu, H., & Kan, X. (2013). Effect of Tip Geometry and Tip Clearance on Aerodynamic Performance of a Linear Compressor Cascade. *Chinese Journal of Aeronautics*, *26*(3), 583–593. https://doi.org/10.1016/j.cja.2013.04.020

# APPENDIX A. OVER-ROTOR CONTOURS OF S1 REDUCED VANE-COUNT CONFIGURATION

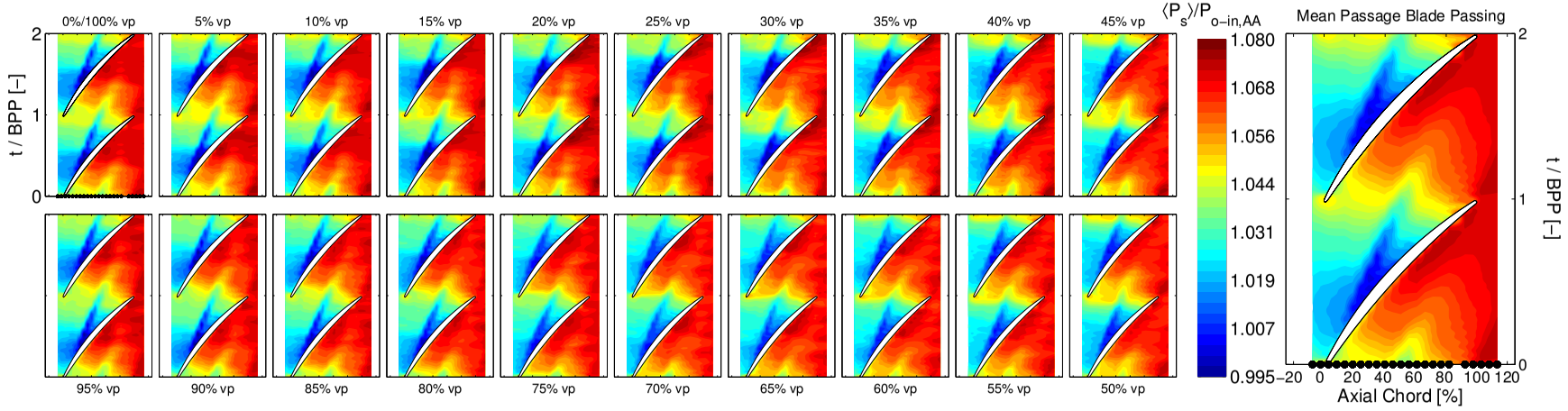


Figure A.1: Mean blade-pass periods of ensemble average static pressures comprising the PE 76EO-1CWB flow condition.

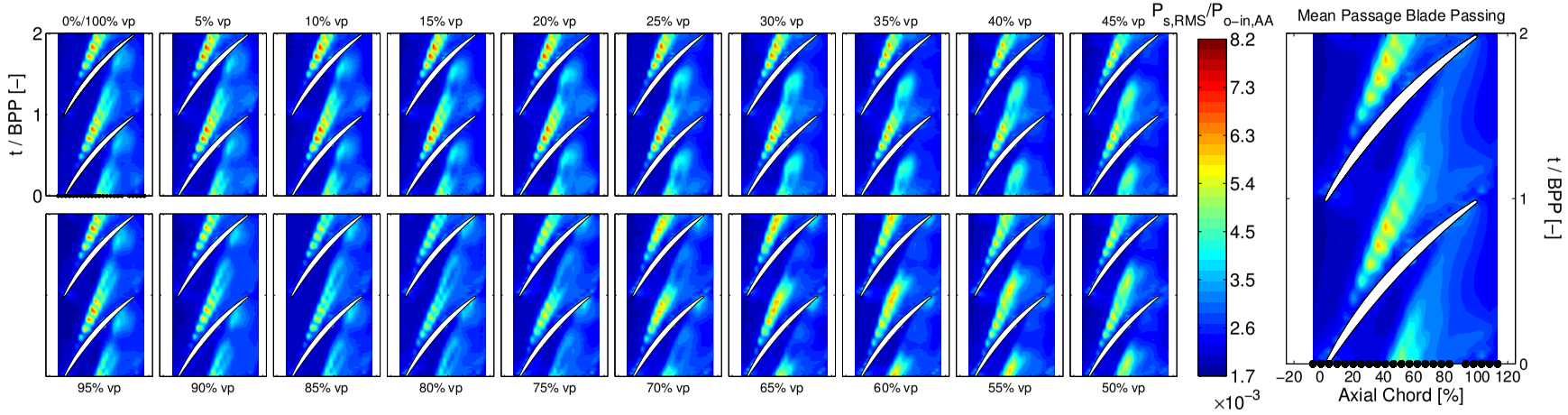


Figure A.2: Mean blade-pass periods of ensemble RMS static pressures comprising the PE 76EO-1CWB flow condition.

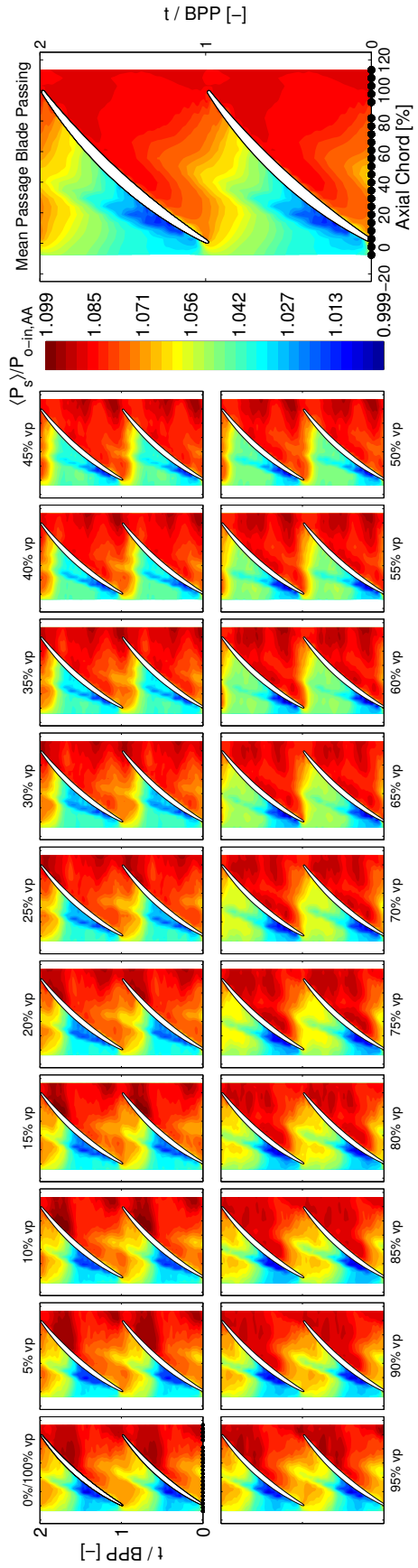


Figure A.3: Mean blade-pass periods of ensemble average static pressures comprising the HL 76EO-1CWB flow condition.

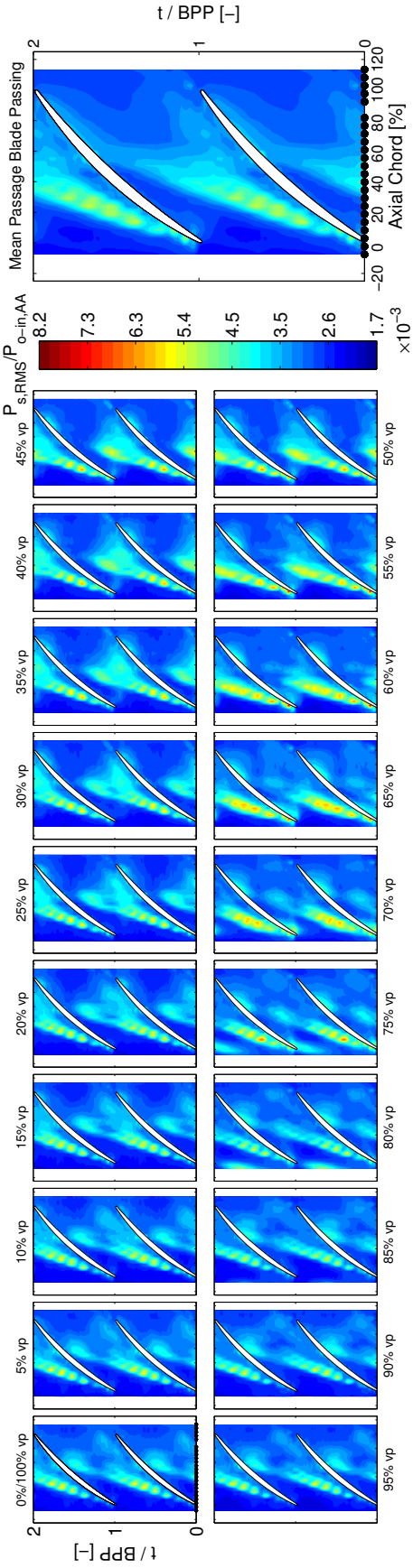


Figure A.4: Mean blade-pass periods of ensemble RMS static pressures comprising the HL 76EO-1CWB flow condition.

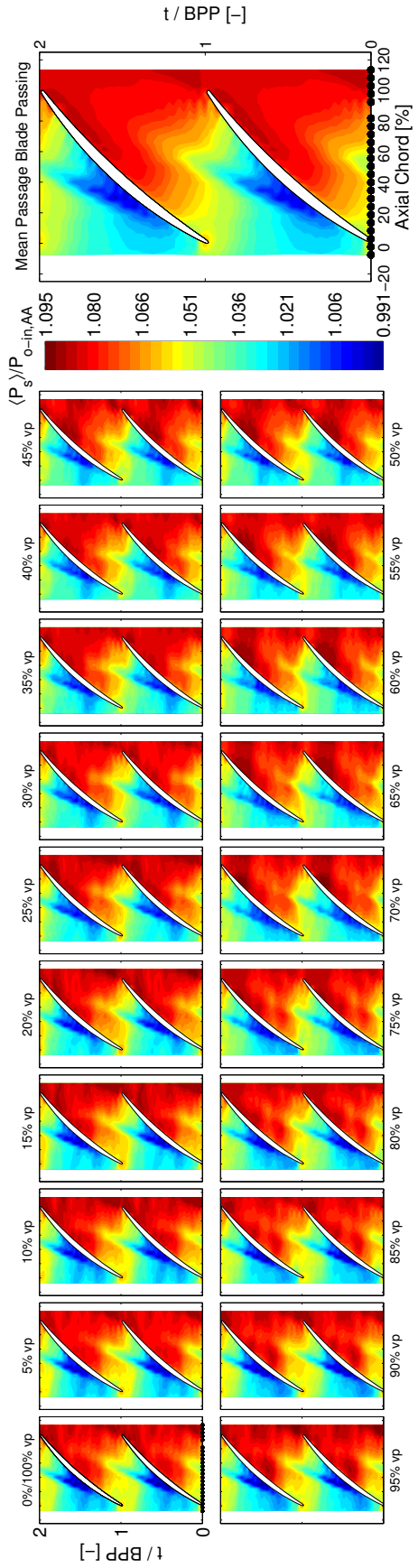


Figure A.5: Mean blade-pass periods of ensemble average static pressures comprising the PE 38EO-1T flow condition.

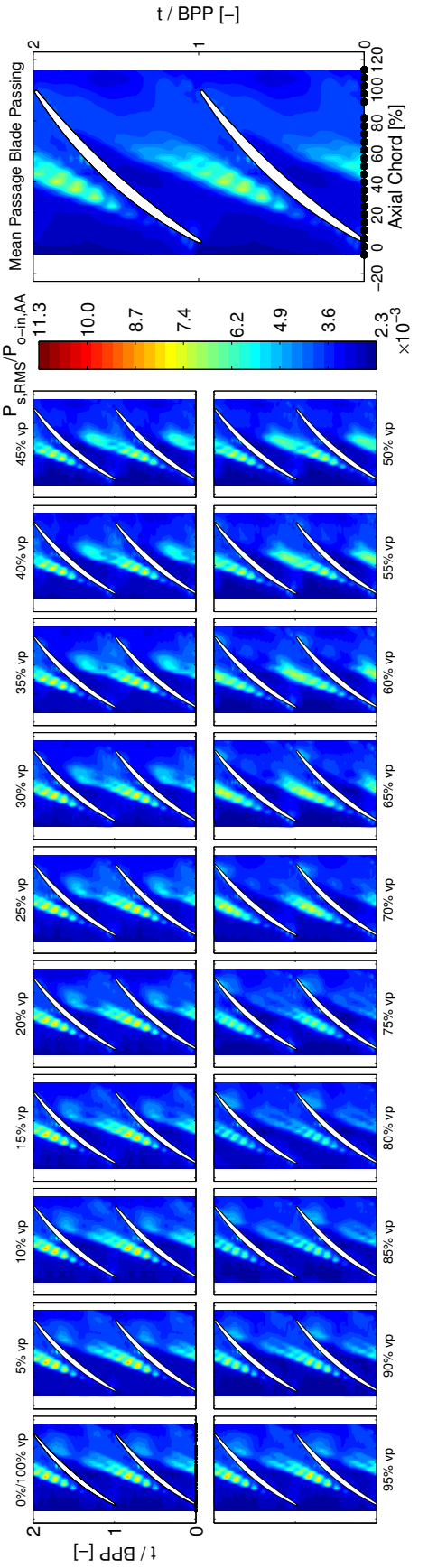


Figure A.6: Mean blade-pass periods of ensemble RMS static pressures comprising the PE 38EO-1T flow condition.

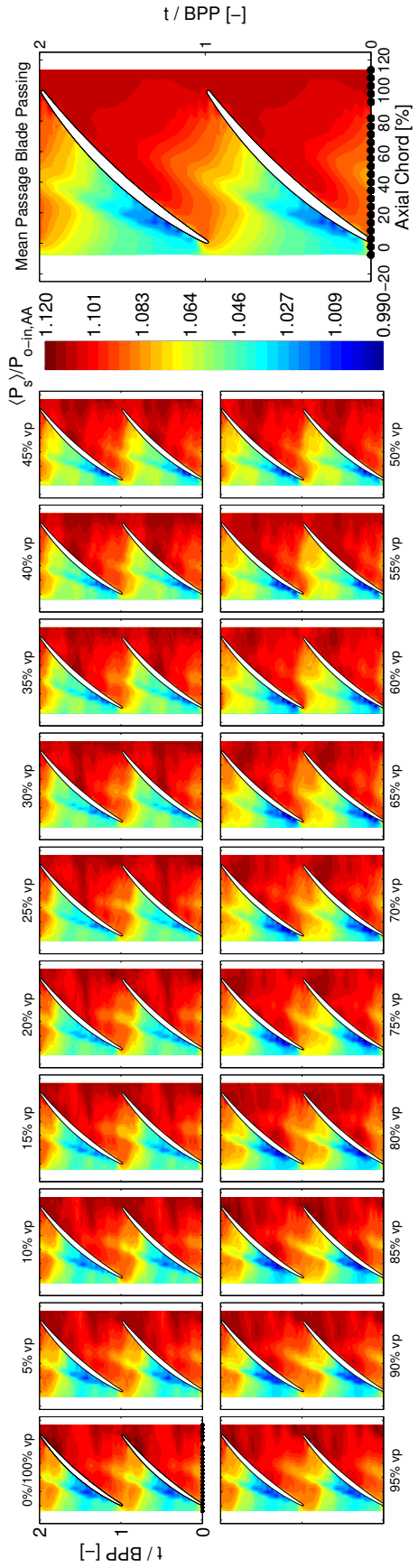


Figure A.7: Mean blade-pass periods of ensemble average static pressures comprising the HL 38EO-1T flow condition.

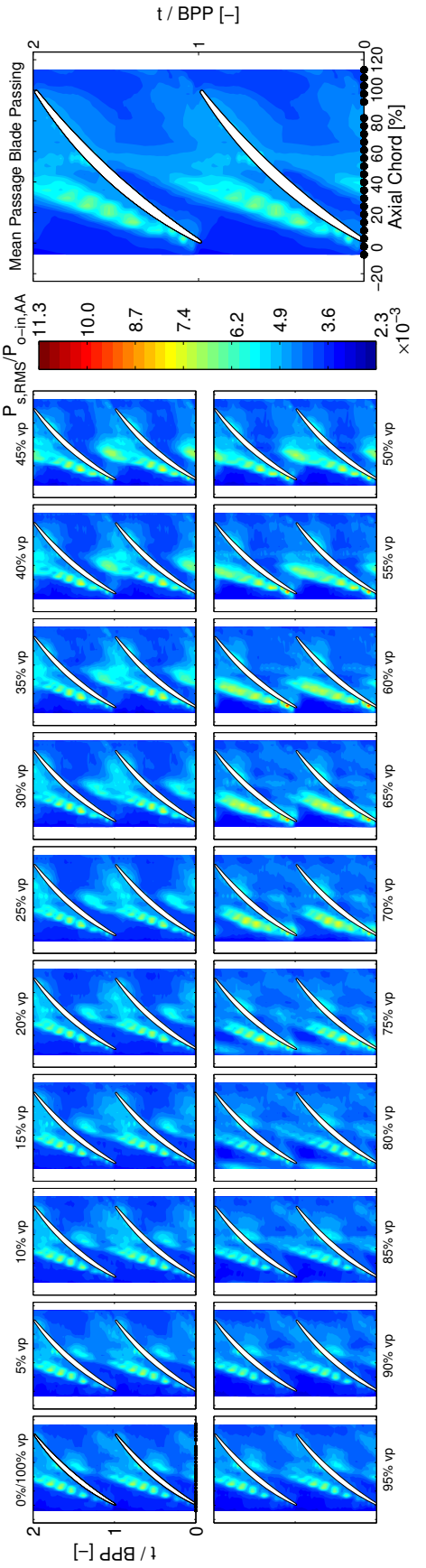


Figure A.8: Mean blade-pass periods of ensemble RMS static pressures comprising the HL 88EO-1T flow condition.

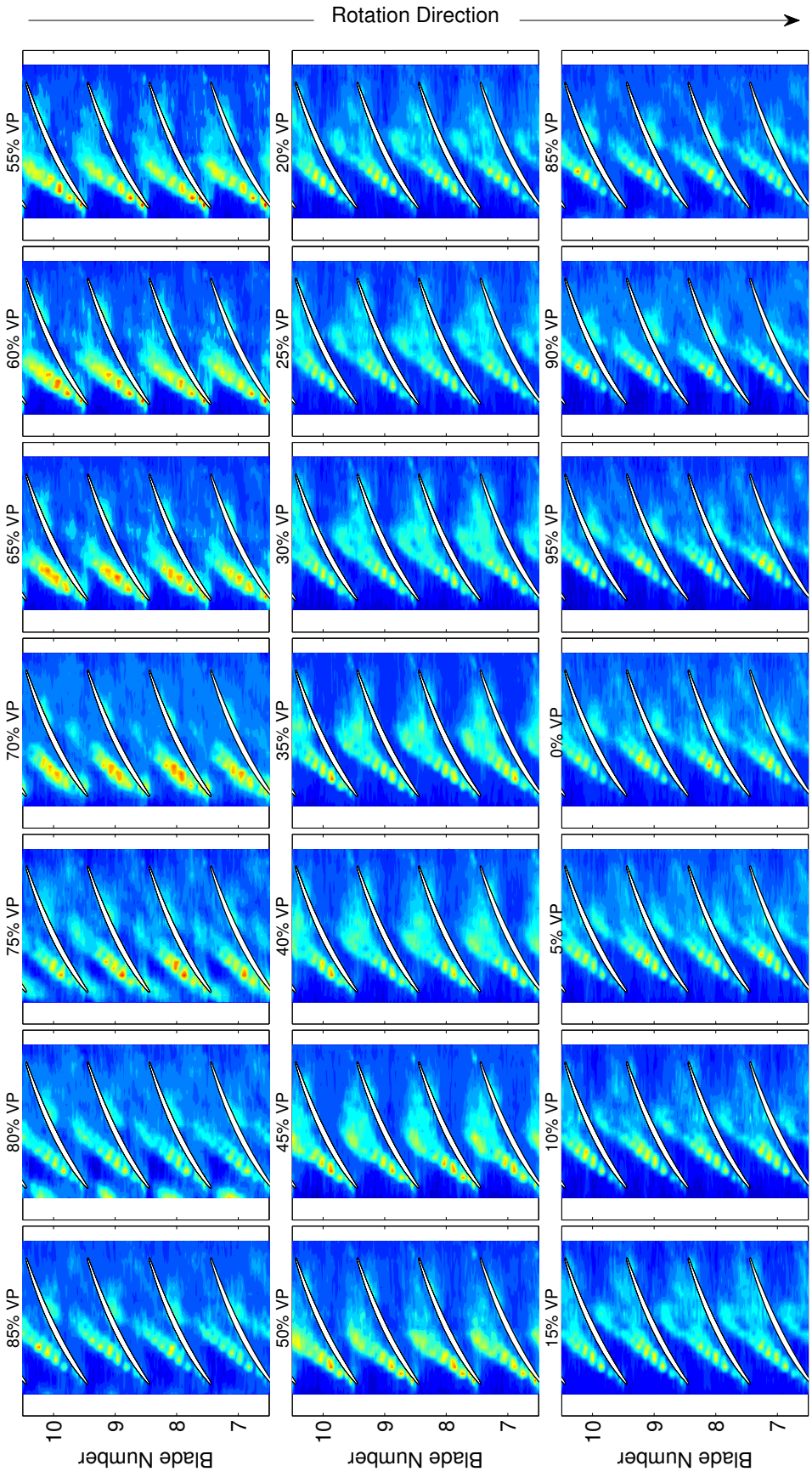


Figure A.9: Full vane passage of over-rotor static pressure measurements of 76EO-1CWB HL flow condition.

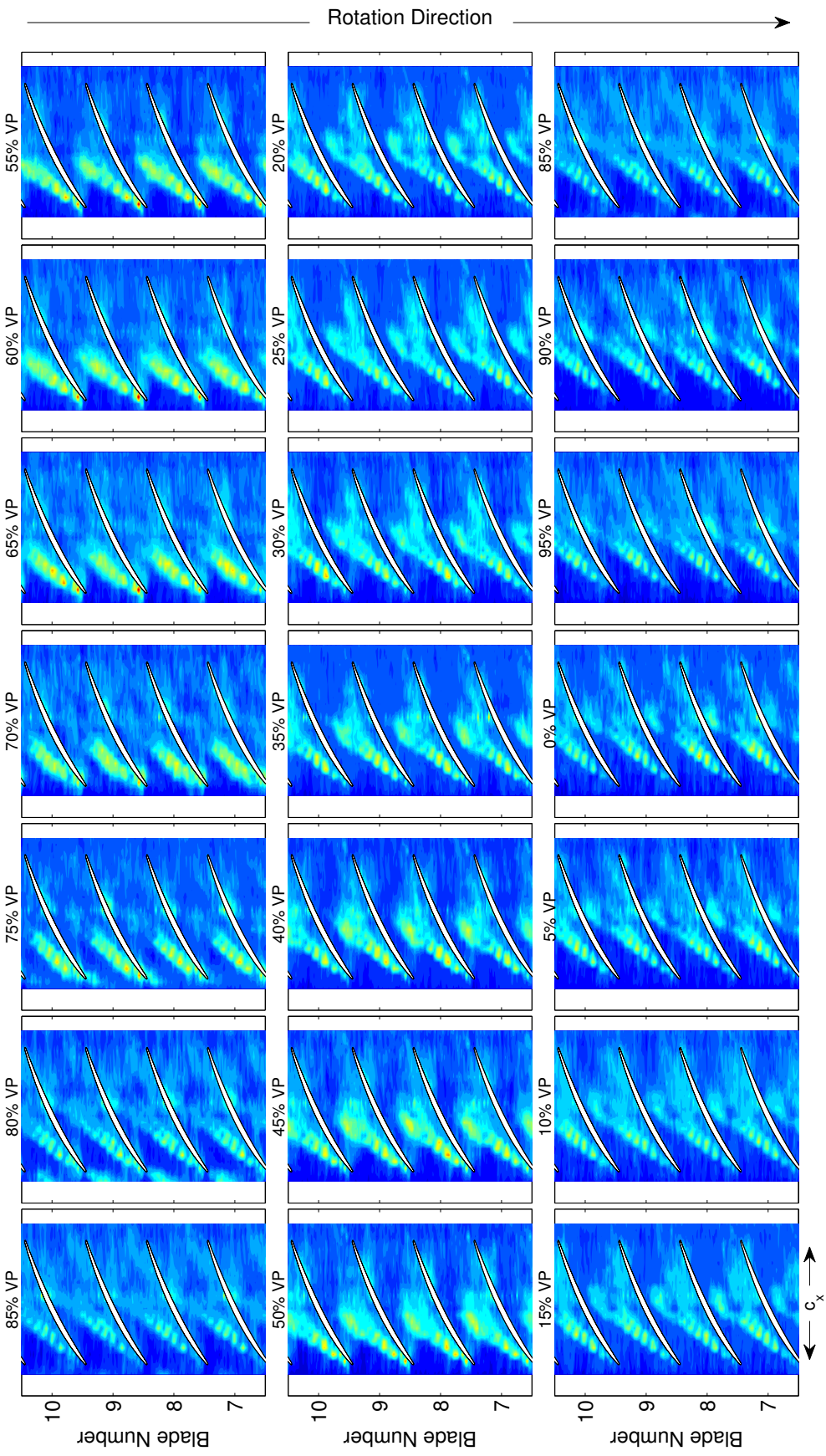


Figure A.10: Full vane passage of over-rotor static pressure measurements of 38EO-1T HL flow condition.

# APPENDIX B. EXIT PLANE CONTOURS OF REDUCED S1 VANE-COUNT CONFIGURATION

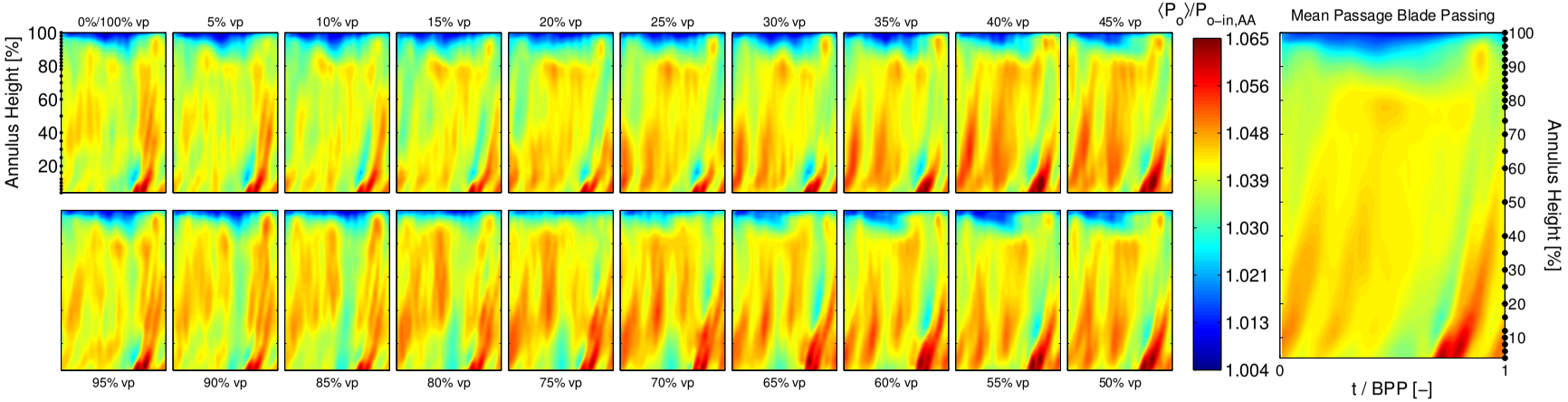


Figure B.1: Mean blade-pass periods of ensemble average total pressures of the PE 38EO-1T flow condition rotor exit plane.

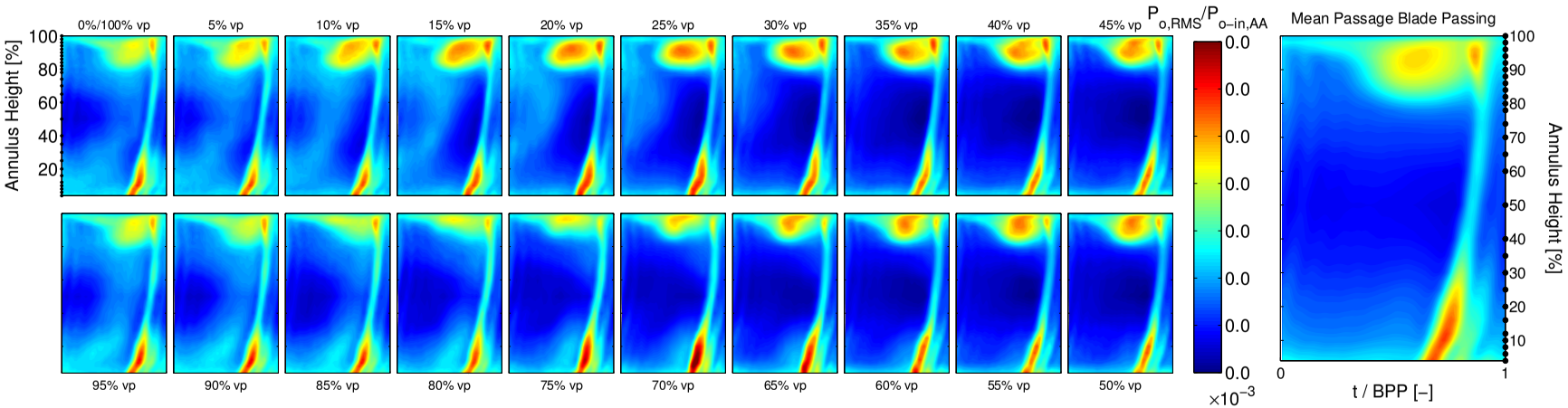


Figure B.2: Mean blade-pass periods of ensemble RMS total pressures of the PE 38EO-1T flow condition rotor exit plane.

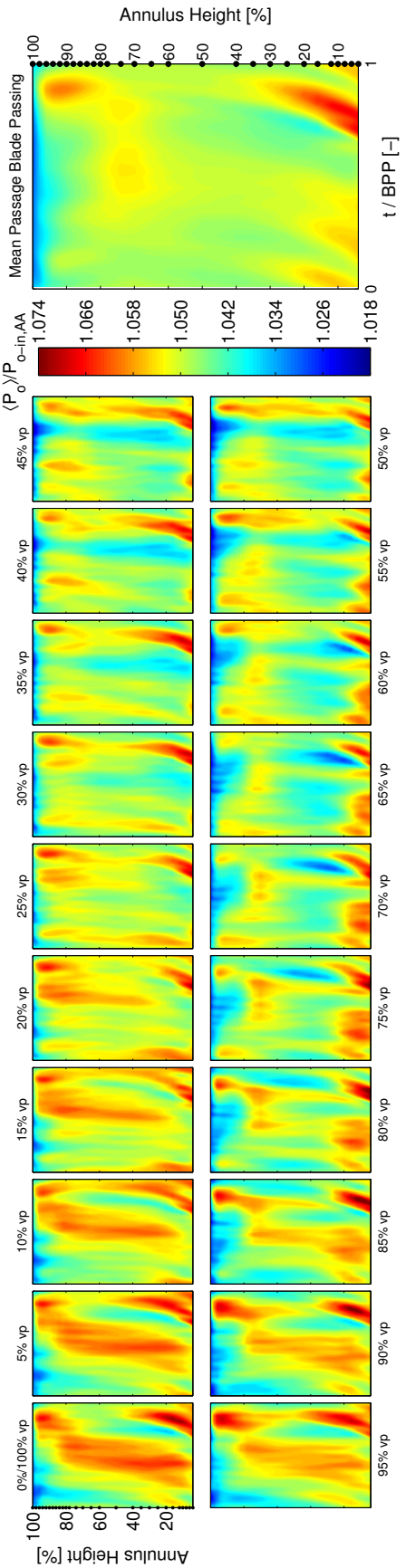


Figure B.3: Mean blade-pass periods of ensemble average total pressures of the HL 38EO-1T flow condition rotor exit plane.

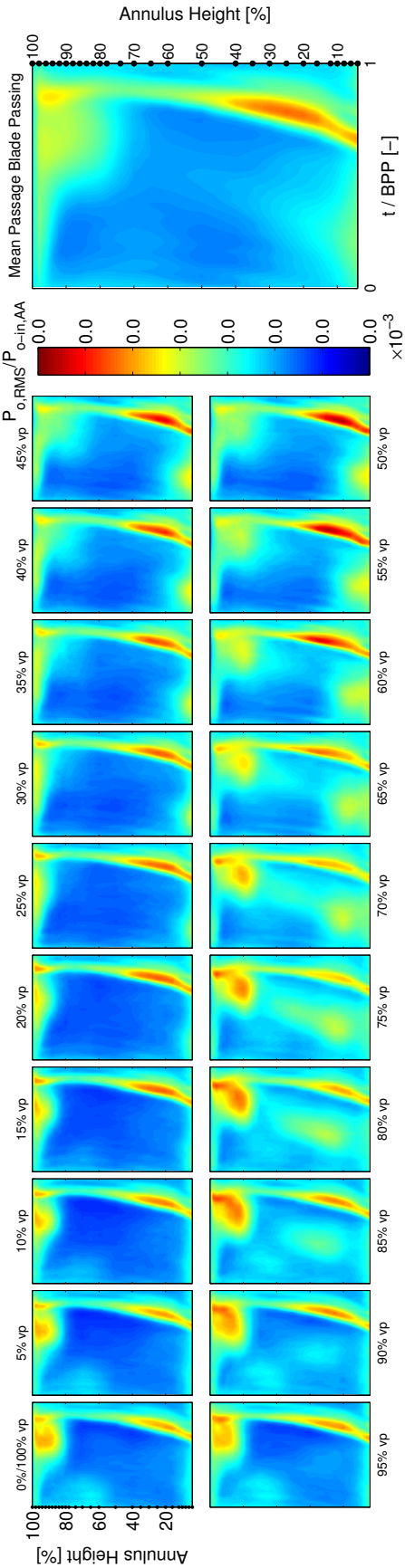


Figure B.4: Mean blade-pass periods of ensemble RMS total pressures of the HL 38EO-1T flow condition rotor exit plane.

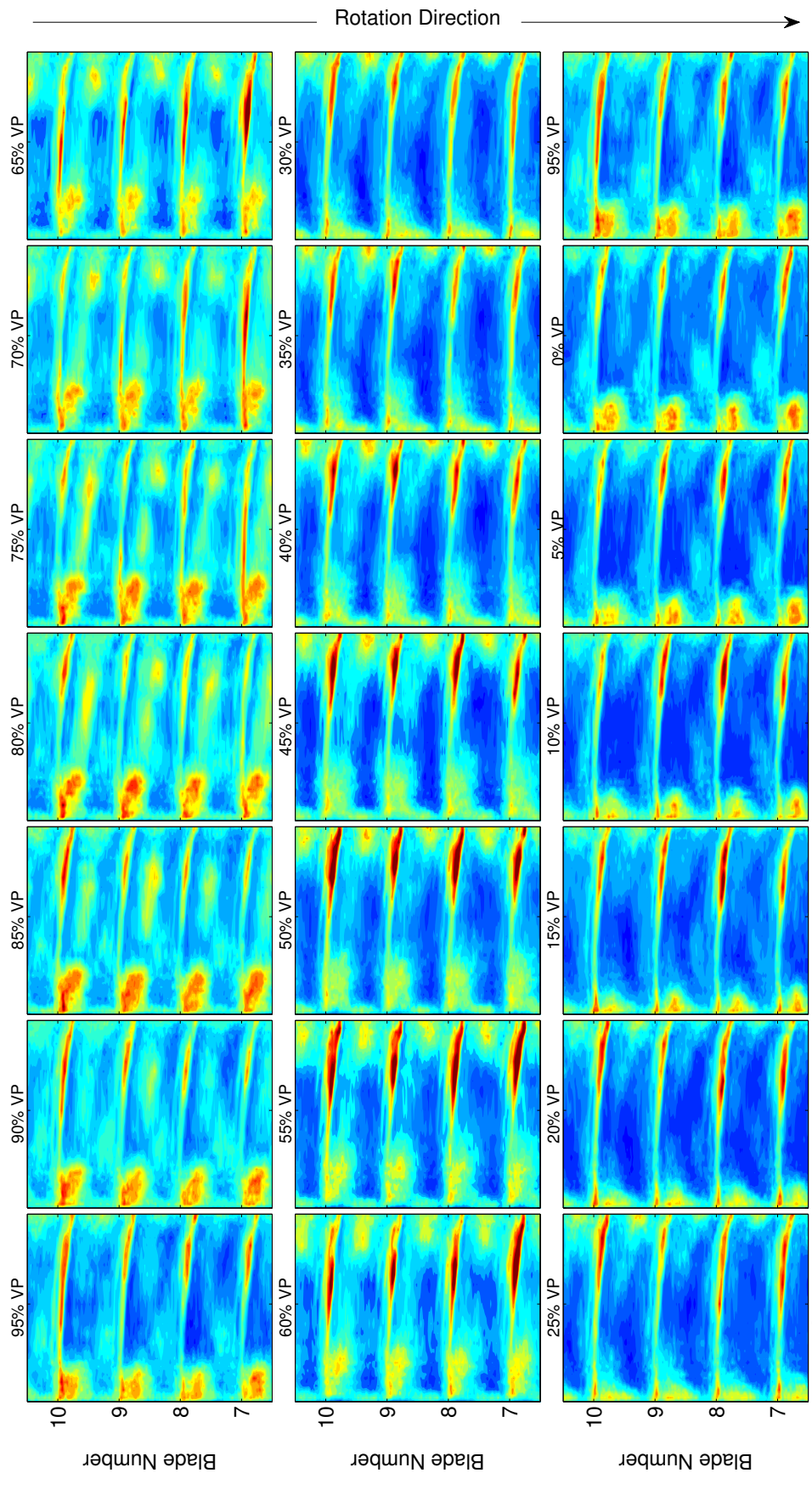


Figure B.5: Full vane passage of exit plane total pressure measurements of 38EO-1T HL flow condition.

# APPENDIX C. SURFACE PRESSURE COEFFICIENTS OF REDUCED S1 VANE-COUNT CONFIGURATION

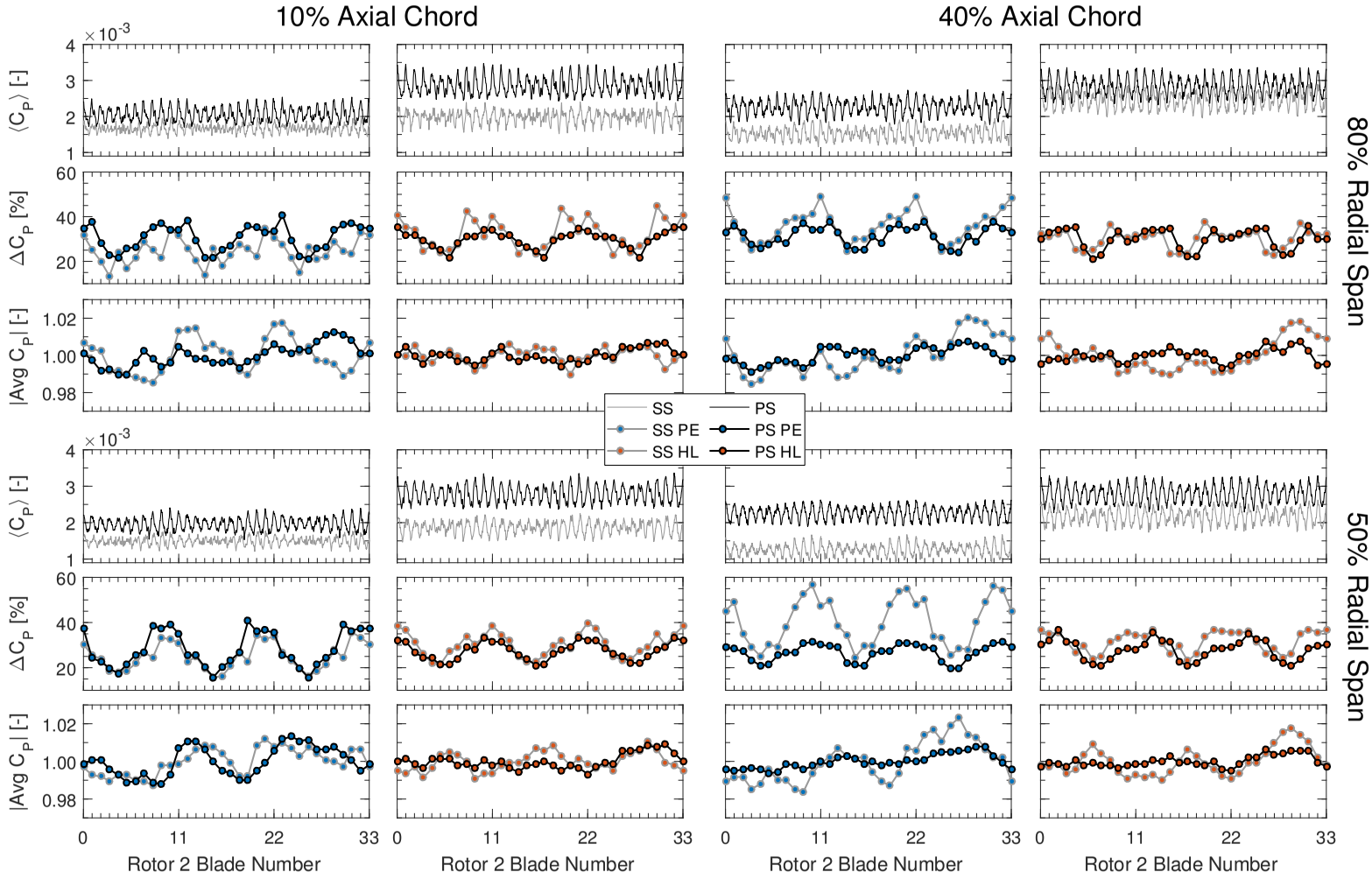


Figure C.1: Surface pressures of the 88EO-1CWB crossing flow condition.

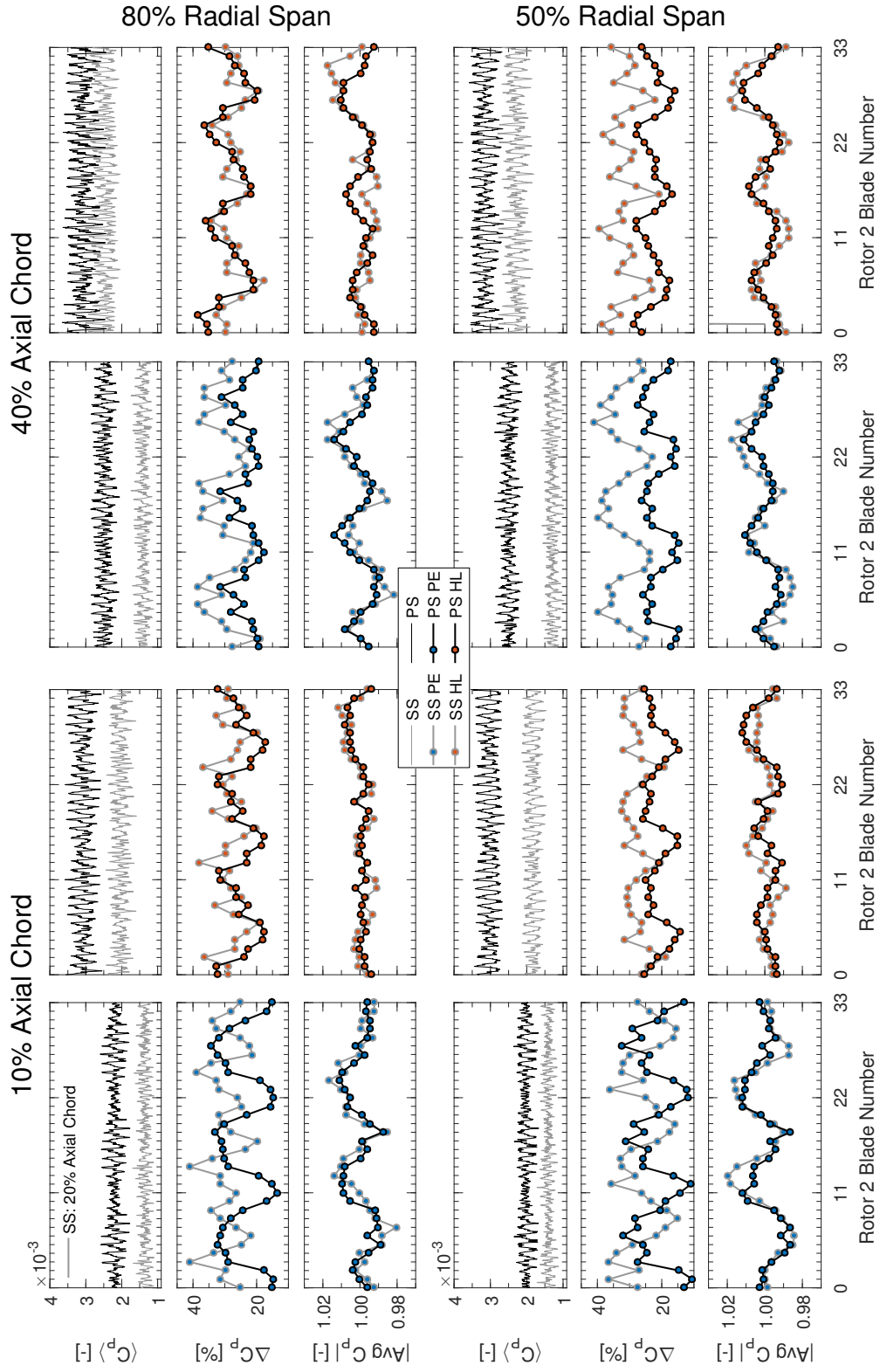


Figure C.2: Surface pressures of the 76EO-1CWB crossing flow condition.

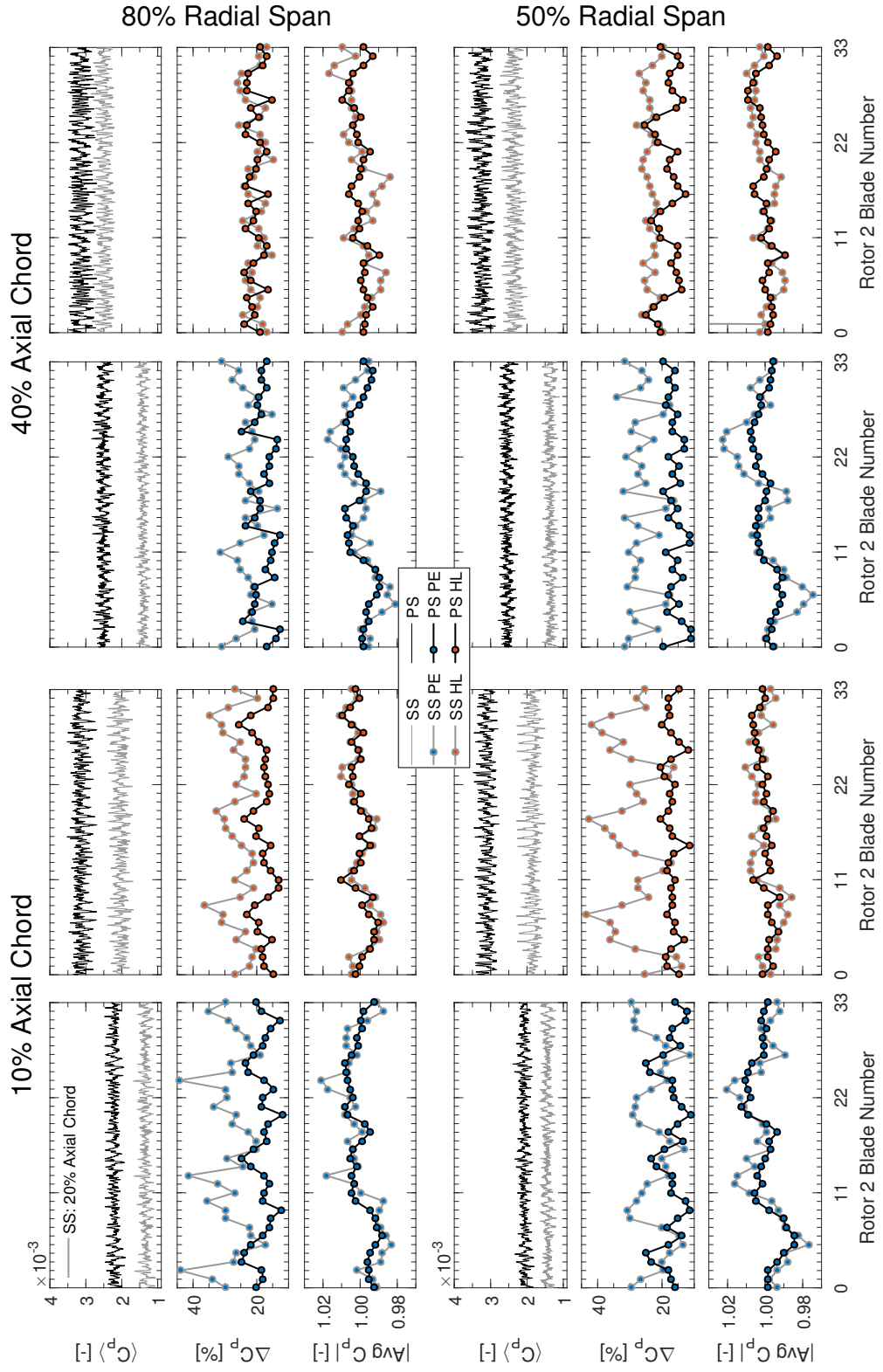


Figure C.3: Surface pressures of the 38EO-1T crossing flow condition.